PERMANENT MAGNET HYSTERESIS SYNCHRONOUS MOTOR ANALYSIS AND DSP BASED VECTOR CONTROL

CENTRE FOR NEWFOUNDLAND STUDIES

TOTAL OF 10 PAGES ONLY
MAY BE XEROXED

(Without Author's Permission)

RUIFENG QIN

PERMANENT MAGNET HYSTERESIS SYNCHRONOUS MOTOR ANALYSIS AND DSP BASED VECTOR CONTROL

by

©RUIFENG QIN, B.Eng., M.Eng.

A thesis submitted in partial fulfilment
of the requirements for the degree of
Doctor of Philosophy

Faculty of Engineering and Applied Science
Memorial University of Newfoundland

October 1996

St. John's, Newfoundland, Canada

Abstract

The hybrid permanent magnet hysteresis synchronous (PMHS) motor has many distinct advantages over conventional permanent magnet or hysteresis motors. Based on the features of PMHS motor structure and the models of permanent magnet and hysteresis, the magnetic equivalent circuit and electrical equivalent circuit of the PMHS motor are developed. An analytical model including the derivation of state variable equations in the time domain is also developed. The transient current, torque and speed during the starting and synchronizing process have been calculated by solving the state variable equations numerically. Reasonably good agreements between the computed and experimental results of a 5 hp PMHS laboratory motor confirm the validity of the proposed analysis.

Programmed sinusoidal pulse width modulation, which is based on the digital signal processing (DSP), is used for the PMHS motor vector control. Using the frequency domain approach, the direct and quadrature axis current controllers are developed. The control algorithms are then put into a form that could be implemented directly on the real-time digital system. Finally, an experimental verification of the algorithm is carried out by measuring the stator line current at different frequencies.

For the speed controller design, first, the general expression of the developed torque of the PMHS motor is derived. Upon controlling the stator current i_{ds} to be zero,

i_{qs} becomes the only controllable variable. The speed controller design is based on the symmetry optimization. The performance of the speed controller is then demonstrated with several real-time experiments, and it is shown to possess the desired characteristics in terms of rise time and overshoot. The rotor position and speed responses are quite smooth in a wide speed range and without any oscillation.

The complete experimental DS1102 DSP based drive system has been built. A detailed description of the system general hardware and software is discussed. Finally, the experimental results of a DSP based PMHS motor vector control system are given. The motor is controlled successfully at inverter frequencies 1 Hz to 60 Hz .

The transient and steady state performances of current and speed show that the vector control of the PMHS motor has important features for smooth and quiet operation over a wide range of speed. The experimental results verify the effectiveness of the motor models for high performance PMHS motor drive.

Acknowledgements

I would like to express my most sincere gratitude and appreciation to my supervisor Dr. M.A.Rahman, for his guidance, encouragement and active support throughout the course of this study. I am very grateful for his training which will be a valuable resource in my professional career.

My special thanks to Dr. B. Jeyasurya and Dr. G. George, members of the supervisory committee, for their constructive criticisms and valuable suggestions in preparing this thesis.

Help from the technical staff, Mr. R. Newman, Mr. D. Guy and Mr. D. Johnson, at the Faculty of Engineering and Applied Science is gratefully acknowledged. Also, special thanks for my colleagues in the Power and Control System Lab, Mr. A. Hoque, Ms. M. Zaman and Mr. T. Radwin, for their cooperation and discussion.

I would also like to take this opportunity to acknowledge the financial support through Memorial University of Newfoundland and Dr. M. A. Rahman's grant which made this work possible.

Finally, I would like to thank my wife, Zhongyun Ma, my parents and my son Ling Qin, for their encouragement, understanding, patience and support.

Contents

Abstract ii

Acknowledgements iv

List of Figures ix

1 Introduction 1

1.1 The Present Status of the Hysteresis Motor in High Performance Drives 1

1.2 The Starting Problem of Permanent Magnet Motors 3

1.3 New Hybrid Motor -- Permanent Magnet Hysteresis Motor 7

1.4 Motor Drives 8

1.5 Objectives of the Thesis 12

1.6 The Organization of the Thesis 13

2 Modelling of PMHS Motor 16

2.1 Introduction 16

2.2 PMHS Motor Structure 16

2.3 Magnetic Equivalent Circuit of A PMHS Motor 19

2.3.1 Model of Permanent Magnet 19

2.3.2 Model of Hysteresis 21

2.3.3 Magnetic Equivalent Circuit 24

2.4 Electrical Equivalent Circuit of a PMHS Motor 28

2.5 State Variable Equation 33

2.6 Summary 41

3 Programmed Pulse Width Modulation in the PMHS Motor Drive 42

3.1 Introduction 42

3.2 Sinusoidal Pulse Width Modulation 43

3.3 Voltage Space Vector 47

3.4 The Generation of Digital PWM Signals 54

3.5 The Operation of the Voltage Source Inverter 61

3.6 Summary 69

4 Direct and Quadrature Axes Current Controls in the PMHS Motor Drive 71

4.1 Introduction 71

4.2 Current and voltage Transformation 72

4.3 The Analysis of Stator Frame Current Controller 74

4.4 Quadrature Axis Current Control 80

4.5 Direct Axis Current Control 97

4.6 Digital Filter Design and Application 99

4.7 Current Control Implementation and Experimental Results 104

4.8 Summary 107

5 Torque and Speed Controls of the PMHS Motor 110

5.1 Introduction 110

5.2 PMHS Motor Torque Equation 111

5.3 Speed Control Loop Transfer Function 118

5.4 Speed Controller Structure and Design 124

5.5 Speed Control Implementation and Experimental Results 133

5.6 Summary 136

6 System Implementation and Experimental Results **138**

6.1 Introduction 138

6.2 General Description of the PMHS Vector Control System 139

6.2.1 System General hardware Description 139

6.2.2 System General Software Description 143

6.3 DS1102 DSP Control Board 146

6.4 Experimental PMHS Motor and Inverter 153

6.5 Rotor Position and Stator Current Measurements 155

6.5.1 Optical Incremental Encoder 155

6.5.2 Speed Calculation software 158

6.5.3 Stator Current Measurement 159

6.6 Experimental Results of Steady State and Starting Performances 160

6.7 Summary 170

7 Summary, Conclusion and Suggestions for Future Research **171**

7.1 Thesis Summary and Conclusion 171

7.2 Contributions 175

7.3 Suggestions for Future Research 176

References **178**

Appendices **184**

A Design Data of the PMHS Motor 184

B The Flow Chart of the State Variable Equation 186

C The Derivation of the Unit Matrix 187

D DS1102 Data Sheet 189

E Experimental Results of Back emf of the PMHS Motor 193

List of Figures

1.1 Typical hysteresis motor torque vs speed 6

1.2 Typical PM motor torque vs speed 6

2.1 Rotor configuration of the PMHS motor 17

2.2 Demagnetization characteristic of NdFeB magnet 20

2.3 Steps in producing a simplified hysteresis loop model 22

2.4 Magnetic equivalent circuit of the PMHS motor 25

2.5 Simplified magnetic equivalent circuit 26

2.6 d-q axis model of the PMHS motor 28

2.7 Electrical equivalent circuit of the PMHS motor 30

2.8 PMHS motor state variable model 34

2.9 Open loop starting process of the PMHS motor 39

3.1 Sinusoidal pulse-width modulation for three-phase inverter 45

3.2 Three-phase inverter 49

3.3 Three-phase voltage source inverter 50

3.4 Voltage space phasors 50

3.5 Voltage space vector 52

3.6 PWM inverter duty cycle arrangement 56

3.7 TMS320P14 PWM channel behaviour 56

3.8 PWM duty cycle generation 58
3.9 The variation of PWM duty cycle 59
3.10 Experimental PWM duty cycle 60
3.11 DSP and inverter interface circuit 63
3.12 PWM logic relations of a switching sequence 64
3.13 Experimental gate signal and shoot through delay 66
3.14 Experimental three-phase SPWM waveform 67
3.15 Experimental results of the modulation variation 68
4.1 Stator frame current controller 75
4.2 Multi-loop control structure 82
4.3 Block diagram of current control 82
4.4 Digital PI controller 84
4.5 Current sensing system 88
4.6 Current open loop bode plot 95
4.7 Current closed loop bode plot 96
4.8 Block diagram of first order IIR filter 102
4.9 Experimental currents before and after being filtered 103
4.10 Current control function overview 105
4.11 Experimental line and rotor frame currents 108
5.1 Control structure with series connection 119
5.2 Block diagram of speed control system 119
5.3 Speed open loop bode plot 129

5.4 Unit-step response of speed control system 130

5.5 Speed closed loop bode plot with zero 131

5.6 Speed closed loop bode plot without zero 132

5.7 Steady state performances of the rotor position and speed 134

5.8 Transient performance of the rotor position and speed 135

6.1 Experimental setup of DSP based vector control of PMHS motor 141

6.2 Experimental setup block diagram 142

6.3 The block diagram of the vector control scheme for the PMHS motor 144

6.4 The main program flow chart of the PMHS motor vector control 145

6.5 Block diagram of the DS1102 DSP board 147

6.6 Block diagram of an incremental encoder interface 153

6 7 Experimental PMHS motor 154

6.8 Structure of incremental encoder 157

6.9 Incremental encoder output waveforms 157

6.10 Speed measurement flow chart 159

6.11 36 Hz steady state performance of the PMHS motor 163

6.12 36 Hz starting performance of the PMHS motor 164

6.13 1 Hz steady state performance of the PMHS motor 165

6.14 12 Hz steady state performance of the PMHS motor 166

6.15 12 Hz starting performance of the PMHS motor 167

6.16 60 Hz steady state performance of the PMHS motor 168

6.17 60 Hz starting performance of the PMHS motor 169

B.1 The flow chart of the state variable equation 186

E.1 emf of the PMHS motor vs speed 195

E.2 emf of the PMHS motor when it is blocked 196

E.3 emf of the PMHS motor when it runs at 0.9 p.u. speed 197

Chapter 1

Introduction

This thesis is concerned with the analysis, vector control system design and implementation of a permanent magnet hysteresis synchronous (PMHS) motor.

1.1 The Present Status of the Hysteresis Motor in High Performance Drives

Since the presentation of the theory of hysteresis torque by Steinmetz [1] in 1908, much work has been done on the theory and practice for hysteresis motors. In the 1920's, hysteresis motors were used on electric clocks, control mechanisms and relays. In 1940, Teare [2] published a method of calculating the motor torque from known field configurations of magnetic flux and magnetomotive force in the hysteresis material.

The development of new magnetic materials having more hysteresis energy per unit volume of the material, like aluminum nickel and cobalt based alloys, has led to the production of hysteresis motors from fractional horse power to several kilowatts rating [3]. Hysteresis motors have emerged from the state of an engineering curiosity to quite

widely used small motors. The research efforts of the past decades bear testimony to the rapidly growing importance in the development of different types of small and integral horse power hysteresis motors. According to my search, 225 representative papers about hysteresis motors have been published from 1908 to 1996. All of the research works on hysteresis motors may be classified as follows:

(1) Basic theory about hysteresis torque and analysis of hysteresis motors based on the approximation of representing the hysteresis loop by either elliptical or parallelogram models;

(2) General equivalent circuits in which harmonics, end winding and slotting effects are ignored;

(3) Field analysis using Maxwell's equations and numerical methods;

(4) The analysis of the effects of high harmonics and stator slotting;

(5) Over excitation and solid-state control;

(6) The study of the hysteresis reluctance motor and the permanent magnet hysteresis motor.

The hysteresis motor is widely used in small motor applications. It has not only simple constructional features with conventional stator windings and a solid rotor hysteresis ring, but also high built-in self-starting torque during the run up and synchronization period. It has no rotor slots and thus it has low noise during operation. These advantages make the hysteresis motor specially suitable for applications, such as in gyros, pumps, timing and recording equipment in which constant torque, synchronous speed and quiet operations are required. In spite of these advantages, the commercial

hysteresis motor still suffers from many limitations, e.g., high magnetizing current, low power factor, and low efficiency associated with high parasitic losses [4]. It also has two additional subtle disadvantages for high accuracy drives such as in gyroscopes. One is the flutter associated with synchronous speed [5]. When the rotor reaches synchronous speed, the rotor flux ceases to sweep around it, and residual flux density B_r of the hysteresis material on the rotor is relatively fixed. As the eddy current torque disappears at synchronous speed, the motor behaves as a temporary permanent magnet motor [6]. However, when random disturbances happen, the resultant poles will move along the rotor surface, thus the rotor will oscillate around the synchronous speed at a low frequency of 3-5 Hz. The other disadvantage is that the hysteresis motor has no preferred synchronizing point, and the rotor position compared with the rotating magnetic field is random. This gives rise to the gyro drifting errors. Figure 1.1 illustrates the starting torque characteristics of a hysteresis motor [7]. The hysteresis and eddy current torques are denoted by the dashed lines. It is to be noted that the resultant torque has high built-in starting and synchronizing capabilities.

1.2 The Starting Problem of Permanent Magnet Motors

The history of the permanent magnet (PM) motor is closely related to the development of PM materials. Permanent magnet materials have been developed in several distinct stages:

(1) Natural PM materials which were discovered in the primitive period;

(2) Commercial PM materials were manufactured in 1930's under the name of Alnico family series;

(3) The barium ferrite PM materials were developed in late 1950's;

(4) The rare earth permanent magnets(REPM) such as samarium cobalt, etc. were developed in late 1960's and early 1970's;

(5) The Neodymium-Iron-Boron (NdFeB) magnets were made available in the 1980's.

The magnetic parameters which are important in developing PM motors are:

(1) Residual flux density B_r;

(2) Coercive force H_c;

(3) Maximum energy products (BH_{max}).

The PM motors have been developed over a long period of time. It was reported that the first PM motor was built in 1900's. Yet the first motor with commercial value was only built in 1947, when the General Electric (GE) Company built the first commercial motor using Alnico material. During the period of 1900-1970, there existed two major problems in the design of PM motors. First, due to the low energy products of the PM materials, the air gap flux was lower than that of a d.c. motor. Secondly, the B-H curve in its second quadrant is easily subjected to demagnetization for its low coercive force. For a PM generator, the rotor flux may be reduced to zero if a short circuit occurs, while for the PM motor however, it is subjected to a reversal of flux each time it starts up. Thus the permanent magnet motor presents a more severe problem

of demagnetization than a permanent magnet generator. These short-comings have been overcome since the advent of rare earth permanent magnets in the 1970's. For example, the maximum energy products of permanent magnets increased from 3.8 MGOe. in barium ferrite to 51 MGOe. in NdFeB magnets. The technical merits of the PM motor have received wide attention. Some of the notable works have been reported by Rahman [8] and Richter [9]. The technical report by Richter of the GE company provides detailed feasibility studies of energy conservation and economic benefit of using PM motors instead of induction motors. The advantages of using a PM motor are apparent. The efficiency of the PM motor has proved to be higher than that of the induction motor, as the winding losses (I^2R) of the rotor due to slip are eliminated.

Permanent magnet synchronous motors have several distinct advantages namely, high efficiency, high power factor, and higher stability. Smooth brushless operation and simple rotor construction of permanent magnet synchronous motors offer additional advantages particularly for high speed applications. However, the permanent magnet synchronous motor, when operated at line frequency, has a major drawback during the starting period as the magnets generate a brake torque which decreases the starting torque and reduces the ability of the rotor to synchronize a load. With the help of cage winding, sufficient accelerating torque is provided. When the motor reaches synchronous speed, the cage torque is reduced to zero, whereas the magnet torque becomes the sole source of motor torque [10]. Figure 1.2 shows the typical magnet brake torque, cage torque and resultant torque of the PM motors during the starting process.

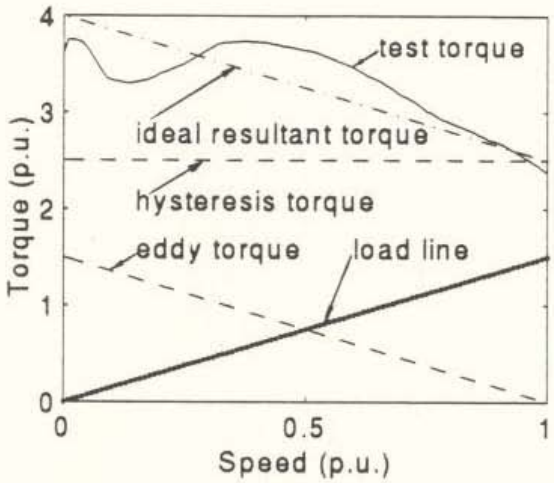

Fig. 1.1 Typical hysteresis motor torque vs speed

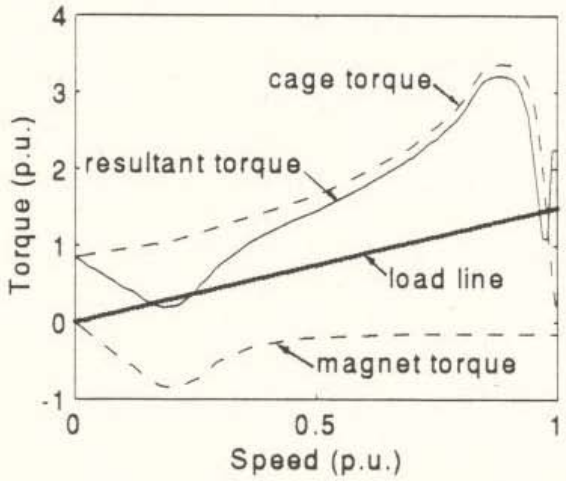

Fig. 1.2 Typical PM motor torque vs speed

1.3 New Hybrid Motor - Permanent Magnet Hysteresis Motor

The permanent magnet hysteresis synchronous (PMHS) motor is a new kind of motor which has received considerable attention in recent years [11]-[15]. The combination of PM and hysteresis materials in the rotor of the hybrid motor has many distinct advantages over the conventional PM or hysteresis motors [10-17]. The hybrid motor in which the permanent magnets are inserted into the slots at the inner surface of the hysteresis ring is called the permanent magnet hysteresis synchronous (PMHS) motor. The rotor structure of the PMHS motor is simple and the squirrel cage winding is eliminated because it has the built-in starting torque. It has high pull-in and pull-out torques and high efficiency [15].

During asynchronous speed, the motor torque consists of the hysteresis torque, eddy current torque and permanent magnet brake torque. At synchronous speed the motor torque consists of the hysteresis and permanent magnet torques. It combines the advantageous features of both the hysteresis and permanent magnet motors. The negative effect of the magnet brake torque is ideally compensated by the high eddy current torque, particularly at the starting and run-up period. This hybrid PMHS motor has great potential for applications in gyros, electric vehicles, air conditioning, compressor pumps, robotics and high performance industrial drives requiring constant torque, a wide range of speed and quiet operation.

1.4 Motor Drives

Electric motors have been the workhorses of industry for many years. The three basic types of electric motors, namely the dc, induction and synchronous motors, have served industrial needs for nearly a century [18]. In recent years, intense research effort has created other variations of motors, such as brushless dc motors, permanent magnet motors, and switched reluctance motors in many applications.

DC motors have traditionally dominated the domain of drive systems. Although the dc motor is more expensive, the control principles and converter equipment required are somewhat simpler in dc drives [19]. The field magnetomotive force (mmf) and the armature mmf of a dc motor are decoupled. The torque of a dc motor depends on armature current and field flux ($T \propto I_a\Psi_f$), and the field flux depends on field current ($\Psi_f \propto I_f$). This decoupled feature provides enhanced speed response for the torque characteristics. The control of torque is normally achieved by controlling the armature current with constant field current. Field weakening is employed to increase the speed beyond a base speed. The simplicity and flexibility of control of the dc motors have made them suitable for variable speed applications. However, the main disadvantages of the dc motor are its commutators and brushes, and the frequent maintenance required for its operation. It is also restricted by the sparks which come from the mechanical commutator system. These major problems of dc motors make them unsuitable for hazardous and maintenance free operation.

The induction motor is a rugged, reliable, and less expensive ac machine. It has been the economical workhorse for use in ac drive applications during the past decades [20]. Variable frequency drives originally used open loop and volt/hertz control to regulate motor flux. These motors are found to be satisfactory for low-performance, cost-effective industrial drives. Closed-loop control with slip regulation is introduced later for improved drive performance. Another control method that is often used for flux regulation is based on the co-ordination of stator current and slip frequency. A current source inverter is suitable for this drive. Unlike the volt/hertz control, the current-slip frequency control technique is somewhat independent of stator parameters. Hence, flux regulation can be achieved even at low speeds [21-22].

Both the volt/hertz and current-slip frequency control provide satisfactory steady-state performance. The volt/hertz control scheme requires closed-loop current regulation as well as accurate speed measurement. Therefore, both these methods are somewhat complicated to implement and fail to provide satisfactory transient performance. Field orientation is a vector control technique that provides a method of decoupling the two components of stator current: one producing the airgap flux and the other producing the torque [23]. Therefore, it provides independent control of torque and flux, which is similar to a separately excited dc motor. The magnitude and phase of the currents are controlled in such a way that flux and torque components of the current remain decoupled during dynamic and static conditions. Several methods have been proposed to implement field oriented control. Basically, the schemes can be classified into two groups: the direct method of field orientation, and the indirect method of field

orientation. The direct method of field-oriented control was originally proposed by Blaschke [23]. The method requires flux acquisition, which is determined by computation techniques using machine terminal quantities. The indirect method of field-oriented control was originally proposed by Hasse [24], and it avoids the requirement of flux acquisition by using known motor parameters to compute the appropriate motor slip to obtain the desired flux position. The scheme of indirect control method is simpler to implement than the direct method. Hence the indirect method of induction motor control is becoming more popular. However, the induction motors have inherent disadvantage of slip dependent rotor copper loss, and there is the problem of heat extraction from the motor core. The motors are either two or four pole types, thus the motors need large end windings and considerable back iron yoke. This partly causes its weight to increase.

The synchronous motor is becoming a strong competitor with the induction motor in the variable-speed drive domain. The main advantages, as compared to the induction motors, are the elimination of rotor copper loss and the natural ability to supply reactive current. In a synchronous motor, the magnetization is provided through the rotor circuit instead of the stator. Hence, the motor can be built with a larger airgap without degraded performance.

In recent years, there has been an emerging growth of permanent magnet (PM) synchronous motors [25-33]. In a PM motor, the rotor field is supplied by permanent magnets. The main advantage compared to the conventional synchronous motor is the elimination of the field coil, dc supply, brush gear and slip rings. Hence, lower loss and a less complex motor can be obtained. In a PM motor there is no provision for rotor side

excitation control. The control of the PM motor is done entirely through the stator excitation control. Field weakening is possible by varying the direct axis current to oppose the rotor magnet flux.

Applications of these permanently excited synchronous motors are found in various industrial drive systems, such as aerospace, machine tools, robotics, precision textiles, etc. The brushless permanent magnet synchronous motors are simply known as permanent magnet ac motors. These motors are either line start or inverter fed types whose polyphase stator windings are simultaneously switched on via balanced polyphase supply voltages.

There is another type of modern small brushless permanent magnet dc motor, commonly called brushless dc motor. Incidentally, these brushless dc motors are polyphase permanent magnet synchronous motors which are electronically commutated and sequentially switched on. They are mostly used for control purposes such as computer disk drives, robotics, automation, high quality turntables and tape capstans, etc. [34].

High performance in the ac motor drive is achieved through the vector control scheme, in which the motor's nonlinear properties and multivariable parameters are linearized and decoupled. The performance of the controlled ac motor, in a wide range of load and speed, is much like a separately excited dc motor. Vector control may be performed in various configurations and has become a rather mature technology.

A microprocessor based control of the hybrid permanent magnet hysteresis synchronous motor was first reported by Rahman and Qian in 1993 [17]. However, there

remain many problems yet to be solved. Some of the topics are listed below.

(1). It is necessary to establish an accurate analytical model of the PMHS motor, such as state variable equations, detailed equivalent circuit and torque equation, which are needed for theoretical analysis, simulation and real time implementation of the vector control.

(2). In the control system of the reference [17], the search coils present several disadvantages such as reliability and noise immunity. For these reasons, to eliminate search coils from the motor stator is a matter of concern. The rotor flux will be estimated from on-line current, rotor position and speed.

(3). The stability of the motor at low speed range, frequency less than 10 Hz, needs to be improved. Thereby the drive motor will operate in all speed ranges.

(4). Because of the speed limitation of analog to digital (A/D) and digital to analog (D/A) circuits in the Labmaster board which was used in reference [17], a high speed digital signal processor (DSP) is needed for more complex vector control of the PMHS motor.

1.5 Objectives of the Thesis

This thesis has two major objectives. The first is to establish an accurate analytical and control model of the permanent magnet hysteresis synchronous motor. This will include the models of permanent magnet and hysteresis, the magnetic equivalent circuit and electrical equivalent circuit, the state variable analysis model of the PMHS motor.

The second objective is to develop and successfully implement a digital signal processor based vector control system for the permanent magnet hysteresis synchronous motor in a wide speed range. This will include the design and implementaion of programmed sinusoidal pulse width modulation, digital current and speed controllers, digital filters and a complete experimental DS1102 DSP based vector control PMHS motor system.

1.6 The Organization of the Thesis

This thesis is organized as follows. A mathematical model for the PMHS motor is developed in Chapter 2. The derivation of both the magnetic equivalent circuit and electrical equivalent circuit is presented. The PMHS motor model for both transient and steady state operations is also presented. Using state variable equations, starting and synchronizing performances are predicted by solving the state variable equations numerically. The experimental results are also provided together with the comparison of the simulation results during starting and synchronization.

Chapter 3 describes the operation of the inverter used to drive the PMHS motor. First, the ideal operation of the inverter is reviewed from the point of view of a modulation system. The voltage space vector is then used to derive the expressions of the inverter operation. Next, the generation of the sinusoidal pulse width modulation (PWM) by the digital signal processor is discussed. The detailed analysis of the logic relations of a switching sequence is presented. Finally, the programmed three-phase sinusoidal pulse width modulation voltage is generated through the DS1102 DSP board. The

necessary interface circuit between the DSP board and the inverter is developed. And a shoot through time delay circuit has been built to prevent the upper and lower transistors of each leg of the PWM inverter from conducting simultaneously and shorting the power supply terminals together.

Chapter 4 focuses on the analysis and control of the current loop, and develops a fully digital current controller for the PMHS motor vector control. The derivation of the rotor frame model for the PMHS motor is briefly reviewed along with the necessary conversion transformations between the motor terminal voltages and currents and the corresponding direct and quadrature axis quantities used in the model. Next, the regulation of d-q axis currents using the conventional stator frame line current controllers is shown to introduce nonlinear speed dependent coupling between the direct and quadrature axis currents. The quadrature and direct axis current controllers are then developed. The controller design is carried out in the frequency domain. Experimental results are also presented in Chapter 4.

Chapter 5 concentrates on the development of the digital speed controller. The PMHS motor torque is discussed in different control conditions. Next, the derivation of the speed control loop transfer function is presented in detail. The controller design is carried out by using the symmetry optimization technique. Finally, implementation details and experimental results are presented.

Chapter 6 completes the development of the vector control system for the PMHS motor by specifying the controller algorithm and by combining it with the results of the previous chapters. The hardware and software implementation of the DSP based PMHS

motor vector control system is presented. A general description of the system software and hardware requirements is provided. A detailed description of the requirements for implementing the system is presented. Finally, the performance of the PMHS motor vector control system is illustrated by several experiments. The experimental results demonstrate the effectiveness of the new approach for the high performance PMHS motor drive.

Chapter 7 provides the summary, conclusion, and suggestions for future work. The contributions of this thesis are highlighted.

Chapter 2

Modelling of PMHS Motor

2.1 Introduction

The objective of this chapter is to develop a mathematical model for the permanent magnet hysteresis motor suitable for the simulation and application of real-time digital control techniques. The model parameters are related to the motor structure and dimensions. Analytical expressions are developed wherever a closed form expression can be obtained.

The discussion will start with the introduction of the PMHS motor structure. The features of this structure and the assumptions involved in developing the equivalent magnetic circuits and electrical equivalent circuits are also presented in this section.

An analytical model including the derivation of state variable equations in the time domain is presented. The transient current, torque, speed, and flux linkages during the starting process have been calculated by solving the state variable equations numerically.

2.2 PMHS Motor Structure

Fig. 2.1 shows the 4-pole rotor assembly of the PMHS motor. The rotor consists

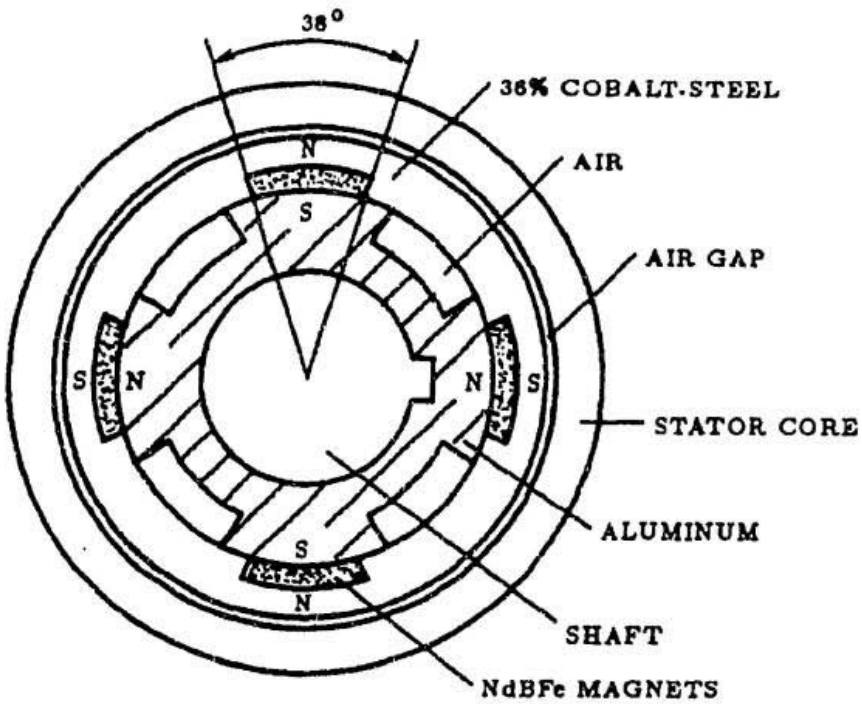

Fig. 2.1 Rotor configuration of the PMHS motor

of a hysteresis ring made of 36% of cobalt steel alloys. This hysteresis ring is supported by the aluminium sleeve and the sleeve is keyed to the motor shaft. Reluctance grooves for the permanent magnets are cut from the inside diameter of the hysteresis ring and the Neodymium Iron Boron (NdFeB) magnets are inserted in the slots. This interior type permanent magnet hysteresis rotor eliminates the airgap undulations due to the rotor slot openings. It thus minimises the flux parasitic losses [16]. The stator has standard three phase 4-pole windings like those in induction or synchronous motors. The magnetic properties of NdFeB permanent magnets and cobalt-steel hysteresis material are listed in Table 2.1.

Table 2.1 Properties of the hysteresis and PM materials

Type of Material	B_r	H_c	BH_{max}	μ_r
Units	(kG)	(kOe.)	(MGOe.)	
36% Cobalt steel hysteresis material	9.6	0.24	1.00	18.0
NdFeB permanent magnets	11.38	10.84	31.10	1.01

Where B_r is the residual flux density of the magnet, H_c is the coercive force of the magnet and μ_r is the relative permeability of magnet material which is determined from the motor's operating point of B-H curve.

2.3 Magnetic Equivalent Circuit of A PMHS Motor

2.3.1 Model of Permanent Magnet

One of the NdFeB magnets of the PMHS motor in Fig. 2.1 is shown in Fig. 2.2(a). The magnet has a radial length l_m and an angular width 2α. The demagnetization characteristic of a NdFeB magnet material is shown in Fig. 2.2(b) [35]. The characteristic is linear over the entire second quadrant and the linearity extends to the third quadrant. In normal use, the magnet operation is limited to the first and second quadrant only. Driving the magnet past the remanence into the first quadrant normally causes no harm, as this is in the direction of magnetization. At extremely high stator currents, the point of operation on the demagnetization characteristic can move to the third quadrant. If the operation in the third quadrant extends to the nonlinear part, some permanent demagnetization of the magnet occurs and the resulting recoil line is roughly parallel to the straight line shown in Fig. 2.2(b). Hence the peak reverse magnetic field that the magnet can be safely subjected to is H_p from Fig. 2.2(b), after which the demagnetization curve becomes nonlinear. When the magnet is subjected to this peak reverse magnetic field, the flux density in the magnet reverses and has a value B_p as shown in Fig. 2.2(b).

Due to the linearity of the characteristic over the operating range, the magnet can be modelled as a constant mmf source F_c in series with a constant reluctance $\Re_c$ where F_c and $\Re_c$ are given by

$$F_c = H_c l_m \qquad (2.1)$$

where l_m is the magnet thickness and

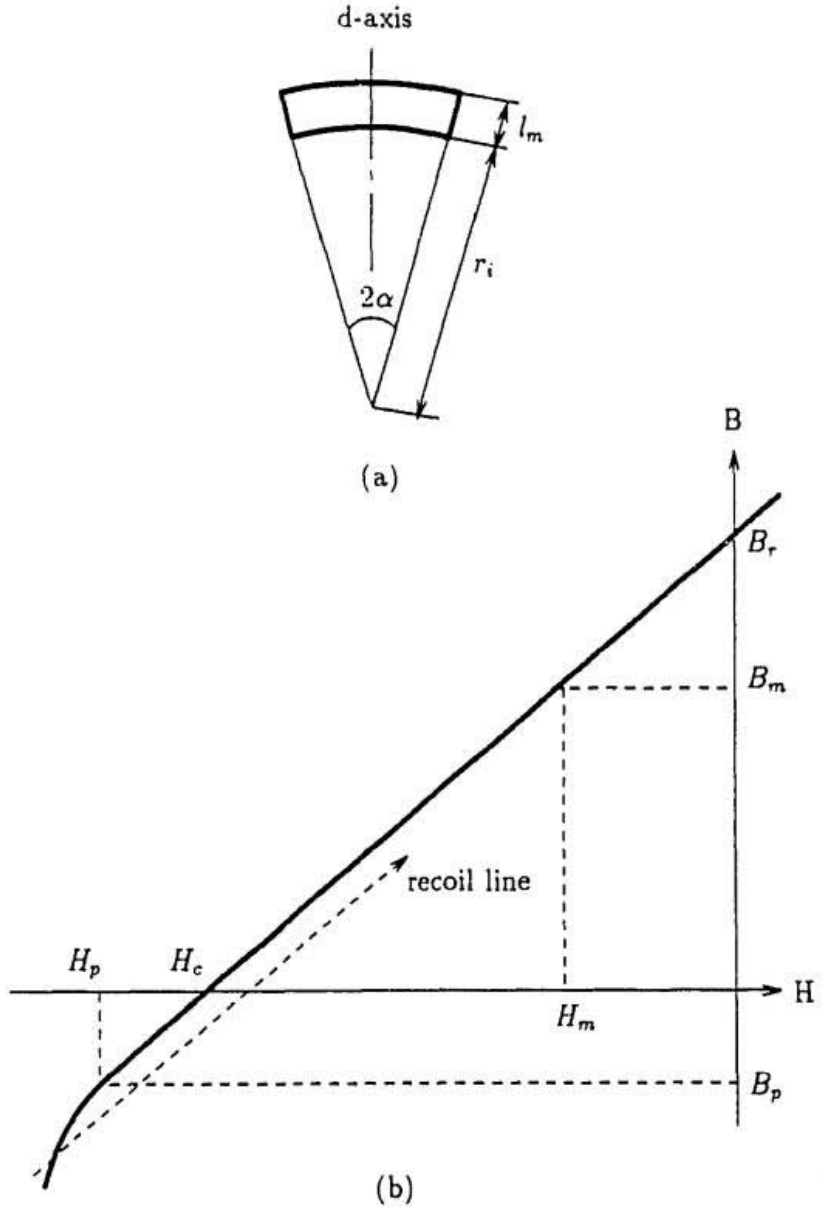

Fig. 2.2 Demagnetization characteristic of NdFeB magnet [35]

(a) NdFeB magnet in the PMHS rotor

(b) Demagnetization characteristic of NdFeB magnet

$$\Re_c = \frac{l_m}{\mu_0 \mu_r l_r d_r \alpha} \qquad (2.2)$$

where l_r is the rotor length and d_r is the mean diameter of rotor at the magnets.

2.3.2 Model of Hysteresis

The flux ϕ in the hysteresis material is related to its magnetomotive force F by the idealized B-H relationship and the hysteresis loop is represented by a parallelogram as shown in Fig. 2.3(a) and 2.3(b) [36]. In Fig 2.3(b), the slope of line bc is $1/\Re_{hH}$ and the slope of line ab is $1/\Re_s$, where $\Re_{hH}$ and $\Re_s$ are unsaturated and saturated reluctances, respectively. Fig. 2.3(a) may be used to determine the flux distribution for a given magnetic potential distribution. The analysis can, however, be simplified and generalized by producing a simplified model of the hysteresis characteristic.

From Fig 2.3(b) the equation of line bc is written as

$$\phi = \frac{1}{\Re_{hH}} (F - F_0) \qquad (2.3)$$

$$F = \Re_{hH} \phi + F_0 \qquad (2.4)$$

So the line bc can be represented as the superposition of line $F = \Re_{hH}\phi$ with the slope of $1/\Re_{hH}$ and the vertical line $F = F_0$. The equation of line dc is written as

$$\phi = \frac{1}{\Re_s} F + \phi_0 \qquad (2.5)$$

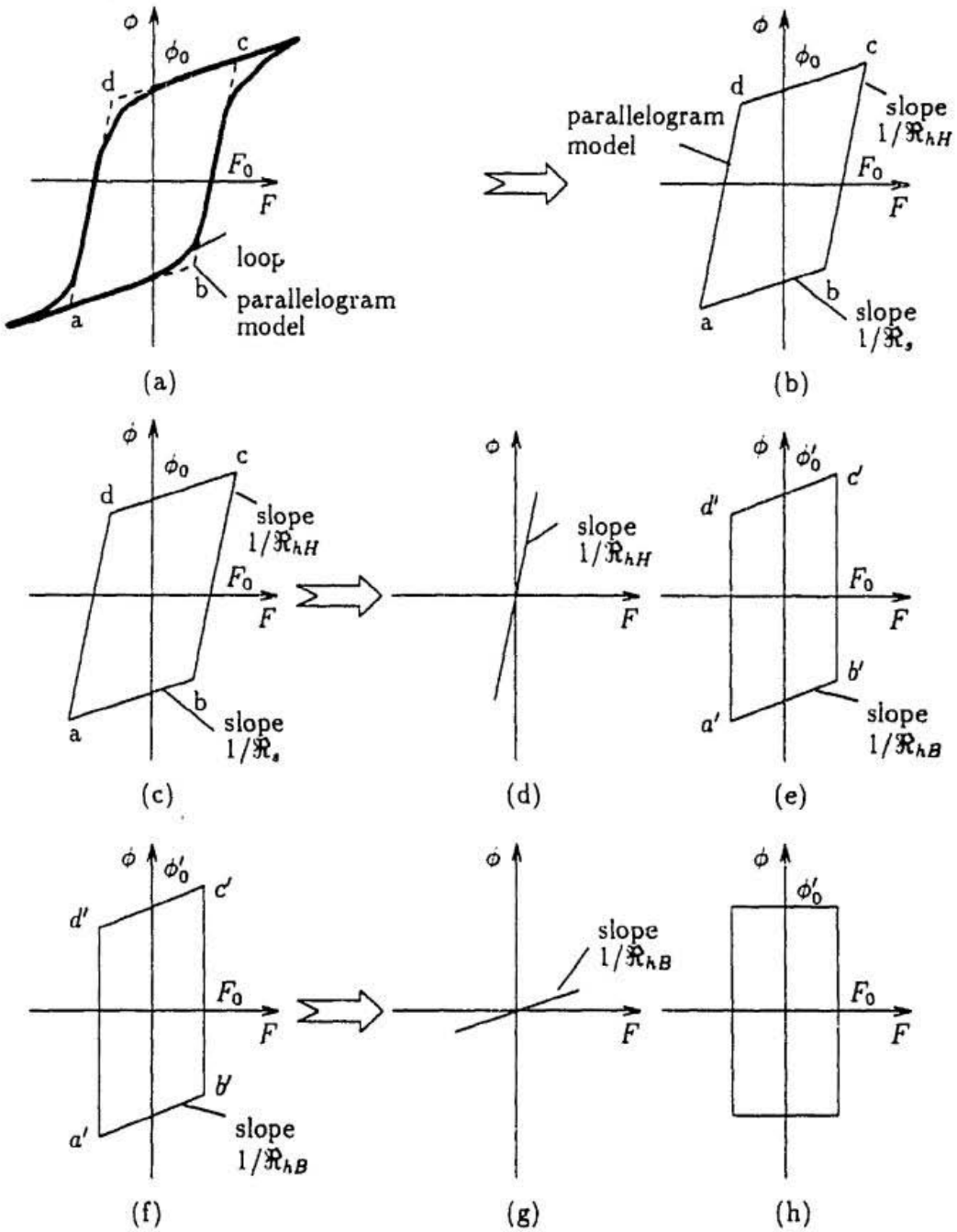

Fig. 2.3 Steps in producing a simplified hysteresis loop model

$$F=\Re_s(\phi-\phi_0) \tag{2.6}$$

Let $\Re_{hB} = \Re_s - \Re_{hH}$, then equation (2.6) will be

$$\begin{aligned} F &= (\Re_{hB}+\Re_{hH})(\phi-\phi_0) \\ &= \Re_{hB}[\phi-(\Re_{hB}+\Re_{hH})\phi_0/\Re_{hB}]+\Re_{hH}\phi \\ &= \Re_{hB}(\phi-\phi_0')+\Re_{hH}\phi \end{aligned} \tag{2.7}$$

where $\phi_0' = (\Re_{hB} + \Re_{hH})\phi_0/\Re_{hB}$. So the line dc is represented as the superposition of line $F=\Re_{hH}\phi$ with the slope of $1/\Re_{hH}$ and the line $F=\Re_{hB}(\phi-\phi_0')$ with the slope of $1/\Re_{hB}$. Thus the first process of simplifying the parallelogram model is shown in Fig. 2.3(c), (d) and (e). The Fig. 2.3(c) is represented as the superposition of Figs. 2.3(d) and (e).

In Fig. 2.3(e) the equation of line d'c' is

$$\phi=\frac{1}{\Re_{hB}}F+\phi_0' \tag{2.8}$$

Thus Fig. 2.3(e) or Fig. 2.3(f) can be further simplified as the superposition of a line with the slope of $1/\Re_{hB}$ and a rectangular loop as shown in Figs. 2.3(g) and (h), respectively.

As shown above, the parallelogram model is represented as a linear reluctance $\Re_{hH}$ in series with a vertically sided ϕ/F characteristic as shown in Figs. 2.3(d) and (e). The linear reluctance $\Re_{hH}$ has an effect which is equivalent to an extension of the air gap. The nonlinear characteristic of Fig. 2.3(f) can be further simplified by representing it as a linear reluctance $\Re_{hB}$ in parallel with a rectangular loop nonlinear element as shown in Figs. 2.3(g) and (h). So the parallelogram as shown in Fig. 2.3(b) is finally represented by Figs. 2.3(d), (g) and (h).

2.3.3 Magnetic Equivalent Circuit

The following assumptions are considered in the derivation of the PMHS motor model.

(1). The stator is assumed to have sinusoidally distributed windings.

(2). The magnetic flux is radial in the air gap and circumferential in the rotor hysteresis material.

(3). The eddy currents and hysteresis effects in the rotor hysteresis material are taken into account in the cases of both run-up and synchronizing operations.

(4). The B-H loop of the hysteresis material is modelled by a parallelogram [36].

The magnetic equivalent circuit of the PMHS motor is shown in Fig. 2.4, where

$F_{dl,ql}$: the primary magnet motive forces in the d-axis and q-axis

$\phi_{dh,qh}$: flux through idealized hysteresis element in d-axis and q-axis

ϕ_{pm} : flux through permanent magnet material

$\Re_{d\delta,q\delta}$: air-gap reluctance in d-axis and q-axis

$\Re_{hB}$: saturated incremental reluctance

$\Re_{hH}$: unsaturated incremental reluctance

$\Re_{pm}$: inner leakage reluctance of permanent magnet material

$\Re_{\sigma}$: leakage reluctance

For the convenience of analysis the simplified version of magnetic circuit is shown in Fig. 2.5, where

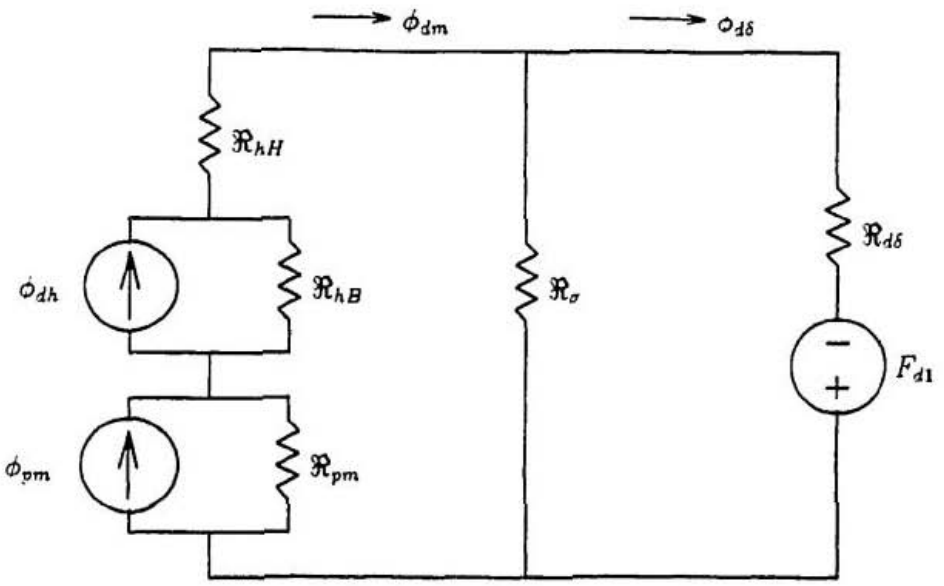

(a) d-axis magnetic equivalent circuit of PMHS motor

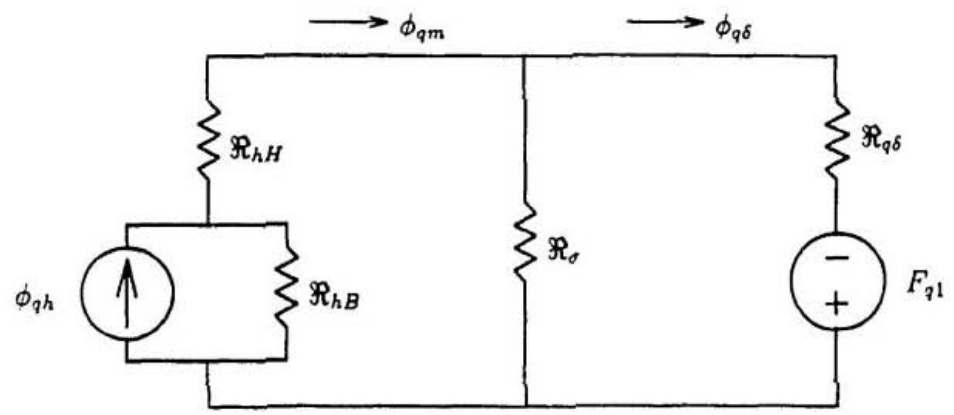

(b) q-axis magnetic equivalent circuit of PMHS motor

Fig. 2.4 Magnetic equivalent circuit of the PMHS motor

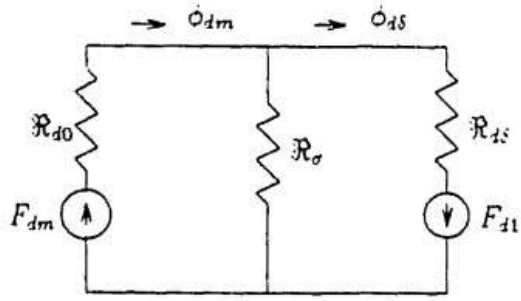

Fig. 2.5 Simplified magnetic equivalent circuit

$$\Re_{d0}=\Re_{hH}+\Re_{hB}+\Re_{pm} \tag{2.9}$$

$$F_{dm}=\Re_{hB}\phi_{dh}+\Re_{pm}\phi_{pm} \tag{2.10}$$

By mesh analysis one obtains

$$\phi_{dm}(\Re_{d0}+\Re_{\sigma})-\phi_{dl}\Re_{\sigma}=F_{dm} \tag{2.11}$$

$$\phi_{dm}(\Re_{dl}+\Re_{\sigma})-\phi_{dm}\Re_{\sigma}=F_{dl} \tag{2.12}$$

From equation (2.12), ϕ_{dm} is obtained as

$$\phi_{dm}=\frac{\phi_{dl}(\Re_{dl}+\Re_{\sigma})-F_{dl}}{\Re_{\sigma}} \tag{2.13}$$

substituting equation (2.13) into equation (2.11), one obtains

$$\frac{\phi_{d\delta}(\Re_{d\delta}+\Re_{\sigma})-F_{d1}}{\Re_{\sigma}}(\Re_{d0}+\Re_{\sigma})-\phi_{d\delta}\Re_{\sigma}=F_{dm} \tag{2.14}$$

$$\phi_{d\delta}[(\Re_{d\delta}+\Re_{\sigma})(\Re_{d0}+\Re_{\sigma})-\Re_{\sigma}^{2}]=F_{dm}\Re_{\sigma}+F_{d1}(\Re_{d0}+\Re_{\sigma}) \tag{2.15}$$

$$\phi_{d\delta}=\frac{F_{dm}\Re_{\sigma}+F_{d1}(\Re_{d0}+\Re_{\sigma})}{\Re_{d0}\Re_{d\delta}+\Re_{d0}\Re_{\sigma}+\Re_{d\delta}\Re_{\sigma}} \tag{2.16}$$

Finally, flux $\phi_{d\delta}$ is written as

$$\phi_{d\delta}=\Lambda_{dm}F_{dm}+\Lambda_{d}F_{d1} \tag{2.17}$$

where

$$\Lambda_{dm}=\frac{\Re_{\sigma}}{\Re_{d0}\Re_{d\delta}+\Re_{d0}\Re_{\sigma}+\Re_{d\delta}\Re_{\sigma}} \tag{2.18}$$

and

$$\Lambda_{d}=\frac{\Re_{d0}+\Re_{\sigma}}{\Re_{d0}\Re_{d\delta}+\Re_{d0}\Re_{\sigma}+\Re_{d\delta}\Re_{\sigma}} \tag{2.19}$$

If there is no permanent magnet material in the q-axis of the PMHS motor, then

$$\Re_{q0}=\Re_{hH}+\Re_{hB} \tag{2.20}$$

$$F_{qm}=\Re_{hB}\phi_{qh} \tag{2.21}$$

$$\phi_{q\delta}=\Lambda_{qm}F_{qm}+\Lambda_{q}F_{q1} \tag{2.22}$$

where

$$\Lambda_{qm} = \frac{\Re_a}{\Re_{q0}\Re_{qs} + \Re_{q0}\Re_a + \Re_{qs}\Re_a} \tag{2.23}$$

and

$$\Lambda_q = \frac{\Re_{q0} - \Re_a}{\Re_{q0}\Re_{qs} + \Re_{q0}\Re_a + \Re_{qs}\Re_a} \tag{2.24}$$

Thus the d-axis flux ϕ_{ds} and q-axis flux ϕ_{qs} are obtained by equations (2.17) and (2.22), respectively.

2.4 Electrical Equivalent Circuit of a PMHS Motor

The stator variables are transformed to the rotor reference frame which eliminates the time varying inductances in the voltage equations. Park's equations [37] are obtained by setting the speed of the stator frame equal to the rotor speed as shown in Fig. 2.6. The expressions for the flux linkages are:

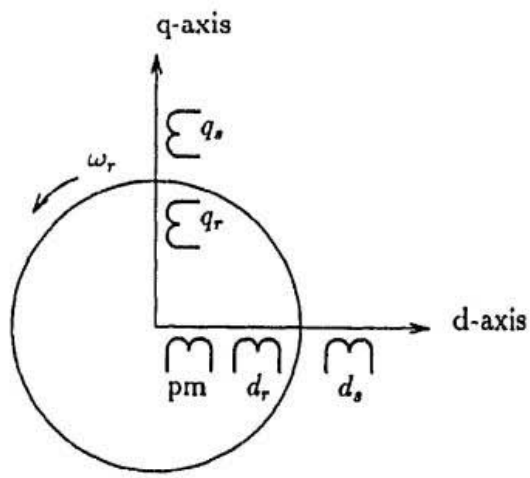

Fig. 2.6 d-q axis model of the PMHS motor

$$\begin{bmatrix} \psi_{ds} \\ \psi_{qs} \\ \psi_{dr} \\ \psi_{qr} \\ \psi_{pm} \end{bmatrix} = \begin{bmatrix} L_{as}+L_{md} & 0 & L_{md} & 0 & L_{md} \\ 0 & L_{as}+L_{mq} & 0 & L_{mq} & 0 \\ L_{md} & 0 & L_{ar}+L_{md} & 0 & L_{md} \\ 0 & L_{mq} & 0 & L_{ar}+L_{mq} & 0 \\ L_{md} & 0 & L_{md} & 0 & L_{apm}+L_{md} \end{bmatrix} \begin{bmatrix} i_{ds} \\ i_{qs} \\ i_{dr} \\ i_{qr} \\ i_{pm} \end{bmatrix} \tag{2.25}$$

In terms of these flux linkages, the motor voltage equations are written as follows:

$$\begin{bmatrix} v_{ds} \\ v_{qs} \\ v_{dr} \\ v_{qr} \\ v_{pm} \end{bmatrix} = \begin{bmatrix} r_s & 0 & 0 & 0 & 0 \\ 0 & r_s & 0 & 0 & 0 \\ 0 & 0 & r_r & 0 & 0 \\ 0 & 0 & 0 & r_r & 0 \\ 0 & 0 & 0 & 0 & 0 \end{bmatrix} \begin{bmatrix} i_{ds} \\ i_{qs} \\ i_{dr} \\ i_{qr} \\ 0 \end{bmatrix} + \frac{d}{dt} \begin{bmatrix} \psi_{ds} \\ \psi_{qs} \\ \psi_{dr} \\ \psi_{qr} \\ \psi_{pm} \end{bmatrix} + \omega_r \begin{bmatrix} -\psi_{qs} \\ +\psi_{ds} \\ 0 \\ 0 \\ 0 \end{bmatrix} \tag{2.26}$$

Since motor and power system parameters are nearly always given in ohms or percent or per unit of a base impedance, it is convenient to express the voltage equation in terms of reactances rather than inductances. Thus the voltage equations become

$$\begin{bmatrix} v_{ds} \\ v_{qs} \\ v_{dr} \\ v_{qr} \\ v_{pm} \end{bmatrix} = \begin{bmatrix} r_s+\frac{p}{\omega_b}x_{ds} & -\frac{\omega_r}{\omega_b}x_{qs} & \frac{p}{\omega_b}x_{md} & -\frac{\omega_r}{\omega_b}x_{mq} & \frac{p}{\omega_b}x_{md} \\ \frac{\omega_r}{\omega_b}x_{ds} & r_s+\frac{p}{\omega_b}x_{qs} & \frac{\omega_r}{\omega_b}x_{md} & \frac{p}{\omega_b}x_{mq} & \frac{\omega_r}{\omega_b}x_{md} \\ \frac{p}{\omega_b}x_{md} & 0 & r_r+\frac{p}{\omega_b}x_{dr} & 0 & \frac{p}{\omega_b}x_{md} \\ 0 & \frac{p}{\omega_b}x_{mq} & 0 & r_r+\frac{p}{\omega_b}x_{qr} & 0 \\ \frac{p}{\omega_b}x_{md} & 0 & \frac{p}{\omega_b}x_{md} & 0 & \frac{p}{\omega_b}x_{md} \end{bmatrix} \begin{bmatrix} i_{ds} \\ i_{qs} \\ i_{dr} \\ i_{qr} \\ i_{pm} \end{bmatrix} \tag{2.27}$$

where ω_b is the base electrical angular velocity used to calculate the inductive reactances: $x_{ds} = x_{\sigma s} + x_{md}$, $x_{qs} = x_{\sigma s} + x_{mq}$ and $x_{dr} = x_{\sigma r} + x_{md}$ and $x_{qr} = x_{\sigma r} + x_{mq}$. The terms x_σ and x_m are generally known as the leakage and magnetizing reactances, respectively. The subscripts *s* and *r* denote the stator and rotor quantities, respectively, and the *d* and *q* are referred to d-axis and *q*-axis, respectively. *p* is the d/dt operator. r_r is the equivalent parallel resistance of rotor hysteresis resistance R_h and eddy current resistance R_e/s, where s is defined as slip during the run-up or asynchronous mode of operation.

The electrical equivalent circuits of the PMHS motor are given in Fig. 2.7 [38].

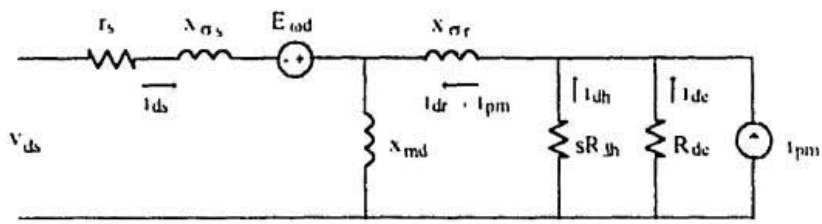

(a) d-axis equivalent circuit

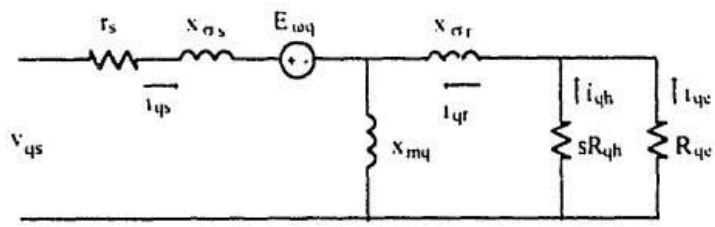

(b) q-axis equivalent circuit

Fig. 2.7 Electrical equivalent circuit of the PMHS motor

The terms $E_{\omega d}$ and $E_{\omega q}$ are given as

$$E_{\omega d}=(1-s)[(x_{as}+x_{mq})i_{qs}+x_{mq}i_{qr}] \tag{2.28}$$

$$E_{\omega q}=(1-s)[(x_{as}+x_{md})i_{ds}+x_{md}(i_{qr}+i_{pm})] \tag{2.29}$$

Based on the parallelogram model of the hysteresis loop, a general equivalent circuit model of the polyphase permanent magnet hysteresis synchronous motor is developed in the d-q axis. The resultant electrical equivalent circuits for both the synchronous and sub-synchronous modes are of the same family as those used to represent the induction machines.

We will now show the usefulness of the electrical equivalent circuits in determining the motor performance and developed power. Stator conductor loss P_{scl} is given as:

$$P_{scl}=r_s(i_{ds}^2+i_{qs}^2) \tag{2.30}$$

Most of the electrical power transferred across the air gap from stator to rotor is converted to mechanical power; the remainder is expended as power losses in the rotor hysteresis material. The power across the airgap P_{gap} is expressed as,

$$P_{gap}=P_{mech}+P_{rhl} \tag{2.31}$$

where P_{mech} is the mechanical developed power and P_{rhl} is the power losses in PMHS motor rotor. The losses in the PMHS motor rotor include:

$$P_{rhl}=sR_{dh}i_{dh}^2+R_{de}i_{de}^2+sR_{qh}i_{qr}^2+R_{qe}i_{qe}^2 \tag{2.32}$$

The total air-gap power delivered to the rotor is

$$P_{gap}=\frac{sR_{dh}R_{de}}{sR_{dh}+R_{de}}i_{dr}^{2}+\frac{sR_{qh}R_{qe}}{sR_{qh}+R_{qe}}i_{qr}^{2} \tag{2.33}$$

Torque calculations can be made from the power calculations. Thus, to determine the electromagnetic torque, T_e, developed by the motor at a speed ω_r (rad/s), one can write

$$P_{mech}=T_e\omega_r \tag{2.34}$$

finally

$$T_e=\frac{P_{mech}}{(1-s)\omega_s} \tag{2.35}$$

where ω_s is the synchronous speed in rad/sec., and s is the slip as defined as:

$$s=\frac{\omega_s-\omega_r}{\omega_s} \tag{2.36}$$

The expression for the electromagnetic torque in the 3-phase 2P-pole motor is also often written in terms of flux linkages and currents.

$$T_e=\frac{3}{2}P(\psi_{ds}i_{qs}-\psi_{qs}i_{ds}) \tag{2.37}$$

During asynchronous speed, the motor torque consists of the hysteresis torque, eddy current torque and permanent magnet brake torque. At synchronous speed the motor torque comprises of the hysteresis and permanent magnet torques. It combines the advantageous features of both the hysteresis and permanent magnet motors. The nagative affect of the magnet brake torque is ideally compensated by the high eddy current torque,

particularly at the initial run-up period.

2.5 State Variable Equation

In the equivalent circuit model, the d-q axis transformation is considered with the fixed reference frame on the rotor axis for all instantaneous speeds, and the permanent magnet or hysteresis material are represented by an equivalent electromotive force (emf). However, there are instances, where the inductances of the PMHS motor do not vary in an ideal sinusoidal fashion and the coefficients of the inductances do not display a certain symmetry. In such cases, transformations do not readily yield solutions to the equations of motion, because the position-dependent terms are not eliminated. With state variable formulation, one is not restricted to the constraints of machine parameters[39]. Furthermore, the time domain model gives directly the transient solution even in the presence of asymmetries and nonlinearities. In order to overcome the highly nonlinear characteristics of the hysteresis material, an attempt has been made in this thesis to derive the PMHS motor equations based on state variable formulations in the time domain.

Fig. 2.8[40] shows the detailed state variable model of a three phase PMHS motor. Each stator winding has a leakage flux and a main flux that links the rotor. The hysteresis phenomenon in an element of the rotor ring is represented by a balanced polyphase winding; and therefore by two orthogonal closed coils, each with the same number of turns as the stator coil pair[40]. The rotor eddy current effect is represented by the equivalent resistance R_e, which is slip independent, and the hysteresis effect is represented by the equivalent resistance R_h, which is slip dependent.

The d-q axis airgap flux equations are written as follows:

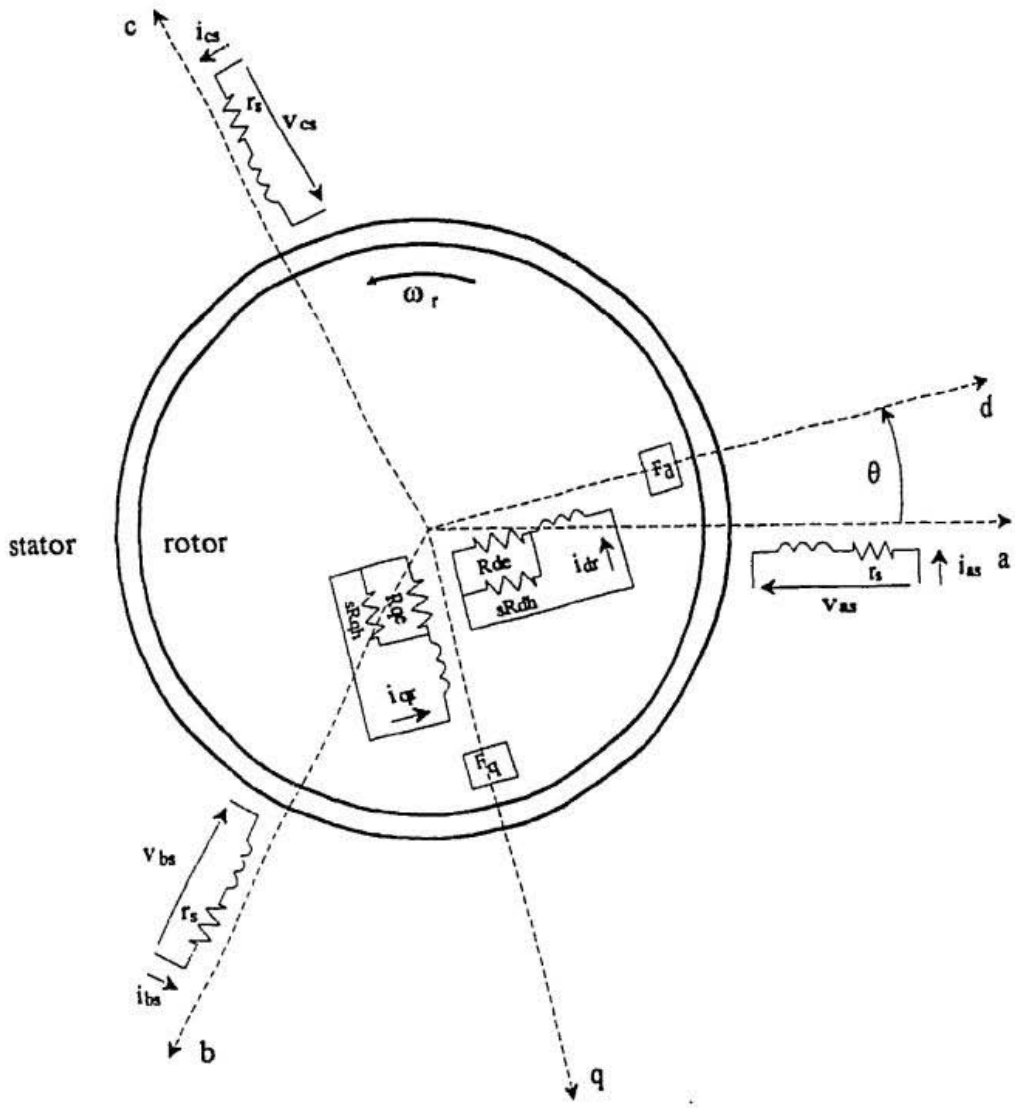

Fig. 2.8 PMHS motor state variable model

$$\phi_{d\delta}=\frac{4}{\pi}\Lambda_d K_\delta K_d K_{wl} W_1[i_{as}\cos\theta+i_{bs}\cos(\theta-\frac{2}{3}\pi)+i_{cs}\cos(\theta+\frac{2}{3}\pi)+i_{dr}]+K_\delta\Lambda_m F_m \tag{2.38}$$

$$\phi_{q\delta}=\frac{4}{\pi}\Lambda_q K_{wl} W_1[i_{as}\sin\theta+i_{bs}\sin(\theta-\frac{2}{3}\pi)+i_{cs}\sin(\theta+\frac{2}{3}\pi)+i_{qr}] \tag{2.39}$$

where i_{as}, i_{bs}, and i_{cs} are the stator currents in phases a, b and c, respectively; i_{dr} and i_{qr} are the d-q axis rotor currents, respectively as shown in Fig. 2.8; K_δ is the factor of fundamental permanent magnet flux; K_d is the factor of the MMF waveform; $K_{wl}W_1$ is the effective series turns per phase of the stator winding; K_{wl} is the fundamental winding factor. The flux linkage equations are given as:

$$\begin{bmatrix}\psi_a\\ \psi_b\\ \psi_c\\ \psi_d\\ \psi_q\end{bmatrix} = K_{wl}W_1 \begin{bmatrix}\cos\theta & \sin\theta\\ \cos(\theta-\frac{2}{3}\pi) & \sin(\theta-\frac{2}{3}\pi)\\ \cos(\theta+\frac{2}{3}\pi) & \sin(\theta+\frac{2}{3}\pi)\\ 1 & 0\\ 0 & 1\end{bmatrix} \begin{bmatrix}\phi_{d\delta}\\ \phi_{q\delta}\end{bmatrix} \tag{2.40}$$

From Fig. 2.8, the voltage equations can be written in the following form:

$$[v]=[r][i]+\frac{d}{dt}[\psi] \tag{2.41}$$

where:

$$[v]=[v_{as}\ \ v_{bs}\ \ v_{cs}\ \ v_{dr}\ \ v_{qr}]^T \tag{2.42}$$

$$[r]=diag.[r_s\ \ r_s\ \ r_s\ \ r_r\ \ r_r] \tag{2.43}$$

$$[i]=[i_{as}\ \ i_{bs}\ \ i_{cs}\ \ i_{dr}\ \ i_{qr}]^T \tag{2.44}$$

$$[\psi]=\begin{bmatrix}\psi_a+L_{os}i_{as}\\ \psi_b+L_{os}i_{bs}\\ \psi_c+L_{os}i_{cs}\\ \psi_d+L_{or}i_{dr}\\ \psi_q+L_{or}i_{qr}\end{bmatrix} \tag{2.45}$$

$$r_r=\frac{R_e(sR_h)}{R_e+(sR_h)} \tag{2.46}$$

Substituting equations (2.38) and (2.39) into equation (2.40), then substituting equation (2.40) into equation (2.45) the flux equation can be written as:

$$[\psi]=[C_1][F]+([L_o]+D_k[C_2]+Q_k[S_1])[i] \tag{2.47}$$

where:

$$[L_o]=\ diag.[L_{os}\ \ L_{os}\ \ L_{os}\ \ L_{or}\ \ L_{or}] \tag{2.48}$$

$$[C_1]=\ diag.[\cos\theta\ \ \cos(\theta-\frac{2}{3}\pi)\ \ \cos(\theta+\frac{2}{3}\pi)\ \ 1\ \ 0] \tag{2.49}$$

$$[F]=\ K_{w1}W_1\Lambda_m F_m[1\ \ 1\ \ 1\ \ 1\ \ 0]^T \tag{2.50}$$

$$D_k=\ \frac{4}{\pi}\Lambda_d K_3 K_d K_{w1}^2 W_1^2 \tag{2.51}$$

$$Q_k=\ \frac{4}{\pi}\Lambda_q K_{w1}^2 W_1^2 \tag{2.52}$$

Matrices $[C_2]$ and $[S_1]$ are given as:

$$[C_2] = \begin{bmatrix} \cos\theta\cos\theta & \cos(\theta-\frac{2}{3}\pi)\cos\theta & \cos(\theta+\frac{2}{3}\pi)\cos\theta & \cos\theta & 0 \\ \cos\theta\cos(\theta-\frac{2}{3}\pi) & \cos(\theta-\frac{2}{3}\pi)\cos(\theta-\frac{2}{3}\pi) & \cos(\theta+\frac{2}{3}\pi)\cos(\theta-\frac{2}{3}\pi) & \cos(\theta-\frac{2}{3}\pi) & 0 \\ \cos\theta\cos(\theta+\frac{2}{3}\pi) & \cos(\theta-\frac{2}{3}\pi)\cos(\theta+\frac{2}{3}\pi) & \cos(\theta+\frac{2}{3}\pi)\cos(\theta+\frac{2}{3}\pi) & \cos(\theta+\frac{2}{3}\pi) & 0 \\ \cos\theta & \cos(\theta-\frac{2}{3}\pi) & \cos(\theta+\frac{2}{3}\pi) & 1 & 0 \\ 0 & 0 & 0 & 0 & 0 \end{bmatrix} \tag{2.53}$$

$$[S_1] = \begin{bmatrix} \sin\theta\sin\theta & \sin(\theta-\frac{2}{3}\pi)\sin\theta & \sin(\theta+\frac{2}{3}\pi)\sin\theta & 0 & \sin\theta \\ \sin\theta\sin(\theta-\frac{2}{3}\pi) & \sin(\theta-\frac{2}{3}\pi)\sin(\theta-\frac{2}{3}\pi) & \sin(\theta+\frac{2}{3}\pi)\sin(\theta-\frac{2}{3}\pi) & 0 & \sin(\theta-\frac{2}{3}\pi) \\ \sin\theta\sin(\theta+\frac{2}{3}\pi) & \sin(\theta-\frac{2}{3}\pi)\sin(\theta+\frac{2}{3}\pi) & \sin(\theta+\frac{2}{3}\pi)\sin(\theta+\frac{2}{3}\pi) & 0 & \sin(\theta+\frac{2}{3}\pi) \\ 0 & 0 & 0 & 0 & 0 \\ \sin\theta & \sin(\theta-\frac{2}{3}\pi) & \sin(\theta+\frac{2}{3}\pi) & 0 & 1 \end{bmatrix} \tag{2.54}$$

Substituting flux equation (2.47) into voltage equation (2.41), the new voltage equation is written as:

$$\begin{aligned} [v] = [r][i] + (D_k\frac{d}{dt}[C_2] + Q_k\frac{d}{dt}[S_1])[i] \\ + ([L_a] + D_k[C_2] + Q_k[S_1])\frac{d[i]}{dt} + \frac{d[C_1]}{dt}[F] \end{aligned} \tag{2.55}$$

The expression for electromagnetic torque is written as:

$$\begin{aligned} T_e = P\psi_d[i_{as}\sin\theta + i_{bs}\sin(\theta-\frac{2}{3}\pi) + i_{cs}\sin(\theta+\frac{2}{3}\pi)] \\ - P\psi_q[i_{as}\cos\theta + i_{bs}\cos(\theta-\frac{2}{3}\pi) + i_{cs}\cos(\theta+\frac{2}{3}\pi)] \end{aligned} \tag{2.56}$$

Thus, the state variable equations are written as follows:

$$
\begin{aligned}
\frac{d}{dt}[i] &= ([L_n]+D_k[C_2]+Q_k[S_1])^{-1}\{[v]-\frac{d[C_1]}{dt}[F] \\
&\quad -([r]+D_k\frac{d}{dt}[C_2]+Q_k\frac{d}{dt}[S_1])[i]\} \\
\frac{d}{dt}\omega_r &= \frac{1}{J}(T_e-B_0\omega_r-T_l) \\
\frac{d}{dt}\theta &= P\omega_r
\end{aligned}
\tag{2.57}
$$

where J is the rotational inertia. Current i, rotor angular speed ω_r and rotor angle θ are taken as state variables.

Theoretical prediction for the PMHS motor performance has been achieved by solving the state variable equation (2.57) numerically by FORTRAN program. The experimental PMHS motor was tested using the 5 hp Mawdsley machine set in the open loop mode of operation. The permanent magnet hysteresis rotor was inserted in the Mawdsley machine stator. The stator was wound for 3-phase, 60-Hz, delta-connected in 4-pole for 208 V operation. The detailed design data, parameters of the PMHS motor and the flow chart of the numerical calculation of the state variable equation are given in appendix A and appendix B, respectively.

Fig. 2.9 shows the open loop starting process of the PMHS motor. Figs. 2.9(a) and (b) show the computed and test speed versus-time responses. It is interesting to note that the experimental speed response is smoother than the simulation one. Usually theoretical results are better fit than the experimental one. Because of the constant parameter model the computed speed versus-time response has more oscillation than the test one [34]. Unlike conventional hysteresis motors, once the speed reaches the

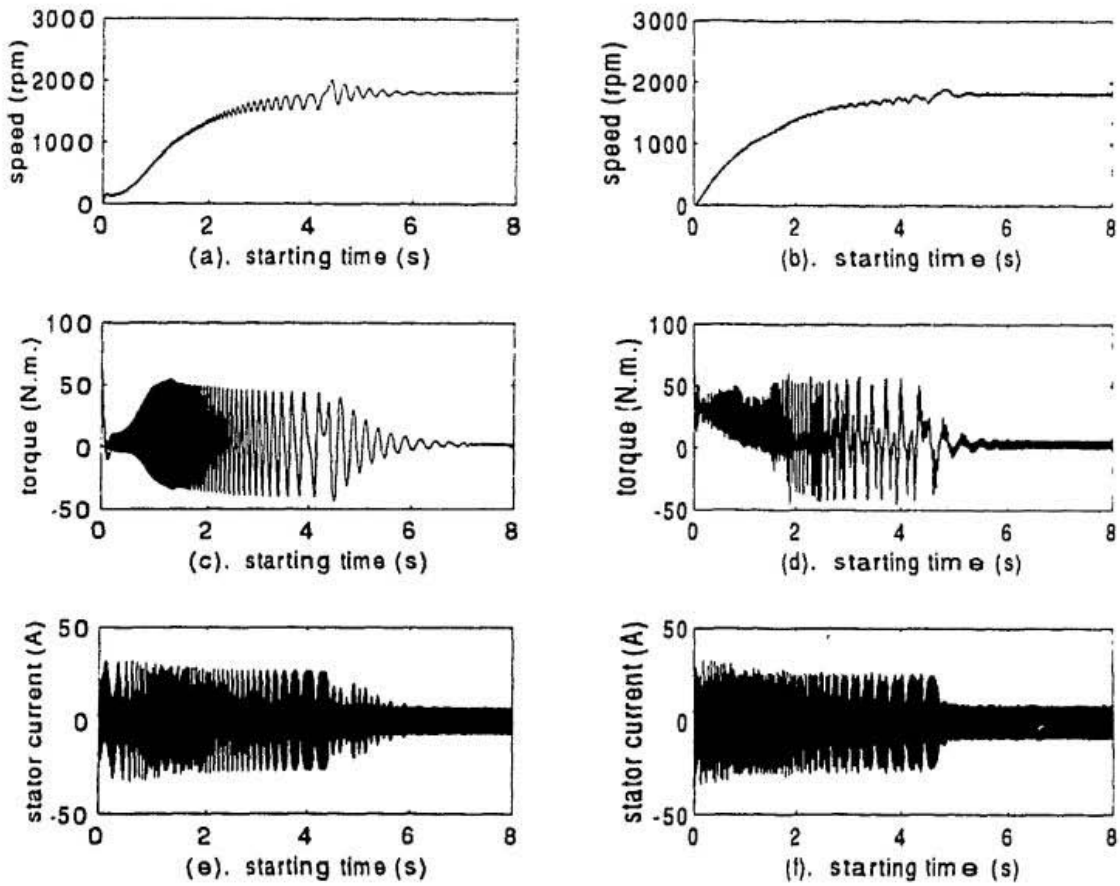

Fig. 2.9 Open loop starting process of the PMHS motor

(a) computed speed vs time response (b) test speed vs time response

(c) computed torque vs time response (d) test torque vs time response

(e) computed current vs time response (f) test current vs time response

synchronous state, the speed curve becomes quite smooth without any oscillation and there is also no flutter around the synchronous speed.

Figs. 2.9(c) and (d) show the variations of computed and test torques with time during the run-up and synchronizing period at no load condition with the dc loading machine coupled to the shaft. It is evident that during the run-up process, the accelerating torque of the PMHS motor is produced primarily by the hysteresis and eddy-current torque components. Once the rotor reaches synchronous speed, the rotor flux ceases to sweep around it. The eddy-current torque disappears, and the motor behaves as a superior hysteresis motor. It is clear from the torque responses of Figs. 2.9(c) and (d) that the starting and synchronization are quite smooth.

Figs. 2.9(e) and (f) show the computed and test values of the stator current with time at rated voltage and frequency. The magnitudes of the computed and experimental motor currents differ by 7% during the worst states of the synchronizing process. It is evident from the results that the starting and synchronization process of the PMHS motor can be observed by measuring the stator current alone.

It is to be noted that there exist good agreements between the experimental and simulation results of the speed and starting current responses. There are two reasons for the difference between the experimental and the computed torque responses. One is due to the inherent linearization, assumption of the parallelogram hysteresis loop and constant equivalent parameter model which give rise to some calculation errors especially in the very beginning of the starting process. Secondly there is some noise in the amplified signal obtained from the torque transducer connected between the test PMHS motor and

the loading machine. However, there is a reasonably identical trend between the simulation and test torque responses during the accelerating process. Once the rotor reaches the synchronous state, the test and simulated torque results are clearly identical.

2.6 Summary

This chapter started with the presentation of the permanent magnet and hysteresis models. Based on the parallelogram model of the hysteresis loop and by making a number of assumptions and approximations, general magnetic and electrical equivalent circuits of the PMHS motor have been developed in both d- and q-axis. A comprehensive analysis of the PMHS motor has been developed using the magnetic and electrical equivalent circuits.

A time domain model of the PMHS motor for the steady state and run-up performances has been developed. Using a state variable method, analytical expressions have been derived to predict the starting performances of the PMHS motor. Reasonably good agreements between the computed and experimental results of a 5hp PMHS laboratory motor confirm the validity of the proposed analysis.

Chapter 3

Programmed Pulse Width Modulation in the PMHS Motor Drive

3.1 Introduction

The function of an inverter is to change a dc input voltage to a symmetrical ac output voltage of desired magnitude and frequency. The output voltage could be fixed or variable at a fixed or variable frequency. A variable output voltage can be obtained by varying the input dc voltage and maintaining the gain of the inverter constant. On the other hand, if the dc input voltage is fixed and it is not controllable, a variable output voltage can be obtained by varying the gain of the inverter, which is normally accomplished by pulse-width-modulation (PWM) control within the inverter. The inverter gain may be defined as the ratio of the ac output voltage to dc input voltage.

The output voltage waveforms of ideal inverters should be sinusoidal. However, the waveforms of practical inverters are nonsinusoidal and contain certain harmonics. For low and medium power applications, square wave voltage may be acceptable; and for high power application, low distortion sinusoidal wavef orms are required. With the

availability of high speed power semiconductor devices, the harmonic contents of output voltage can be minimized or reduced significantly by sinusoidal pulse width modulation (SPWM) techniques.

Traditionally, an analog current or voltage regulator has been used in an ac motor vector control system. In such a regulator, the current or voltage command generated from the digital controller is converted into analog signals and compared with the analog feedback signals to produce switching signals for the inverter. Typical examples of such schemes include the hysteresis current regulator, bang-bang control and the voltage sinusoidal pulse width modulation in which the width of each pulse is varied in proportion to the amplitude of a sine wave evaluated at the center of the same pulse.

Owing to the rapid advancement in computer technology, more and more powerful microprocessors and digital signal processors are becoming available. It becomes possible to implement the voltage pulse width modulation in the digital domain with the advantages of higher flexibility and higher level of system integration.

First, the operation of the PWM inverter will be discussed. This serves as a brief review of the PWM and presents a theoretical analysis of its efficiency. Also, this section presents the basic structure of the voltage source inverter, the principle of the voltage pulse width modulation technique and its limitations. Finally, experimental results of a DSP based voltage space vector PWM are given.

3.2 Sinusoidal Pulse Width Modulation

The pulse width modulation technique in an inverter system can move unwanted

frequency components to a higher frequency region, i.e., the sidebands of a carrier frequency. Thus the output waveform of a PWM inverter is generally improved by using a high ratio between the carrier frequency and the output fundamental frequency, and the distortion factor and lower-order harmonics are reduced significantly. Because most ac motors are designed to operate on a sine wave supply, the inverter output voltage should be as nearly sinusoidal as possible. It seems obvious, therefore, that the three-phase reference should be sine wave reference, in order to give a PWM waveform in which the pulse width is sinusoidally modulated throughout the cycle. This is termed sinusoidal PWM. The gate signals as shown in Fig. 3.1 [41] are generated by comparing a sinusoidal reference signal with a triangular carrier wave of frequency f_c. This type of modulation is commonly used in industrial applications and abbreviated as SPWM. The frequency of the reference signal f_r, determines the inverter output frequency f_o. Its peak amplitude A_r, controls the modulation index M, and then in turn the rms output voltage V_o. The number of pulses per half-cycle depends on the carrier frequency. For large carrier ratios, the sinusoidal PWM inverter delivers a high quality output voltage waveform in which the dominant harmonics are of a high order, being clustered around the carrier frequency and its harmonics. Smooth motor rotation is obtained, even at low speed, because the undesirable low-order harmonics and troublesome torque pulsations are minimized with a sinusoidal PWM supply.

The rms output voltage can be varied by varying the modulation index $M = A_r/A_c$. This variation alters the pulse widths in the output voltage waveform but preserves the sinusoidal modulation pattern. It can be observed that the area of each pulse corresponds

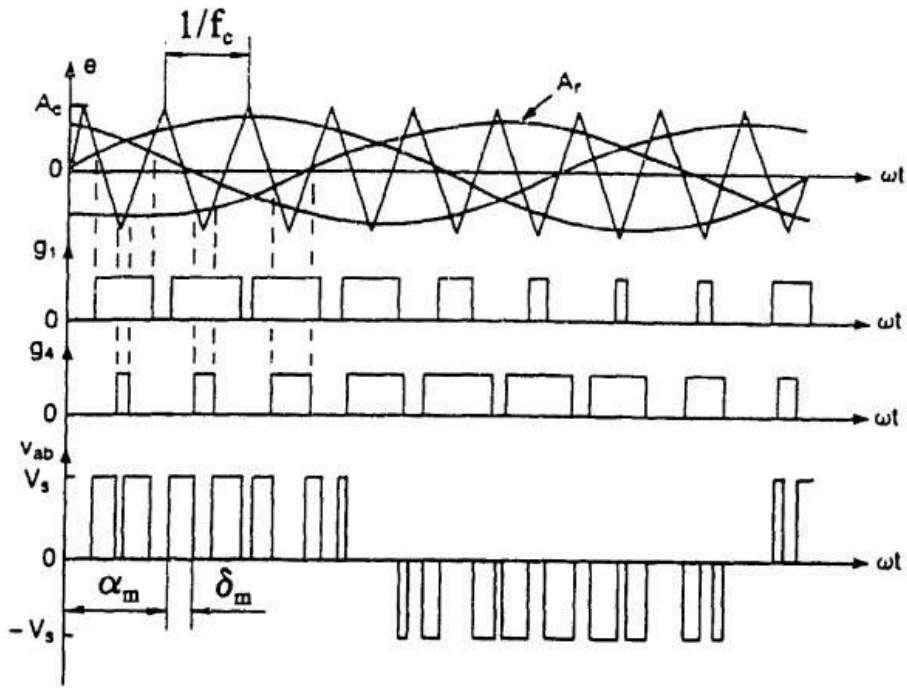

Fig. 3.1 Sinusoidal pulse-width modulation for three-phase inverter [41]

approximately to the area under the sine wave between the adjacent midpoints of off-periods on the gate signals. If δ_m is the width of mth pulse, the rms output voltage

$$V_o = V_s \left[\sum_{m=1}^{p} \frac{\delta_m}{\pi} \right]^{\frac{1}{2}} \qquad (3.1)$$

where p is the number of pulses per half-cycle. Equation (3.1) can also be applied to determine the Fourier coefficient of output voltage as

$$B_n = \sum_{m=1}^{p} \frac{2V_s}{n\pi} \sin\frac{n\delta_m}{2} \left[\sin n\left(\alpha_m + \frac{\delta_m}{2}\right) - \sin n\left(\pi + \alpha_m + \frac{\delta_m}{2}\right) \right] \qquad (3.2)$$

$$\text{for } n = 1,3,5,\ldots$$

where α_m is the angle from initial point to the mth pulse.

The output voltage of an inverter contains harmonics. However, the SPWM pushes the harmonics into a high frequency range around the switching frequency f_c and its multiples, that is, around harmonics m_f, $2m_f$, $3m_f$, and so on. The frequencies at which the voltage harmonics occur can be related by

$$f_n = (jm_f \pm k) f_c \qquad (3.3)$$

$$\begin{aligned} n &= jm_f \pm k \\ &= 2jp \pm k \end{aligned} \qquad (3.4)$$

$$\text{for } j = 1,2,3,\ldots \text{and } k = 1,3,5,\ldots$$

The peak fundamental output voltage for the PWM and SPWM control can be found approximately as

$$V_{m1} = dV_s \qquad \text{for } 0 \le d \le 1.0 \qquad (3.5)$$

For $d = 1$, equation (3.5) gives the maximum peak amplitude of the fundamental output

voltage as $V_{m1(max)} = V_s$. But according to Fourier analysis, $V_{m1(max)}$ could be as high as $4V_s/\pi = 1.278V_s$ for a square wave output. In order to increase the fundamental output voltage, d must be increased beyond 1.0. The operation for $d > 1.0$ is called over modulation. Some of the intersections between the reference and carrier waves are lost; and as a result, pulses are dropped in the output voltage waveform. For large values of M, the only intersections are those at the zero crossings of the sine wave. The value of d at which $V_{m1(max)}$ equals $1.278V_s$ is dependent on the number of pulses per half-cycle p. Over modulation basically leads to a square wave operation and adds more harmonics as compared to operation in the linear range (with $d \leq 1.0$). Over modulation is normally avoided in applications requiring low distortion.

The adjustable frequency operation of a sine PWM inverter for ac motor control requires the generation of a set of three-phase sine wave reference voltages of adjustable amplitude and frequency. If the motor is to operate at very low speeds, the reference wave must have a corresponding low frequency capability. With traditional analog circuit techniques, it is difficult to generate such a low frequency sine wave reference without encountering problems of dc offset and parameter drift.

3.3 Voltage Space Vector

The most frequently used three-phase inverter circuit consists of three legs, one for each phase, as shown in Fig. 3.2(a). The switching elements are power bipolar junction transistors (BJTs). The points labelled a, b, and c are connected directly to the motor coils to generate the actual three-phase voltage.

To simplify the analysis of the inverter, each leg, or phase, in the inverter is considered as a logical switch having only two states, as shown in Fig. 3.2(b). With 3 logical switches the inverter can have only 8 different states, state "1", if one of the upper devices is "ON", and state "0" if one of the lower devices is "ON". The logical relations are shown in table 3.1.

Table 3.1 Logical state of inverter

Inverter state n	a b c
0	0 0 0
1	1 0 0
2	1 1 0
3	0 1 0
4	0 1 1
5	0 0 1
6	1 0 1
7	1 1 1

To generate the desired sinusoidal pulse width modulation voltage output of the inverter, the pulse width of each phase voltage output is modulated by controlling the ON/OFF time duration of the upper or lower transistors switches. Using the voltage source inverter as shown in Fig. 3.3, to supply the stator of the PMHS motor with the desired

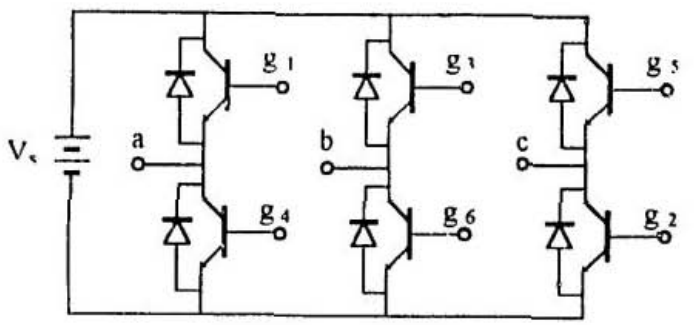

(a)

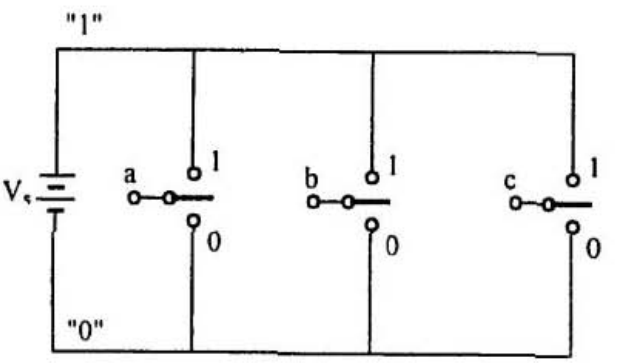

(b)

Fig. 3.2 Three-phase inverter

(a) three phase inverter

(b) logical switches of the inverter

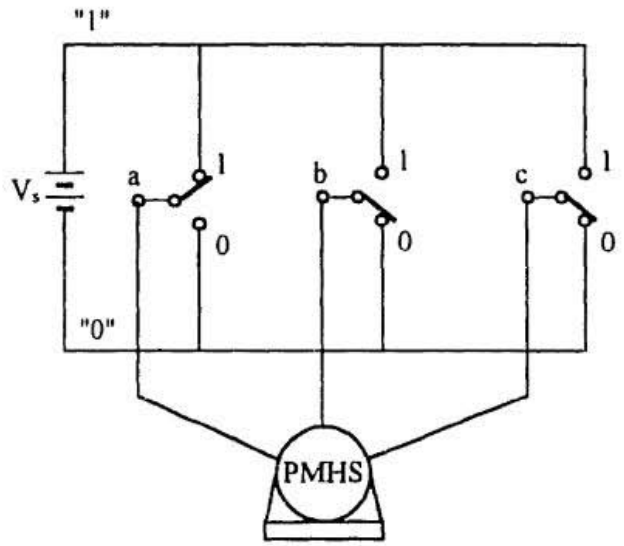

Fig. 3.3 Three-phase voltage source inverter

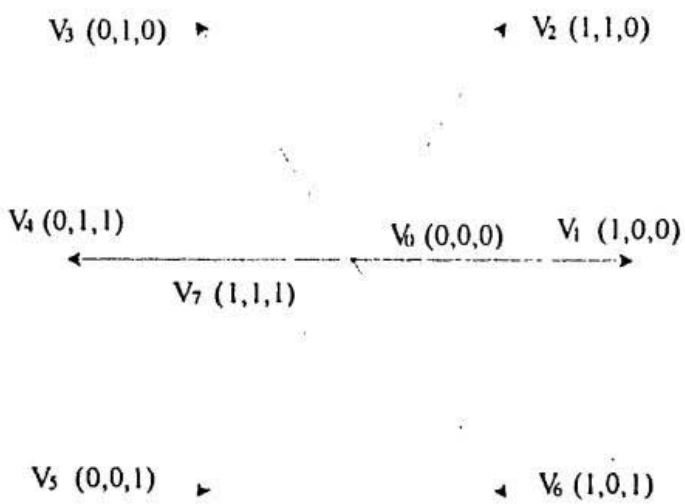

Fig. 3.4 Voltage space phasors

complex voltage vectors, only eight possible complex voltage vectors can be generated, as shown in Fig. 3.4. It shows that the PWM voltage source inverter provides six nonzero and two zero discrete voltage vectors. If line voltages V_a, V_b and V_c are chosen in the same line with the vectors V_1, V_3 and V_5, respectively, then the desired voltage vector V_{ref} will be

$$V_{ref} = \frac{2}{3}\left(V_a + V_b e^{-\frac{j2\pi}{3}} + V_c e^{\frac{j2\pi}{3}}\right) \qquad (3.6)$$

The voltages V_a, V_b, and V_c are easy to determine, if the triplets of conducting transistors in the inverter are identified, in accordance with Table 3.2.

Table 3.2 Voltage vector of a PWM voltage source inverter

	V_0 (000)	V_1 (100)	V_2 (110)	V_3 (010)	V_4 (011)	V_5 (001)	V_6 (101)	V_7 (111)
V_a	0	$2/3V_s$	$1/3V_s$	$-1/3V_s$	$-2/3V_s$	$-1/3V_s$	$1/3V_s$	0
V_b	0	$-1/3V_s$	$1/3V_s$	$2/3V_s$	$1/3V_s$	$-1/3V_s$	$-2/3V_s$	0
V_c	0	$-1/3V_s$	$-2/3V_s$	$-1/3V_s$	$1/3V_s$	$2/3V_s$	$1/3V_s$	0

Any desired stator voltage vector V_{ref} can be expressed by a weighted combination of the vectors shown in Fig. 3.5.

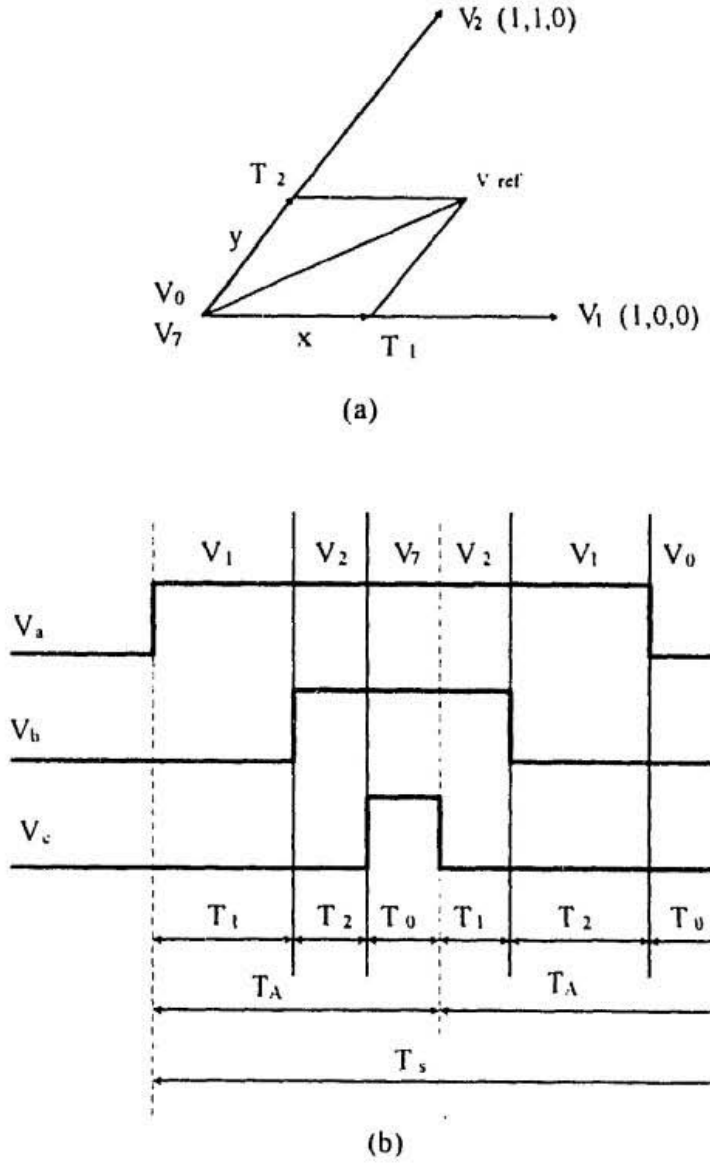

Fig. 3.5 Voltage space vector

(a) Voltage vectors and weighting factors

(b) Weighted average of voltage vectors

$$V_{ref} = xV_i + yV_{i+1} + zV_{0,7} \qquad (3.7)$$

where, x, y and z are weighting factors, subscript i =1, 2 ... 5. [42]

To achieve good tracking of V_{ref} and a constant switching frequency, the choice of the appropriate synthesizing vectors, V_0, V_1, ..., V_7 should meet the following requirements:

1) minimum deviation from the desired V_{ref};

2) minimum switching during one cycle time.

The first requirement is met if the two vectors adjacent to the desired vector V_{ref} are chosen. The second requirement is met when the switching sequence is arranged in such a way that each inverter leg is commuted only once during a switching cycle. This can be achieved by appropriately choosing the vectors V_0 and V_7 as two of the weighted vectors. So equation (3.7) has to meet following conditions.

$$x = \frac{T_1}{T_A} \; ; \quad y = \frac{T_2}{T_A} \; ; \quad z = \frac{T_o}{T_A} \qquad (3.8)$$

$$T_1 + T_2 + T_0 = T_A$$

The calculation of V_{ref}, T_1, T_2, and T_0 may be done on a digital signal processor, but it requires a considerable computation effort and a good knowledge of the motor parameters. Making alternate use of the two zero vectors V_0 and V_7 it is possible to achieve any small weighting factors (x, y, z) without violating the restrictions imposed by commutation time or maximum inverter frequency. After switching one inverter phase to the high level, the following vector and the next zero vector are not obtained by

switching the same phase back to low, but by synchronously switching the other two phases to high. Fig. 3.5(b) shows the inverter phase voltages for a given reference voltage V_{ref}; according to Fig. 3.5(b), it is possible to get the vectors V_1 or V_2 for any time interval, which can be much smaller than the time T_A (T_A is imposed by the switching frequency of the inverter, and T_A is 1/2 T_s).

3.4 The Generation of Digital PWM Signals

In this thesis, PWM signals are generated digitally using the DS1102 DSP board, which is built around the Texas Instruments TMS320C31 floating point digital signal processor and a TMS320P14 DSP microcontroller. The TMS320P14 DSP has a hardware subsystem capable of generating PWM output signals. This subsystem can be controlled by some of the slave's on-chip registers. Thus it is not necessary to load a slave application in order to use PWM, as access to the on-chip registers is already supported by the EPROM firmware. To control and set the duty cycle the communication software in the on-chip EPROM can be used. The function *ds1102_p14_pwm_init()* is used to initialize the slave-DSP's high precision PWM mode. The function *ds1102_p14_pwm_14 (long channel, float value)* alters the duty cycle of the specified PWM *channel*. The *channel* number corresponds to the TMS320P14 compare output channels. The *float value* must be in the range -1.0 to +1.0 and represents a duty cycle of 0 to 100%.

The generation of the three-phase sinusoidal output of the PWM signals is based on the pulse width modulation. This type of modulation requires a duty cycle arrangement which is shown in Fig. 3.6, in which T_{PWM} denotes the inverter period. It

is not possible to generate such duty cycles with the TMS320P14, since this DSP starts its PWM channels simultaneously, as shown in Fig. 3.7 where the PWM_a and PWM_1 represent PWM output channels of the DSP board. Since the DSP provides six PWM channels (PWM_0 through PWM_5) the problem could be solved if two channels are used to generate one PWM inverter duty cycle. For example, the generation of PWM_a is performed by PWM_0 and PWM_1. The channels are programmed in such a way that the pulse width of PWM_0 is equal to the first pause width of PMW_a. The pause width of PWM_1 is equal to the pulse width of PWM_0, because PMW_a is symmetric to $T_n + T_{PWM}/2$. Both channels are connected with an exclusive OR-gate. The output of this gate provides the required PWM inverter duty cycle. Fig. 3.8 illustrates the duty cycle generation. The output PWM signals are programmed so that the resulting pulse has a width proportional to the desired voltage and is centered within the sampling interval. At each sampling instant, the PWM signals are reprogrammed to reflect the new value of the desired voltage. The waveforms produced are identical to the ones generated by the conventional method.

The processor is provided with a 25 MHz clock. Therefore, the timer register 2 which is used to generate the period clock, has a cycle time of 160 ns. The PWM channels are used in the high resolution 14 bit and frequency 1.506 kHz mode. Since a period of $T_{PWM} = 664 \times 10^{-6}$ s is required, the timer register must be loaded with

$$time\ register = \frac{664 \times 10^{-6} s}{160 \times 10^{-9} s} = 4150 \qquad (3.9)$$

To get a pulse width of 664 μs the action register of PWM channel i must be loaded with

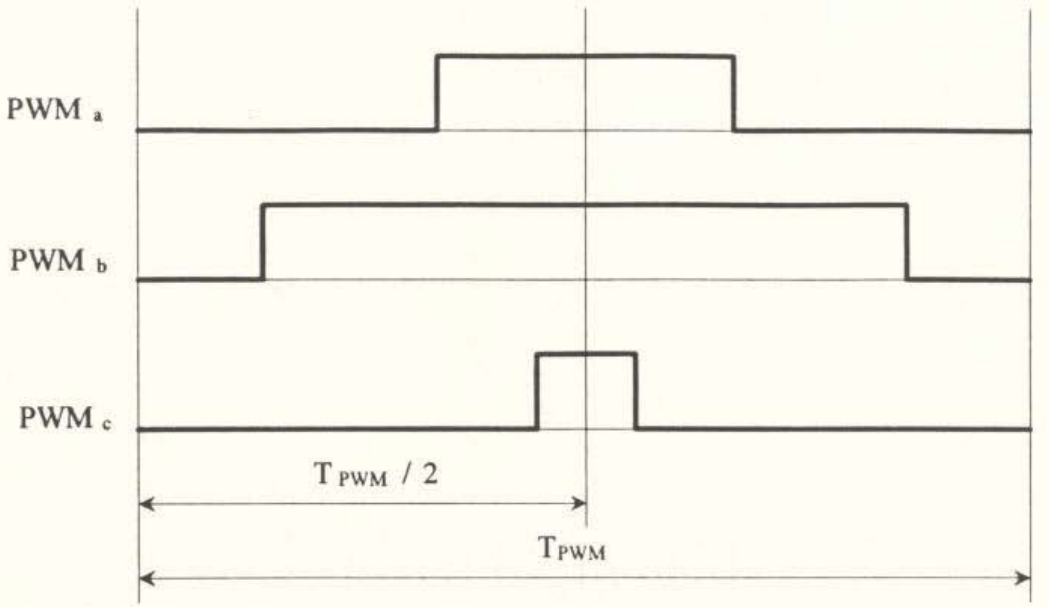

Fig. 3.6 PWM inverter duty cycle arrangement

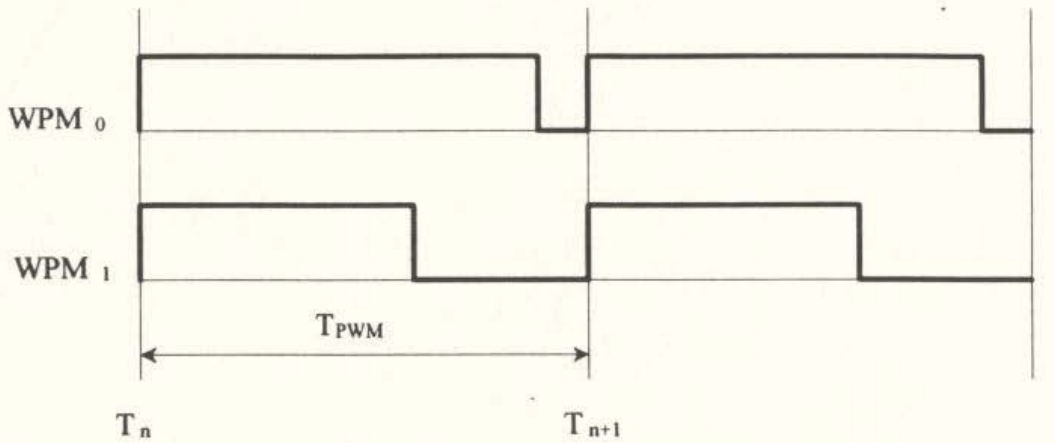

Fig. 3.7 TMS320P14 PWM channel behaviour

$$action\ register_i = \frac{664\times10^{-6}s}{40\times10^{-9}s} = 16600 \qquad (3.10)$$

The following example describes only the calculation of PWM channels 0 and 1, since the other computations are identical. PWM channel 0 (PWM_0) is used only for the first half period $T_{PWM}/2$. The maximum pulse width of PWM_0 must be reached if u_a=-1.0 where u_a is a parameter in Equation (3.11). On the other hand, the pulse width of PWM_0 must be minimal, if $u_a \approx 1.0$. The computation of the capture register is done according to the following equation

$$action\ register_0 = -4149 \cdot u_a + 4150 \qquad (3.11)$$

As the pause width of the second PWM channel (PWM_1) is identical to the pulse width of PWM_0, a subtraction will provide the required register value:

$$action\ register_1 = 16600 - action\ register_0 \qquad (3.12)$$

The variation of PWM duty cycles for $u_a \approx -1$ and $u_a \approx 1$ is shown in Fig. 3.9. For the convenience of real time control, the maximum pulse width PA_{max} is taken as 1, and the minimum of pulse width PA_{min} is taken as 0. The experimental result of the PWM duty cycle for pulse width PA=0.1 and PA=0.9 are shown in Fig. 3.10. PWM_0 and PWM_1 are the output signals of the DSP board. PWM_a is the ideal PWM signal of phase *a* for the voltage source inverter.

When viewed in the frequency domain, the PWM system is seen to be a modulation system. The carrier frequency is the triangular frequency while the modulating waveform is the reference voltage waveform. Two important quantities are

the modulation index M which is the ratio of the amplitude of the reference signal to the amplitude of the carrier triangular wave; and p which is the ratio of the carrier wave frequency to the reference signal frequency. For p sufficiently large and for $0 \leq M \leq 1$, it is known that the pulse widths are linearly related to the modulation index.

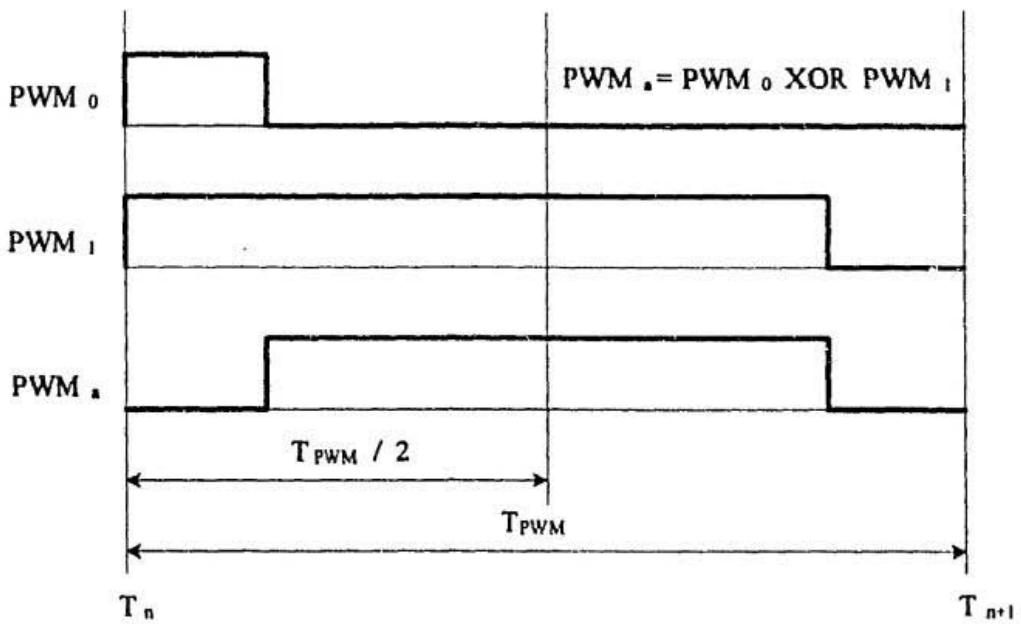

Fig. 3.8 PWM duty cycle generation

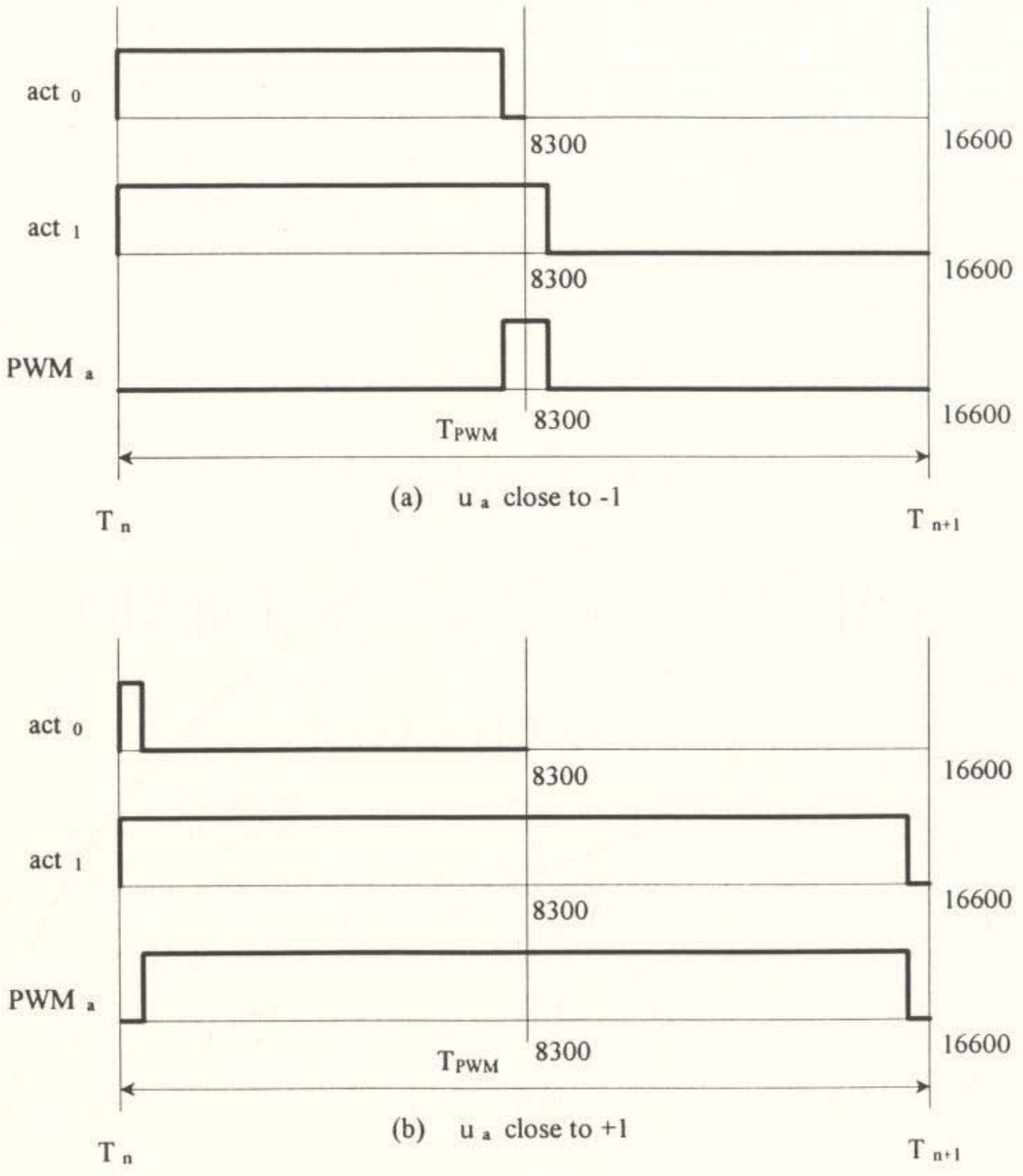

Fig. 3.9 The variation of PWM duty cycle

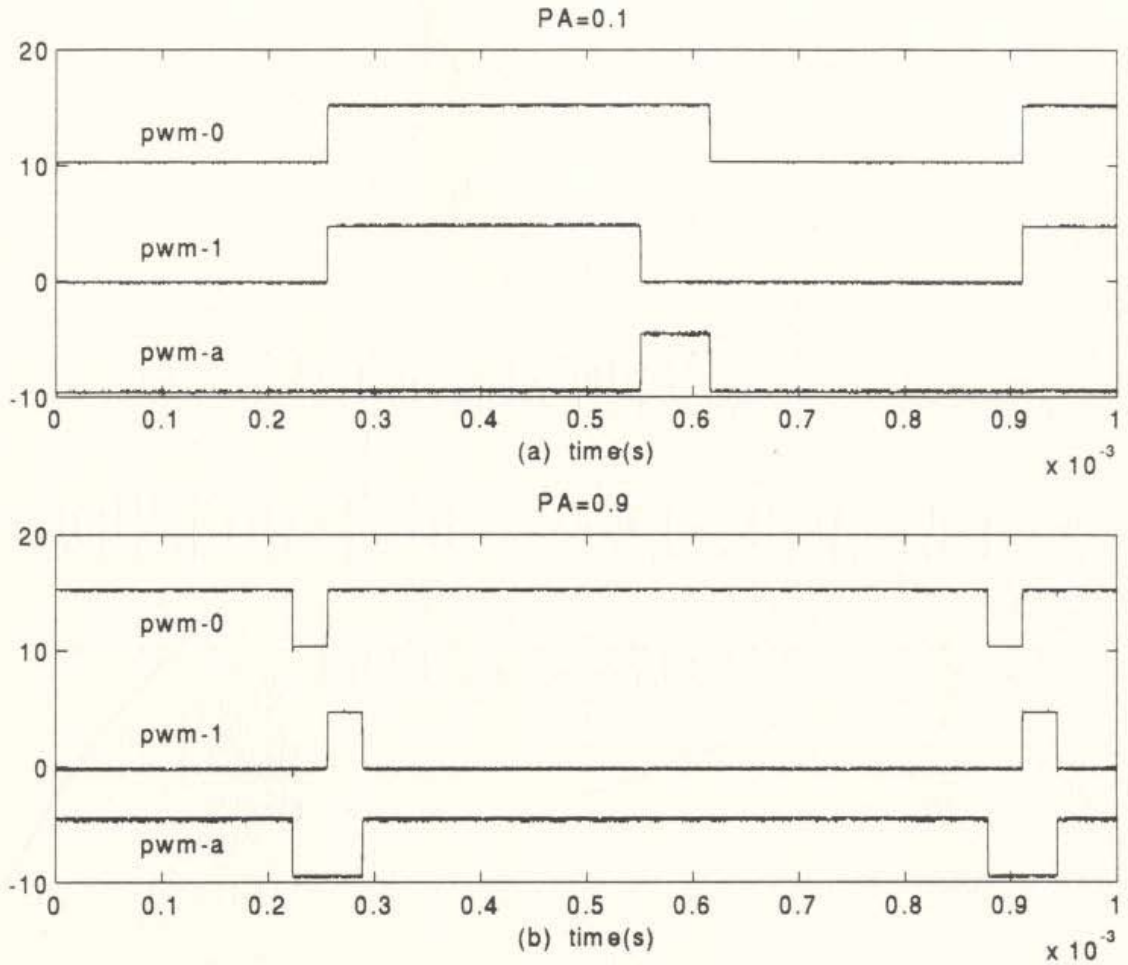

Fig. 3.10 Experimental PWM duty cycle

(a) pulse width PA = 0.1; (b) pulse width PA = 0.9

3.5 The Operation of the Voltage Source Inverter

The voltage source inverter is shown in Fig. 3.2(a). The switching elements are power bipolar junction transistors (BJTs). The points labelled a, b and c are connected directly to the motor stator terminals. Since the operation of each leg is identical, consider the generation of V_a. Ideally, for PWM operation, V_a is connected to either "1" or "0" by alternately enabling either the upper or the lower BJT. Due to the finite switching time of the BJT's and the possible skew in the base command paths, the conducting BJT must be turned off before the other one, which is in the same leg, is turned on in order to guarantee that they do not both conduct simultaneously and short the power supply terminals together. This delay is called the shoot through-delay. During the shoot through-delay, the diodes which are connected across BJT's *e* and *c* provide a closed path for the circulating current of the inductive load. Thus, the switching of V_a between the supply rails not only depends upon the gate command to the BJT's, but also on the direction and the magnitude of the load current.

The TMS320P14 PWM channel waveform is shown in Fig. 3.7. Six-channel digital PWM generation takes 81 μs DSP time. Because the execution time of control software is a big concern, the generation of the PWM duty cycle and shoot-through delay are achieved by hardware instead of software. In order to generate the PWM duty cycle as shown in Fig. 3.8, exclusive OR gates are used. The shoot-through delay is achieved by a monostable multivibrator. The interface circuit between the DSP board and the voltage source inverter is shown in Fig. 3.11. The input signals of the circuit, PWM_0, PWM_1, ...and PWM_5, are the six PWM channel outputs of the DSP board. By exclusive

OR logic operation, PWM_a, PWM_b and PWM_c duty cycles are generated. Then the duty cycles go through the shoot through delay circuit. Finally, the six gate signals of the voltage source inverter are generated, as shown in Fig. 3.11(a). For jitter-free operation of the monostable multivibrator, as shown in Fig. 3.11(b), resistance R_t should be in the range of 2kΩ to 40kΩ and C_t should be between 10nF and 10μF. Using these ranges of values, the shoot-through delay time is approximately $T=0.7R_tC_t$. The voltage source inverter used in this thesis requires a shoot through-delay time of 40μs. Thus a value of 6.8kΩ is chosen for resistance R_t and 0.01μF is chosen for capacitance C_t. A detailed timing diagram and all the logic relations are shown in Fig. 3.12.

A detailed analysis of the logic relations of the switching sequence in two PWM periods will now be discussed. Since the system is symmetrical, it suffices to explain the behaviour of only one leg of the inverter. Referring to Fig. 3.12, the six consecutive timing zones are described. In the first timing zone, both the DSP first two channels output PM_0 and PM_1 are high. The exclusive OR logic operation is taken for these two signals by the transistor-transistor logic (TTL) 7486 exclusive OR gate. Thus, PM_a, the desired inverter phase *a*'s output of upper BJT is low. The PM_a inverse, the desired phase *a*'s output of lower BJT is high. Interval two begins as PM_0 becomes low and ends when PM_1 is low. After the exclusive OR logic operation of PM_0 and PM_1, the desired output of PM_a is high. The 40μs wide pulse is generated by the TTL 74121 monostable multivibrator circuit, as shown in Fig. 3.12 waveform m1. Notice that the m1 pulse is started from the PM_a's rising edge. Interval three begins as the PM_1 goes low. So, PM_a goes low, and inverse of PM_a goes high. The pulse m4 is generated immediately from

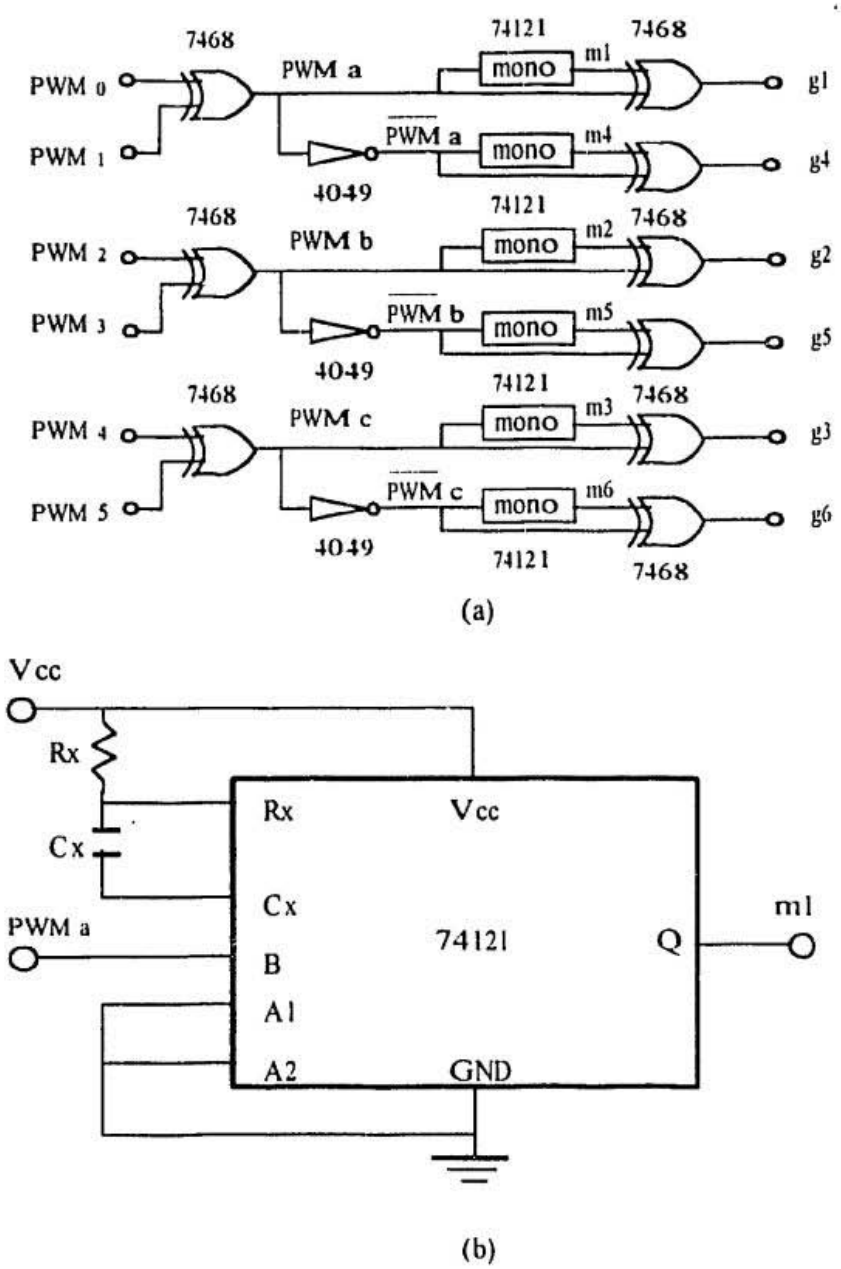

Fig. 3.11 DSP and inverter interface circuit

(a) gate signal generation circuit (b) monostable multivibrator

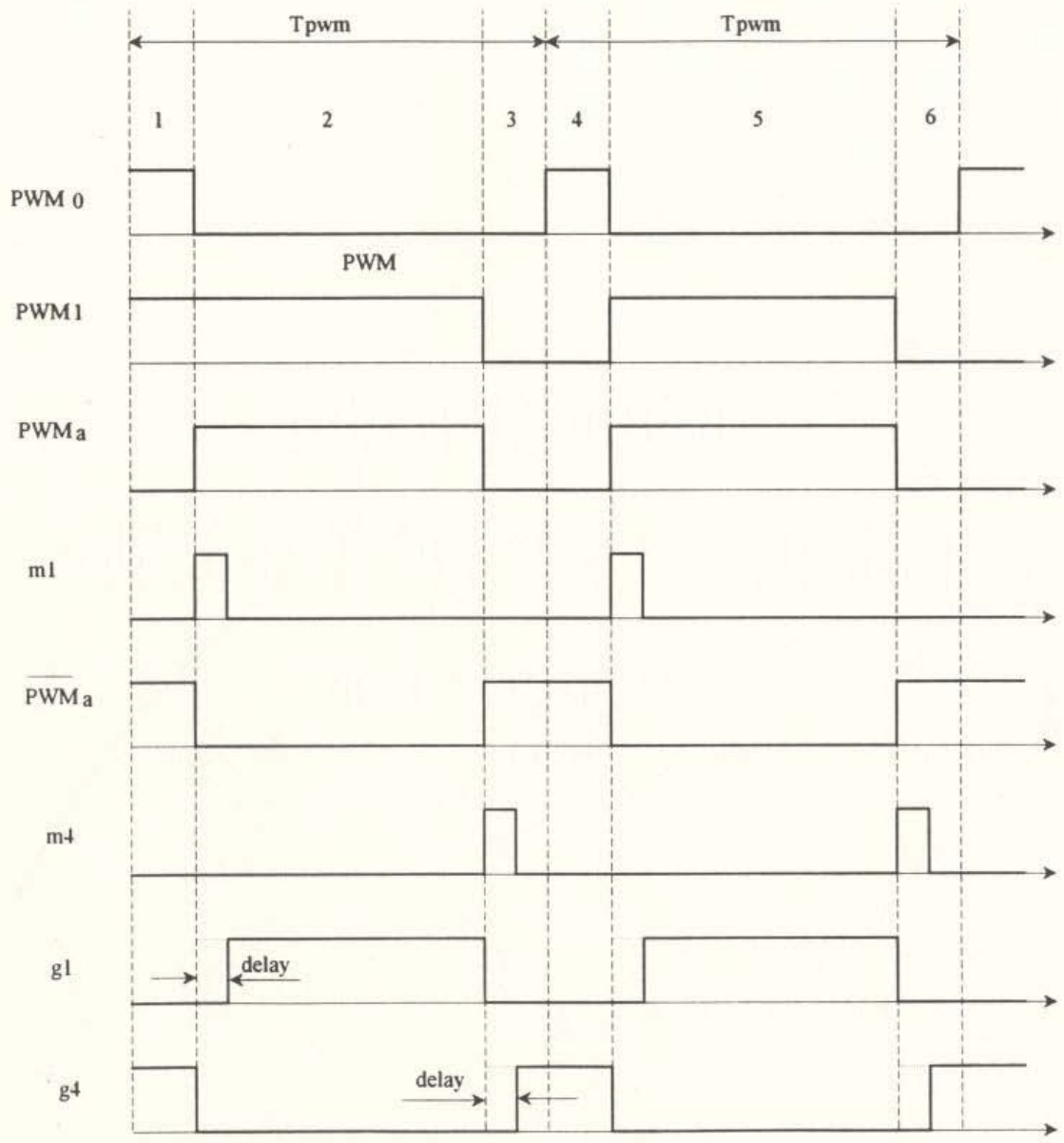

Fig. 3.12 PWM logic relations of a switching sequence

the rising edge of the PM_a inverse line. Finally, the real upper gate signal g1 of phase a with shoot-through delay is generated by PM_a and m1 through an exclusive OR logic operation. The lower gate signal g4 is generated by PM_a inverse and m4 the same way.

Fig. 3.13 shows the experimental results of upper and lower gates signals for one leg. Fig. 3.13(a) is the sinusoidal pulse width modulation gate signal for both the upper and lower BJTs within the same leg. In order to see the shoot through delay clearly, the horizontal axis of Fig. 3.13(a) is amplified 10 times as shown in Fig. 13.3(b). Due to the finite switching time of the BJT's, the conducting BJT must be turned off before the other one in the same leg is turned on in order to guarantee that they do not both conduct simultaneously. Any violation of this minimum shoot through delay time constraint may result in an inverter shoot through fault that short circuits the dc link. As shown in Fig. 13.3(b), the upper BJT must be turned off 40μs early before the lower BJT is turned on. And the lower BJT also must be turned off 40μs early before the upper BJT is turned on.

Finally, the programmed three-phase sinusoidal pulse width modulation voltage is generated through the DS1102 DSP board, as shown in Fig. 3.14. There are three sinusoidal reference waves each shifted by 120°. The curves a, b and c represent the three reference sinusoidal voltages of phase a, phase b and phase c, respectively. V_a, V_b and V_c are the three phase PWM voltages. It is very clear that at any instant, the pulse width of the PWM voltage is proportional to the reference voltage amplitude.

The fundamental output voltage of the sinusoidal PWM inverter is varied by changing the value of the modulation index M. Figs. 3.15(a), (c) and (e) show the variations of the modulation index M at 0.8, 1.0 and 1.2 respectively. The corresponding

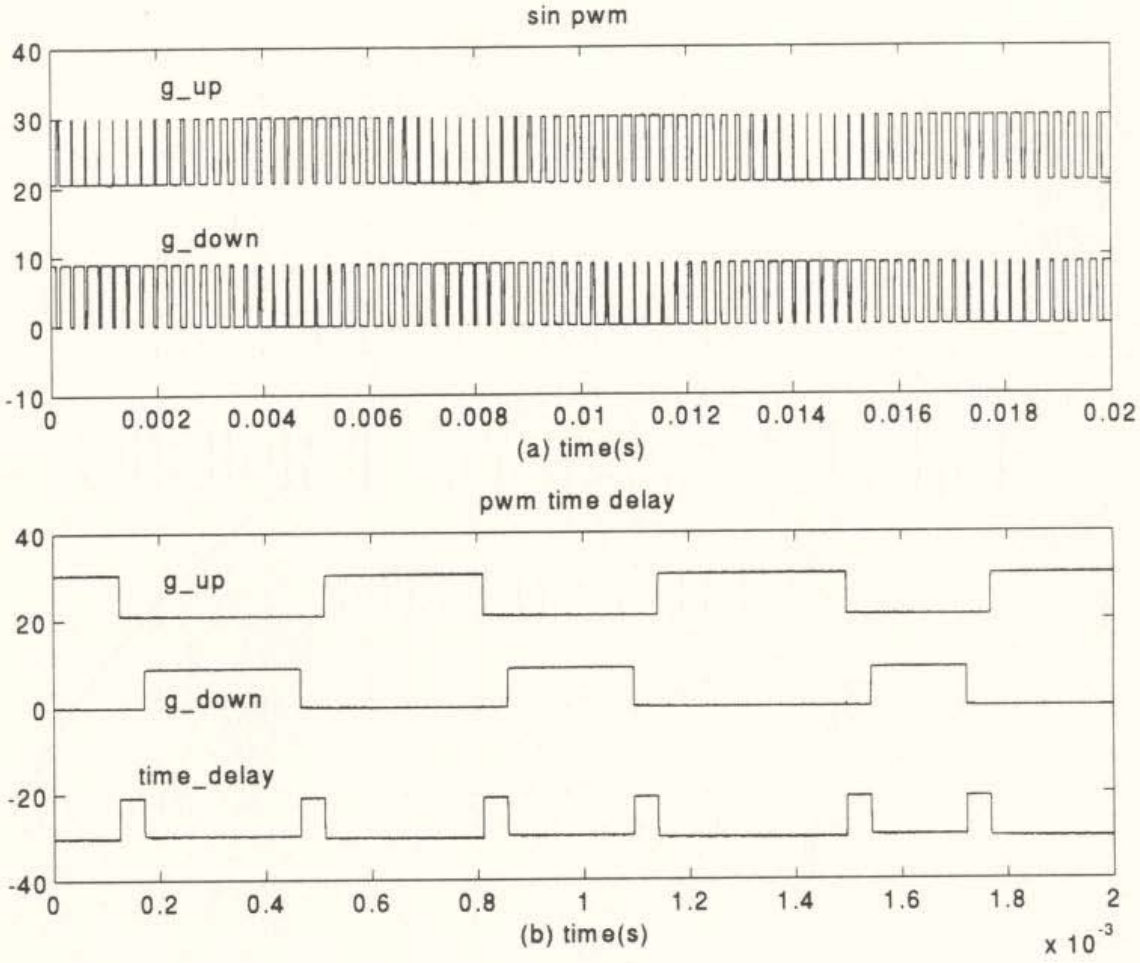

Fig. 3.13 Experimental gate signal and shoot through delay

(a) SPWM gate signals

(b) gate signals and shoot through delay

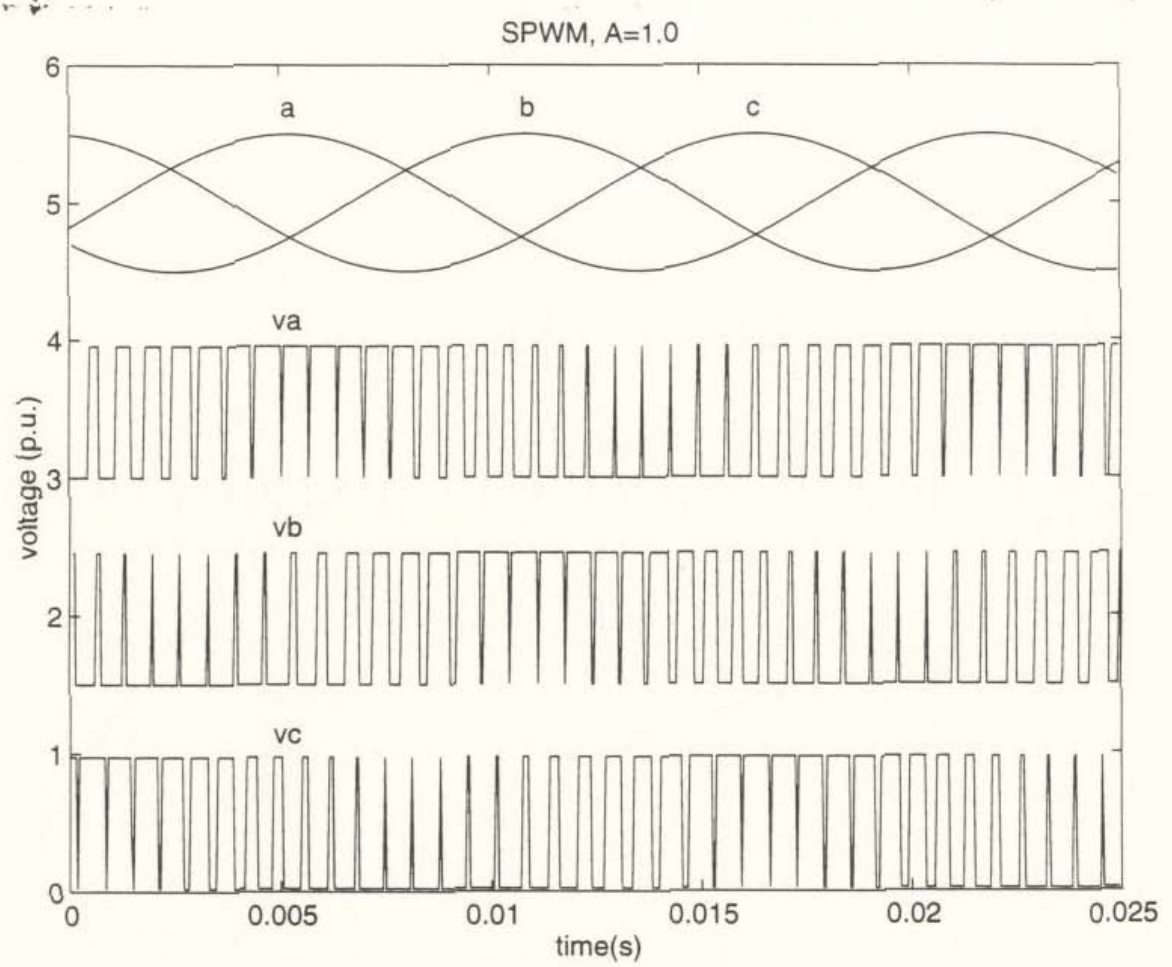

Fig. 3.14 Experimental three-phase SPWM waveform

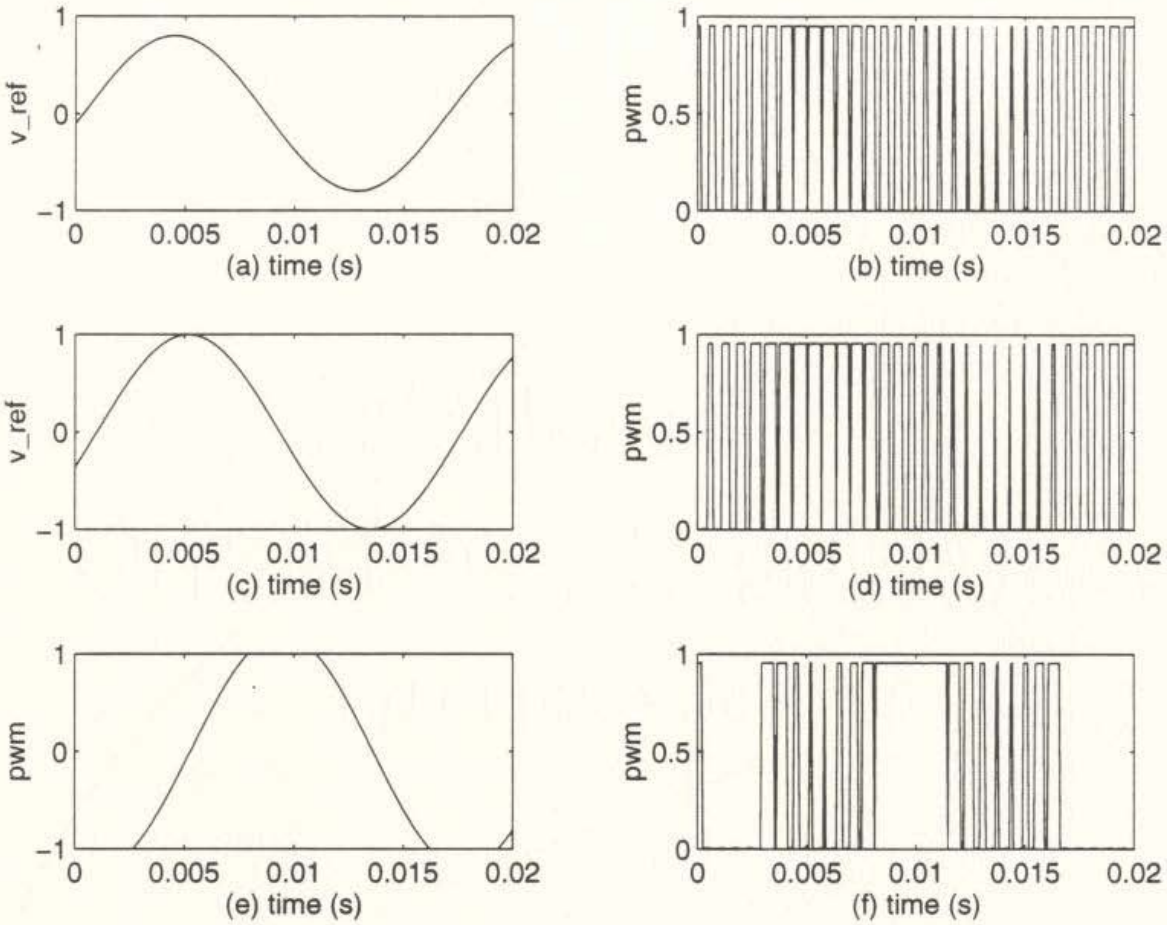

Fig. 3.15 Experimental results of the modulation variation

(a) modulation index M = 0.8 (b) SPWM output voltage for M = 0.8

(c) modulation index M = 1.0 (d) SPWM output voltage for M = 1.0

(e) modulation index M = 1.2 (f) SPWM output voltage for M = 1.2

sinusoidal PWM output voltages are shown in Figs. 3.15(b), (d) and (f), respectively. Improved utilization of the available dc link voltage is possible in a sine wave PWM inverter when M is increased above unity, as shown in Fig. 3.15(e) and (f), in which the modulation index M is 1.2. This increase in M overrides the normal sinusoidal modulation process and is termed over modulation. Some of the modulated pulses are lost, and as a result, pulses are dropped in the output voltage waveform. If the modulation index M is large enough, the voltage waveform will be an unmodulated square wave, and the inverter has changed from sine wave PWM to the six-step mode of operation, which develops the maximum possible value of fundamental voltage. The penalty for adopting over modulation is that the true sinusoidal modulation strategy is abandoned, and low-order harmonics reappear in the output voltage waveform.

3.6 Summary

This chapter began with an analysis of the sinusoidal pulse width modulation. For high enough carrier frequency, only the fundamental frequency component is significant. Its amplitude is linearly related to the width of the PWM pulses. The voltage utilization, adjustable frequency operation and harmonic analysis show that sinusoidal PWM voltage is suitable for the smooth operation of the PMHS motor.

Based on the analysis of three-phase voltage source inverter, the simplified operation logic relations of the inverter were described. The voltage space vectors were derived to lay the foundation for the DSP based PMHS motor control system.

Using a TMS320P14 DSP microcontroller, six channel PWM signals were

generated. The gate signals of the inverter with shoot through delay were achieved through logic operation. Finally, experimental results of the laboratory implemented programmed three-phase sinusoidal PWM voltage wave forms were given in different modulations.

Chapter 4

Direct and Quadrature Axis Current Controls in the PMHS Motor Drive

4.1 Introduction

The PMHS motor drive system is a multi-input multi-output control system. To control the current, electromagnetic torque, field flux and speed, a set of stator currents and their frequencies have to be controlled. The number of control variables become too many and each one of these has a direct influence on the field flux and electromagnetic torque. Independent control of the field flux and torque is required for high performance applications. That is made possible by a decoupling controller. This decoupling controller will transform the torque and field flux commands into equivalent current commands to influence these variables independently. This is similar to the dc motor control where field flux is controlled by the field current and torque by the armature current. Hence the decoupling controller transforms the control of the PMHS motor into that of an equivalent dc motor drive. This will enable the independent control of field flux and electromagnetic torque, thus simplifying the control task of the PMHS motor drive which is a multi-input multi-output system. A class of decoupling controllers, known as vector

controllers, will be used for this control system.

The current controllers determine the speed of response of the current loop and hence the torque generation in the motor. Apart from the speed of response of the current loop, it is desirable to minimize the current harmonics and hence the torque ripple.

4.2 Current and Voltage Transformation

The Park transformation will be used in order to model the PMHS motor in a manner similar to the separately excited dc motor. Further transformations that are necessary to account for the delta connection of the three phase stator windings are discussed. The fluxes, voltages, and currents in the three phase system are conveniently expressed as vectors in an orthogonal coordinate system. A transformation defined by the unitary matrix is given as

$$C_{abc} = \sqrt{\frac{2}{3}} \begin{bmatrix} \cos(0) & \cos(\frac{2\pi}{3}) & \cos(-\frac{2\pi}{3}) \\ \sin(0) & \sin(\frac{2\pi}{3}) & \sin(-\frac{2\pi}{3}) \\ \frac{1}{\sqrt{2}} & \frac{1}{\sqrt{2}} & \frac{1}{\sqrt{2}} \end{bmatrix} \qquad (4.1)$$

This matrix transforms the (a,b,c) system into the (α,β,0) coordinate system according to the following relation [37]

$$\begin{bmatrix} x_\alpha \\ x_\beta \\ x_0 \end{bmatrix} = C_{a\alpha} \begin{bmatrix} x_a \\ x_b \\ x_c \end{bmatrix} \tag{4.2}$$

Where x denotes the flux, voltage, or current. From a geometric viewpoint, the $C_{a\alpha}$ transformation maps the magnetic axis of the motor into the (α,β) plane formed by the two upper elements of the orthogonal system. The third dimension of the transformation, termed the zero (0) sequence quantity, cannot generate fluxes, voltages, or currents in the motor. As a result the simple case of the two-phase motor can be analyzed, together with the 0-axis quantities if required, and the results transformed to the three-phase equivalents if necessary.

It is interesting to note that $(C_{a\alpha})^t = (C_{a\alpha})^{-1}$, thus

$$(C_{a\alpha})^{-1} = (C_{a\alpha})^t = \sqrt{\frac{2}{3}} \begin{bmatrix} \cos(0) & \sin(0) & \frac{1}{\sqrt{2}} \\ \cos(\frac{2\pi}{3}) & \sin(\frac{2\pi}{3}) & \frac{1}{\sqrt{2}} \\ \cos(-\frac{2\pi}{3}) & \sin(-\frac{2\pi}{3}) & \frac{1}{\sqrt{2}} \end{bmatrix} \tag{4.3}$$

and

$$\begin{bmatrix} x_a \\ x_b \\ x_c \end{bmatrix} = (C_{\alpha a})^{-1} \begin{bmatrix} x_\alpha \\ x_\beta \\ x_0 \end{bmatrix} \tag{4.4}$$

By expressing the above equations in the rotor frame of reference, the explicit trigonometric dependencies can be removed. The coordinate axes in this frame are commonly aligned as direct and quadrature axes with respect to the rotor's magnetic

field. Since the zero-sequence quantities are not transformed, we are concerned only with the transformation from stator α, β axes to rotor d, q axes. The stator to rotor matrix depends on the actual rotor position. Therefore, the matrix elements are not constant and must be determined during every sampling cycle.

$$C_{\alpha d} = \begin{bmatrix} \cos\theta & \sin\theta \\ -\sin\theta & \cos\theta \end{bmatrix} \tag{4.5}$$

$$\begin{bmatrix} x_d \\ x_q \end{bmatrix} = C_{\alpha d} \begin{bmatrix} x_\alpha \\ x_\beta \end{bmatrix} \tag{4.6}$$

The output of the current controllers is a voltage space vector in rotor frame. This space vector must be retransformed to a space vector in stator coordinates, which requires the inverse matrix $(C_{\alpha d})^{-1}$.

$$\begin{bmatrix} x_\alpha \\ x_\beta \end{bmatrix} = (C_{\alpha d})^{-1} \begin{bmatrix} x_d \\ x_q \end{bmatrix} \tag{4.7}$$

with

$$(C_{\alpha d})^{-1} = \begin{bmatrix} \cos\theta & -\sin\theta \\ \sin\theta & \cos\theta \end{bmatrix} = (C_{\alpha d})^{t} \tag{4.8}$$

4.3 The Analysis of Stator Frame Current Controller

Most conventional analog current controllers operate in the stator frame by

controlling each line current separately. It is tempting to regulate rotor frame currents i_d and i_q with line current commands. In this case, the commands currents i_a^*, i_b^* and i_c^* are generated by inverse transforming i_d^* and i_q^*. The block diagram is shown in Fig. 4.1(a). It will be seen that this scheme introduces unwanted speed dependent coupling between i_d and i_q for the controller design. Most industrial analog control systems can be modeled in this form. It is this coupling and not the back emf that is largely responsible for their less than ideal observed performance [43].

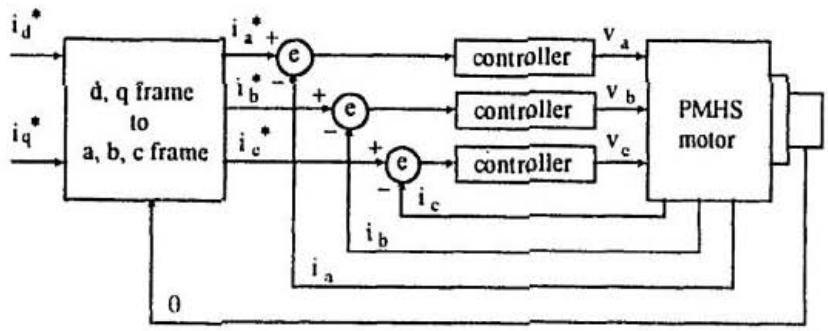

(a)

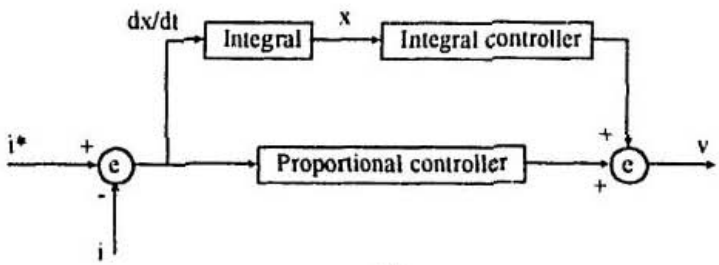

(b)

Fig. 4.1 Stator frame current controller

(a) block diagram of line current control (b) P-I line current controller

During steady state operation, stator frame current controllers are required to track sinusoidal commands whose frequency depends upon the motor speed. However, in the rotor frame, these commands are always constant. The sinusoidal currents seen by the motor are created by the d-q axis to line transformations and are not seen by the controller. It is well known that the proportional and integral (P-I) controller gives zero steady state error to constant command inputs [45]. Therefore, the P-I controller implemented directly in the rotor frame is expected to give performance that is superior to that of the P-I controller implemented in the stator frame. In the analysis below, they are compared to each other in the d-q frame by translating the stator frame (a,b,c) controller into its rotor (d,q) frame equivalent.

A detailed block diagram of one of the P-I line current controllers is given in Fig. 4.1(b). From Fig. 4.1(b) one can write following relations

$$\frac{dx}{dt} = i^* - i$$
$$x = \int (i^* - i)\, dt \qquad (4.9)$$

The stator frame equations for the system are

$$\begin{bmatrix} v_a \\ v_b \\ v_c \end{bmatrix} = K_p \begin{bmatrix} i_a^* - i_a \\ i_b^* - i_b \\ i_c^* - i_c \end{bmatrix} + \frac{1}{T_i} \begin{bmatrix} x_a \\ x_b \\ x_c \end{bmatrix} \tag{4.10}$$

$$\frac{d}{dt} \begin{bmatrix} x_a \\ x_b \\ x_c \end{bmatrix} = \begin{bmatrix} i_a^* - i_a \\ i_b^* - i_b \\ i_c^* - i_c \end{bmatrix} \tag{4.11}$$

where the states x are the integral of the feedback errors.

For a balanced three phase system, $x_a + x_b + x_c = 0$, only two quantities are independent. Thus, the third one can be determined from the other two known quantities. For simplifying analysis, phase a and phase b quantities are chosen to represent the a, b, c three phase system in this subsection. Thus the transfer matrix $C_{a\alpha}$ can be simplified as [44]

$$C_{a\alpha} = \begin{bmatrix} 1 & 0 \\ \frac{1}{\sqrt{3}} & \frac{2}{\sqrt{3}} \end{bmatrix} \tag{4.12}$$

The right hand side of the equation (4.11) is transformed into the d-q frame by inverting the $C_{a\alpha}$ transform and $C_{\alpha d}$ transform. Phase a and phase b are chosen to represent the three phases system. Therefore, this gives

$$\frac{d}{dt} \begin{bmatrix} x_a \\ x_b \end{bmatrix} = (C_{a\alpha})^{-1} (C_{\alpha d})^{-1} \begin{bmatrix} i_d^* - i_d \\ i_q^* - i_q \end{bmatrix} \tag{4.13}$$

In equation (4.13), the left hand side is stator frame (a,b) quantities and right hand side is rotor frame (d,q) quantities. To put both sides of the equation (4.13) in the same

frame, the derivation is as follows. First, notice that

$$\begin{bmatrix} x_d \\ x_q \end{bmatrix} = (C_{sd})(C_{as}) \begin{bmatrix} x_a \\ x_b \end{bmatrix} = \begin{bmatrix} \cos\theta & \sin\theta \\ -\sin\theta & \cos\theta \end{bmatrix} (C_{as}) \begin{bmatrix} x_a \\ x_b \end{bmatrix} \tag{4.14}$$

differentiating both side of equation (4.14) with respect to time gives

$$\frac{d}{dt}\begin{bmatrix} x_d \\ x_q \end{bmatrix} = -\frac{d\theta}{dt}\begin{bmatrix} \sin\theta & -\cos\theta \\ \cos\theta & \sin\theta \end{bmatrix}(C_{as})\begin{bmatrix} x_a \\ x_b \end{bmatrix} + (C_{sd})(C_{as})\frac{d}{dt}\begin{bmatrix} x_a \\ x_b \end{bmatrix} \tag{4.15}$$

$$= -\frac{d\theta}{dt}\begin{bmatrix} 0 & -1 \\ 1 & 0 \end{bmatrix}(C_{sd})(C_{as})\begin{bmatrix} x_a \\ x_b \end{bmatrix} + (C_{sd})(C_{as})\frac{d}{dt}\begin{bmatrix} x_a \\ x_b \end{bmatrix}$$

Detailed derivation is given in Appendix B. The right hand side first item of equation (4.15) is substituted by equation (4.14), and the right hand side second item of equation (4.15) is substituted by equation (4.13). This derivation yields equation (4.16)

$$\frac{d}{dt}\begin{bmatrix} x_d \\ x_q \end{bmatrix} = \begin{bmatrix} 0 & P\omega_r \\ -P\omega_r & 0 \end{bmatrix}\begin{bmatrix} x_d \\ x_q \end{bmatrix} + \begin{bmatrix} i_d^* - i_d \\ i_q^* - i_q \end{bmatrix} \tag{4.16}$$

Where P is the number of motor pole pairs and the ω_r is the rotor angular speed. Following an analogous procedure on the voltage Equation (4.10) gives

$$\begin{bmatrix} v_d \\ v_q \end{bmatrix} = K_p \begin{bmatrix} i_d^* - i_d \\ i_q^* - i_q \end{bmatrix} + \frac{1}{T_i}\begin{bmatrix} x_d \\ x_q \end{bmatrix} \tag{4.17}$$

From equations (4.16) and (4.17) one can obtain the specification of the stator frame line

current controller in the d-q frame. For the P-I current controller implemented directly in the d-q frame, the equations are

$$\frac{d}{dt}\begin{bmatrix} x_d \\ x_q \end{bmatrix} = \begin{bmatrix} i_d^* - i_d \\ i_q^* - i_q \end{bmatrix} \tag{4.18}$$

$$\begin{bmatrix} v_d \\ v_q \end{bmatrix} = K_p \begin{bmatrix} i_d^* - i_d \\ i_q^* - i_q \end{bmatrix} + \frac{1}{T_i}\begin{bmatrix} x_d \\ x_q \end{bmatrix} \tag{4.19}$$

The derivative and voltage equations derived from stator frame are given in equations (4.16) and (4.17), and the equations derived directly from the rotor frame are given in equations (4.18) and (4.19), respectively. It is clear that both of the voltage equations (4.17) and (4.19) are the same. The important difference between the two kinds of equations derived from different frames is in the integral state equations. The stator frame implementation results in speed dependent cross coupling between the d-q states. In steady state, $dx_d/dt = dx_q/dt = 0$. For the line current controller, the error between the commanded and the actual current is not zero but, instead, depends on the speed. On the other hand, the d-q frame P-I controller gives zero steady state error.

This result can also be explained by considering the form of i^* being fed into each controller. For the d-q controller, the reference currents i_d^* and i_q^* are constants. Thus, the P-I controller gives zero steady state error. For the stator frame implementation, the frequency of the sinusoidal commands i_a^*, i_b^* and i_c^* that are fed into each P-I controller depend on the motor speed. Since the loop gain of the P-I controller decreases with increasing frequency, higher speed operation gives a larger steady state error. In

terms of stator currents, this means that the sinusoidal currents in the motor have a gain and phase error that depend on speed. On the other hand, the P-I controller results in zero steady state error when implemented directly in the d-q frame. This is due to the fact that steady state motor currents appear as dc quantities in the d-q frame. Thus, the d-q controller is attractive because it gives zero steady state error with a simple P-I controller. Also, it is consistent with the philosophy of modelling and controlling as much of the system as possible in the d-q frame. The next several sections will detail the development of a d-q frame current controller for the PMHS motor.

4.4 Quadrature Axis Current Control

For the PMHS motor vector control system, the electrical dynamics are much faster than the mechanical dynamics so that the electrical state variables appear to have reached their equilibrium values when viewed by the slower mechanical states. On the other hand, the mechanical states seem essentially constant at their initial values when viewed by the electrical subsystem. Assuming that the electrical dynamics are uniformly stable and that all initial conditions are within the domain of attraction of the equilibrium point, the time required for the electrical states to reach their equilibrium values can be made arbitrarily small by choosing small enough input. This can be accomplished by increasing the speed of the electrical system via control action.

This gives formal justification for arranging the control system into the multiloop structure shown in Fig. 4.2. The inner control loop is used to regulate the electrical dynamics. The current controller is able to quickly force the motor currents to their

commanded values. Thus, under control action, the equilibrium currents are actually equal to the commanded values. The current commands now become the control inputs for the speed equation. Thus, the outer control loop regulates the speed of the motor by issuing current commands to the inner control loop. The inner current loop assures a fast current response and the limiter also maintains the current to a safe level. The outer speed loop ensures that the actual speed is always equal to the commanded speed and any transient will be overcomed within the shortest time without exceeding the motor and converter capabilities.

Static state linearization has been used to linearize and decouple the direct and quadrature axis current dynamics. This allows the development of each current controller separately. Valuable insight is gained by analyzing the block diagram of the system shown in Fig. 4.3. P(s) is the discrete time compensator to be implemented in the DSP board. D(s) is the PWM inverter transfer function. The sample and hold operations are modeled as Z(s), and the PMHS motor is modeled by M(s). The currents are sensed by Hall effect sensors with calibration K_H. The dynamics of the noise filter are represented by the continuous time transfer function F(s). From the block diagram, one can obtain the relationship

$$\frac{i_q(s)}{i_q^*(s)} = \frac{P(s)D(s)Z(s)M(s)}{1 + P(s)D(s)Z(s)M(s)K_H Z(s)F(s)} \qquad (4.20)$$

where i_q is the output current of the motor, i_{qf} is the filtered motor output current and the i^*_q is the current command. The transfer functions of the various subsystems will be described in the following subsections.

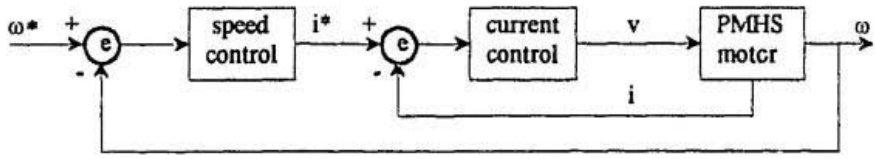

Fig. 4.2 Multi-loop control structure

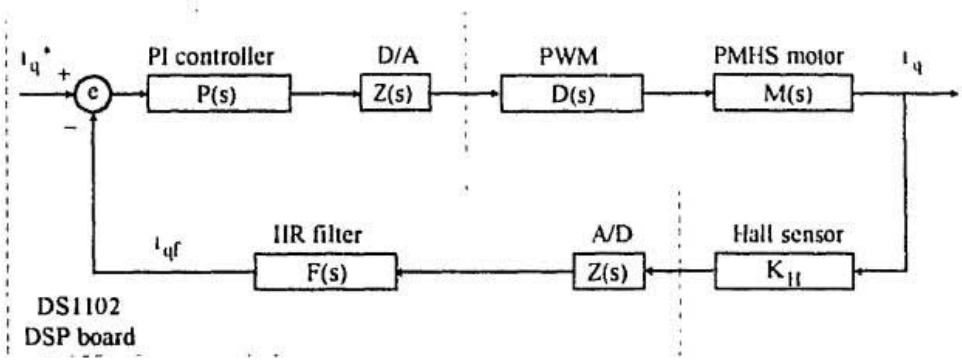

Fig. 4.3 Block diagram of current control

PI controller

. Since the controller is in the d-q frame, steady state current commands are constant. Even if it is desired to vary the motor speed, the slower response time of the mechanical system means that the current commands will vary relatively slowly and still appear constant over many samples of the inner loop sampling period. Thus, the control topology should give zero steady state error to constant command inputs. In addition, the controller should be robust to modelling errors. Finally, a simple algorithm is desirable. This minimizes the computational burden on the DSP board and allows a higher sampling rate for the inner control loop.

The proportional plus integral (PI) controller satisfies these constraints while giving acceptable dynamic performance. The transfer function of the PI controller is

$$P(s) = K_p + \frac{K_I}{s} = K_p\left(1 + \frac{1}{T_q s}\right) \qquad (4.21)$$

where K_P and K_I are the proportional and integral gain constants, respectively. The time constant is given as $T_q = K_p/K_I$. Clearly, the PI controller adds a zero at $s = -K_I/K_p$ and a pole at $s=0$ to the open loop transfer function. One obvious effect of the integral control is that it increases the order of the system by one. More important is that the type of the system is increased by one. Therefore, the steady state error of the original system without integral control is improved by one order; that is, if the steady state error to a given input is constant, the integral control reduces it to zero. However, because the system is increased by one order, it may be less stable than the original system or even become unstable if the parameters K_p and K_I are not properly chosen.

The state space model of a digital PI controller can be derived by sampling its continuous time counterpart. A block diagram of the resulting structure is shown in Fig. 4.4. The input e(k) is the error between the commanded and the measured currents while the output y(k) is the voltage command for the inverter, applied to the augmented sampled data model of the PMHS motor. The state space equations are

$$\begin{aligned} x(k+1) &= x(k) + T_s e(k) \\ y(k) &= K_I x(k) + K_p e(k) \end{aligned} \tag{4.22}$$

where x(k) is the integrator state, and T_s is the sampling time of DSP, and K_p and K_I are the proportional and integral gains, respectively.

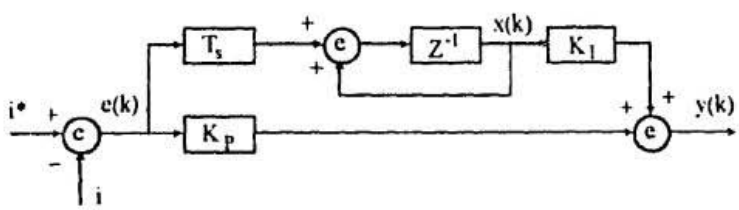

Fig. 4.4 Digital PI controller

PWM inverter

In this thesis, PWM signals are generated digitally using the DS1102 DSP board. The voltage source inverter used in this thesis requires the shoot through delay time of 40μs. It can be noted from the block diagram that the input of the PWM signal is the output of the PI controller, and the output of the PWM signal is the q axis stator voltage in the synchronously rotating reference frame. The inverter gain can be represented as a function of the peak voltage capability corresponding to the available control voltage. Hence its transfer function is given as

$$D(s) = \frac{K_{PWM}}{1 + sT_{PWM}} \qquad (4.23)$$

Zero-order hold

A digital to analog (D/A) converter is necessary to couple the digital PWM components to the analog interface circuit. The output of the digital PWM is a train of impulses. The data hold acts as an interface, or filter, that converts the impulses into an analog signal. One of the most commonly used data holds in practice is the zero-order hold (z.o.h.). Functionally, the z.o.h. simply holds the magnitude of the signal carried by the impulse at a given time instant, say, kT_s, for the entire sampling period T_s, until the next impulse arrives at $t = (k + 1)T_s$. Analytically, the z.o.h. is also used to model the operations of a A/D converter. The transfer function of the z.o.h. is given as

$$Z(s) = \frac{1 - e^{-sT}}{s} \tag{4.24}$$

There are many ways of approximating e^{-sT_s} by a rational function. A better approximation is to use the Padé approximation [45], which is given in the following for a two-term approximation:

$$e^{-sT_s} \approx \frac{1 - sT_s/2}{1 + sT_s/2} \tag{4.25}$$

The characteristic of the approximation is that the transfer function contains a zero in the right-half s-plane so that the step response of the approximating system may exhibit a small negative undershoot near $t=0$.

If the z.o.h. is connected in cascade with a linear process with transfer function $G_p(s)$, by using the time-delay property of z-transforms, the z-transform of the combination is written

$$G(z) = (1 - z^{-1}) Z\left[\frac{G_p(s)}{s}\right] \tag{4.26}$$

PMHS motor

On the basis of the analysis in Chapter 2, the PMHS motor currents and voltages in the rotor frame are represented as

$$\begin{aligned} v_d &= r_s i_d + \frac{d}{dt}(L_d i_d + \psi_m) - \omega_r L_q i_q \\ v_q &= r_s i_q + \frac{d}{dt}(L_q i_q) + \omega_r(\psi_m + L_d i_d) \end{aligned} \tag{4.27}$$

where ψ_m is the flux produced by the permanent magnet and residue hysteresis. In steady

state $d\psi_m/dt = 0$. For the convenience of analysis equation (4.27) is written in state variable form

$$\frac{d}{dt}\begin{bmatrix} i_d \\ i_q \end{bmatrix} = \begin{bmatrix} \frac{1}{L_d} & 0 \\ 0 & \frac{1}{L_q} \end{bmatrix}\begin{bmatrix} v_d \\ v_q \end{bmatrix} - \left(\begin{bmatrix} \frac{r_s}{L_d} & 0 \\ 0 & \frac{r_s}{L_q} \end{bmatrix} + \omega_r \begin{bmatrix} 0 & -\frac{L_q}{L_d} \\ \frac{L_d}{L_q} & 0 \end{bmatrix} \right)\begin{bmatrix} i_d \\ i_q \end{bmatrix} - \omega_r \psi_m \begin{bmatrix} 0 \\ \frac{1}{L_q} \end{bmatrix} \tag{4.28}$$

Currents i_d and i_q are taken as state variables. In order to design the controller, the state equations must not depend on speed. Examining equation (4.28), however, it is seen that ω_r is coupled to the electrical dynamics in two places. The first one is a nonlinear term proportional to $\omega_r i$ and the second one is due to the back emf $\omega_r \psi_m$. It is also desirable to linearize the state equation so that linear system theory can be applied to the design of the controller. For the electrical dynamics, the unwanted nonlinearity is created by the $\omega_r i$ and $\omega_r \psi_m$ terms. Using the continuous-time global linearization techniques [45], the control inputs can be used to cancel the unwanted dynamics and achieve the decoupling and linearization goals. For the electrical dynamics, define

$$\begin{bmatrix} v_d \\ v_q \end{bmatrix} = \begin{bmatrix} \frac{1}{L_d} & 0 \\ 0 & \frac{1}{L_q} \end{bmatrix}^{-1} \left(\begin{bmatrix} \frac{1}{L_d} & 0 \\ 0 & \frac{1}{L_q} \end{bmatrix}\begin{bmatrix} v_{dl} \\ v_{ql} \end{bmatrix} + \omega_r \begin{bmatrix} 0 & -\frac{L_q}{L_d} \\ \frac{L_d}{L_q} & 0 \end{bmatrix}\begin{bmatrix} i_d \\ i_q \end{bmatrix} + \omega_r \psi_m \begin{bmatrix} 0 \\ \frac{1}{L_q} \end{bmatrix} \right) \tag{4.29}$$

and substitute equation (4.29) into equation (4.28) to get

$$\frac{d}{dt}\begin{bmatrix} i_d \\ i_q \end{bmatrix} = \begin{bmatrix} \frac{1}{L_d} & 0 \\ 0 & \frac{1}{L_q} \end{bmatrix}\begin{bmatrix} v_{dl} \\ v_{ql} \end{bmatrix} - \begin{bmatrix} \frac{r_s}{L_d} & 0 \\ 0 & \frac{r_s}{L_q} \end{bmatrix}\begin{bmatrix} i_d \\ i_q \end{bmatrix} \tag{4.30}$$

The electrical dynamics are now totally decoupled and linear in terms of the new input v_f.

Take the continuous-time linear dynamics of i_q from equation (4.30) to get the continuous-time transfer function

$$M(s) = \frac{\frac{1}{r_s}}{1 + \frac{L_{ff}}{r_s} s} \qquad (4.31)$$

Hall Effect Sensor

The gain of the Hall effect current sensor is 85 and its time constant is so small that it can be reasonably neglected. Therefore, the transfer function of the Hall effect current sensor is

$$K_H = 85.0 \qquad (4.32)$$

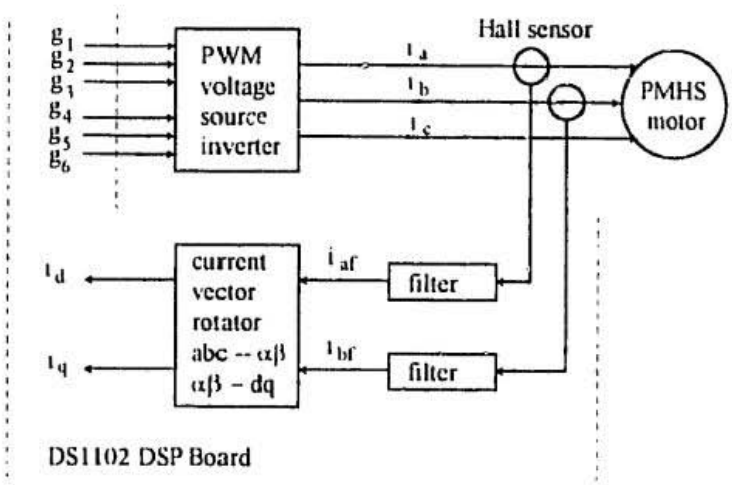

Fig. 4.5 Current sensing system

Noise Filter

In this proposed control system, there are two identical digital filter channels, each of which is placed on a line current, i_a and i_b. Upon transforming their dynamics into the d-q frame, it is seen that they introduce speed dependent coupling between i_d and i_q. The significance of the coupling is analyzed using the relative gain array and a state space model is developed.

A block diagram of the motor current sensing system is shown in Fig. 4.5. It is assumed that the dynamics of the Hall effect current sensors can be ignored. The line current signals are passed through noise filters. It is desired to model this entire process with an equivalent d-q frame filter whose inputs are i_d and i_q and whose outputs are the filtered signals i_{df} and i_{qf}.

The state space representation of the noise filters are

$$\frac{d}{dt}\begin{bmatrix} i_{af} \\ i_{bf} \end{bmatrix} = a\begin{bmatrix} i_{af} \\ i_{bf} \end{bmatrix} + b\begin{bmatrix} i_a \\ i_b \end{bmatrix} \qquad (4.33)$$

where a and b are parameters which correspond to a cutoff frequency. This system is transformed into the d-q frame in the same way that the stator currents are transformed into the d-q frame.

$$\begin{bmatrix} i_d \\ i_q \end{bmatrix} = C_{sd} C_{abc} \begin{bmatrix} i_a \\ i_b \end{bmatrix} \qquad (4.34)$$

Differentiation of equation (4.34) leads to the following equation

$$\frac{d}{dt}\begin{bmatrix} i_d \\ i_q \end{bmatrix} = -\frac{d\theta}{dt}\begin{bmatrix} \sin\theta & -\cos\theta \\ \cos\theta & \sin\theta \end{bmatrix} C_{abc}\begin{bmatrix} i_a \\ i_b \end{bmatrix} - C_{sd}C_{abc}\frac{d}{dt}\begin{bmatrix} i_a \\ i_b \end{bmatrix}$$

$$= -\frac{d\theta}{dt}\begin{bmatrix} 0 & -1 \\ 1 & 0 \end{bmatrix} C_{sd}C_{abc}\begin{bmatrix} i_a \\ i_b \end{bmatrix} - C_{sd}C_{abc}\frac{d}{dt}\begin{bmatrix} i_a \\ i_b \end{bmatrix} \qquad (4.35)$$

$$= \begin{bmatrix} 0 & P\omega_r \\ -P\omega_r & 0 \end{bmatrix} C_{sd}C_{abc}\begin{bmatrix} i_a \\ i_b \end{bmatrix} - C_{sd}C_{abc}\frac{d}{dt}\begin{bmatrix} i_a \\ i_b \end{bmatrix}$$

Multiplying both sides of the stator frame equation (4.33) by $C_{sd}C_{abc}$

$$C_{sd}C_{abc}\frac{d}{dt}\begin{bmatrix} i_{df} \\ i_{qf} \end{bmatrix} = a\,C_{sd}C_{abc}\begin{bmatrix} i_{df} \\ i_{qf} \end{bmatrix} + b\,C_{sd}C_{abc}\begin{bmatrix} i_a \\ i_b \end{bmatrix} \qquad (4.36)$$

$$= a\begin{bmatrix} i_{df} \\ i_{qf} \end{bmatrix} + b\begin{bmatrix} i_d \\ i_q \end{bmatrix}$$

and applying equations (4.34) and (4.35) yields the state space equations for the d-q frame where the speed dependent cross coupling is apparent.

$$\frac{d}{dt}\begin{bmatrix} i_{df} \\ i_{qf} \end{bmatrix} = \begin{bmatrix} a & P\omega_r \\ -P\omega_r & a \end{bmatrix}\begin{bmatrix} i_{df} \\ i_{qf} \end{bmatrix} + b\begin{bmatrix} i_d \\ i_q \end{bmatrix} \qquad (4.37)$$

The general coupled filter is described by its transfer function as

$$\begin{bmatrix} i_{df}(s) \\ i_{qf}(s) \end{bmatrix} = \begin{bmatrix} h_{11}(s,\omega) & h_{12}(s,\omega) \\ h_{21}(s,\omega) & h_{22}(s,\omega) \end{bmatrix}\begin{bmatrix} i_d(s) \\ i_q(s) \end{bmatrix} \qquad (4.38)$$

The closer that the diagonal elements are to one, the smaller the cross coupling. If the diagonal elements are near zero then there is strong coupling. For the proposed system, the magnitude of the diagonal elements is more than three orders of magnitude greater

than the off-diagonal elements. Thus, there is no significant coupling due to the noise filter. Therefore, the transfer function of the filter is

$$F(s) = \frac{b}{(s - a)} \tag{4.39}$$

Transfer Functions

Because the gain of Hall effect current sensor K_H is considered in the DSP control software, it will be equal to one in the transfer function. Also, because the sampling frequency of this system is as high as 6.25kHz, the zero-order hold effect is very small and can be reasonably neglected.

Thus the current control system open loop transfer function is given as

$$G_{io}(s) = \frac{bK_{pwm}K_p(T_i s + 1)}{L_q T_{pwm} T_i s^4 + T_i (r_s T_{pwm} + L_q - aL_q T_{pwm}) s^3 + T_i [r_s - a(r_s T_{pwm} + L_q)] s^2 - ar_s T_i s} \tag{4.40}$$

and the current control system closed loop transfer function is given as

$$G_{ic}(s) = \frac{k_{pwm}K_p [T_i s^2 + (1 - aT_i) s - a]}{L_q T_i T_{pwm} s^4 + T_i (r_s T_{pwm} + L_q - aL_q T_{pwm}) s^3 + T_i [r_s - a(r_s T_{pwm} + L_q)] s^2 + T_i (bK_{pwm}K_p - ar_s) s + bK_{pwm}K_p} \tag{4.41}$$

The Bode plot of a transfer function is a very useful graphical tool for any control system analysis and design. The Bode plot corresponds to the positive portion of the $j\omega$-axis from $\omega = \infty$ to $\omega = 0$ in the s-plane, so it is used to determine the gain and phase crossover points and the corresponding gain and phase margins. The determination of the

gain margin and the phase margin of a minimum-phase system from the Bode plot of $G(j\omega)H(j\omega)$ is as follows:

The gain margin G.M. is measured at the phase-crossover frequency ω_c:

$$G.M. = -|G(j\omega_c)H(j\omega_c)|\,dB \qquad (4.42)$$

The phase margin Pha.M. is measured at the gain-crossover frequency ω_g:

$$Pha.M. = -180^\circ + \angle G(j\omega_g)H(j\omega_g) \qquad (4.43)$$

The gain and phase margins are based on open-loop systems, and indicate the relative stability of the system when the loop is closed. The gain margin is the amount of gain increase required to make the loop gain unity at the frequency where the phase angle is -180°. Similarly, the phase margin is the difference between the phase angle of the response and -180° when the loop gain is 1.0. It is generally found that gain margins of three or more combined with phase margins between 30 and 60 degrees result in reasonable tradeoffs between the bandwidth and stability.

An effective design of PI controller is to place the zero at $s = -K_I/K_P$, very close to the origin in the s-plane, and the values of K_P and K_I should both be relatively small. To bring the magnitude curve of the uncompensated transfer function down to 0 dB at the new gain-crossover frequency ω'_c the PI controller must provide the amount of attenuation equal to the gain of the magnitude curve at the new gain-crossover frequency. In other words, set

$$|G_p(j\omega'_c)|\,dB = -20\log_{10}K_P\ dB \qquad (4.44)$$

from which

$$K_p = 10^{G(\omega_c')dB/20} \qquad (4.45)$$

Usually, as a general guideline, it is recommended that K_I/K_p be placed at a frequency that is at least one decade below ω_c'. Thus,

$$K_I = \frac{\omega_c'}{10} K_p \ rad/s \qquad (4.46)$$

The current controller parameters are selected in accordance with the symmetry criterion: $T_1 = 4T_{tot}$, $K_1 = (L_q/r_s)/(2K_mT_{tot})$, where T_{tot} is the sum of time constants of PWM inverter, z.o.h., Hall sensor and filter.

Fig. 4.6 is the Bode plot of the proposed current control system, PI controller, and the loop transmission as the frequency is varied up to 10^3 rad./sec. The parameters are given as follows: $K_{pwm}=1$, $T_{pwm}=0.000332$, $r_s=1.0$, $L_q=0.0290$, $a=-439.96$, $b=439.96$.

The location of the zero below that of the pole constitutes a phase lead compensator. As illustrated in the plots, it has the effect of increasing stability margins by slightly increasing the crossover frequency while simultaneously adding positive phase angle to the system. By maintaining a high band width, this type of compensation results in the rapid speed of response desired for the inner current loop. The location of the zero also results in overshoot to a step command. Since this transient dies out quickly, it does not have a great effect on the slower mechanical system and is thus tolerable.

Fig. 4.7 is the Bode plot of the closed loop transfer function. The system bandwidth rolls off rapidly at higher frequencies. Notice that extending the system bandwidth to suppress input disturbances has the accompanying effect of making the

system responsive to high frequency noise in the command input. It is thus desirable to make the bandwidth of the proposed system as small as can be tolerated for acceptable performance.

Now that the linear discrete-time PI controller has been specified, it must be combined with the static state linearization equations to form the complete control system. The calculation of the linear states is the same as in equation (4.22).

$$\begin{aligned} x_q(k+1) &= x_q(k) + T_s e_q(k) \\ v_{ql}(k+1) &= K_{qI} x(k) + K_{qP} e_q(k) \end{aligned} \qquad (4.47)$$

The linear voltage is then combined with speed and direct axis current measurement to determine the complete nonlinear output voltage as

$$v_q(k+1) = L_d \omega_r(k+1)\, i_d(k) + \psi_m \omega_r(k+1) + v_{qL}(k+1) \qquad (4.48)$$

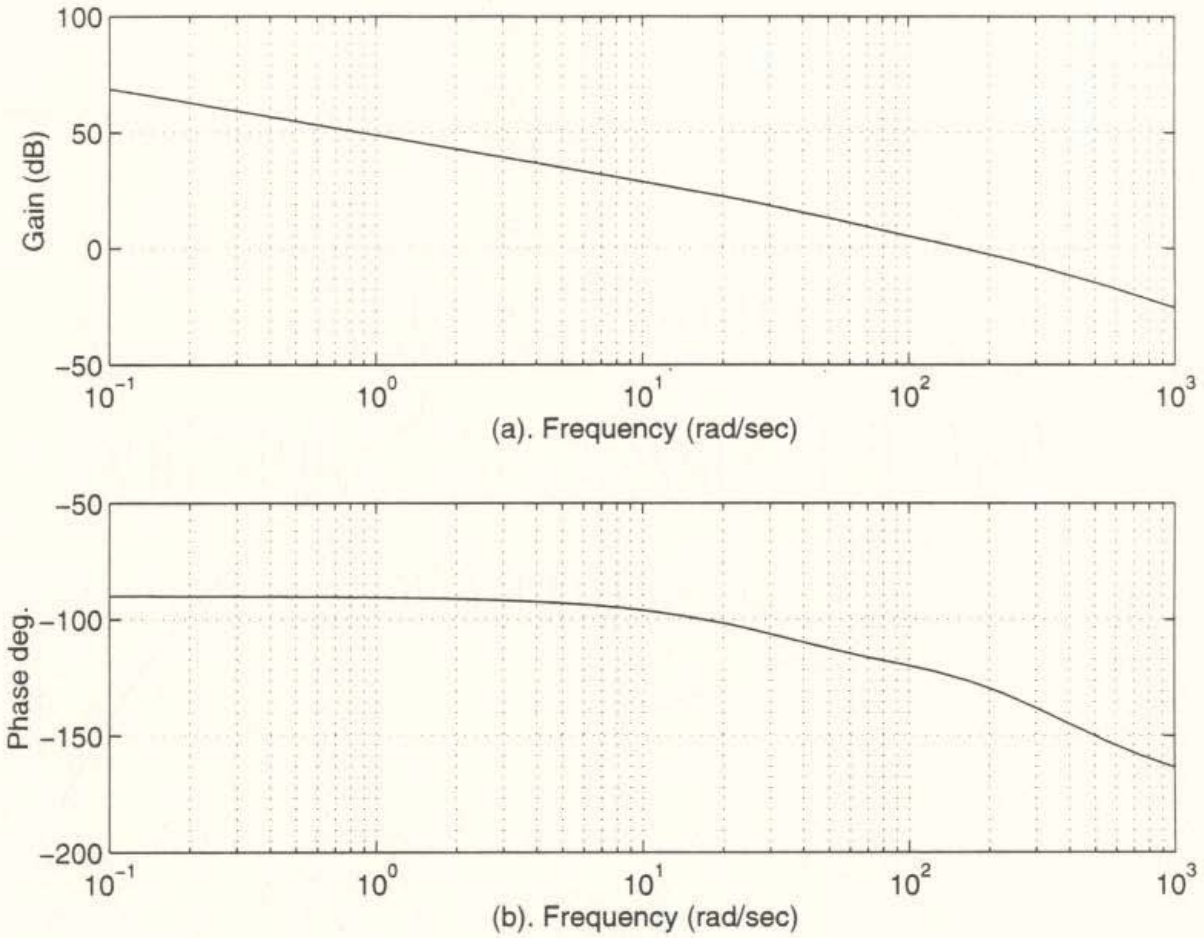

Fig. 4.6 Current open loop bode plot

(a) gain gargin

(b) phase margin

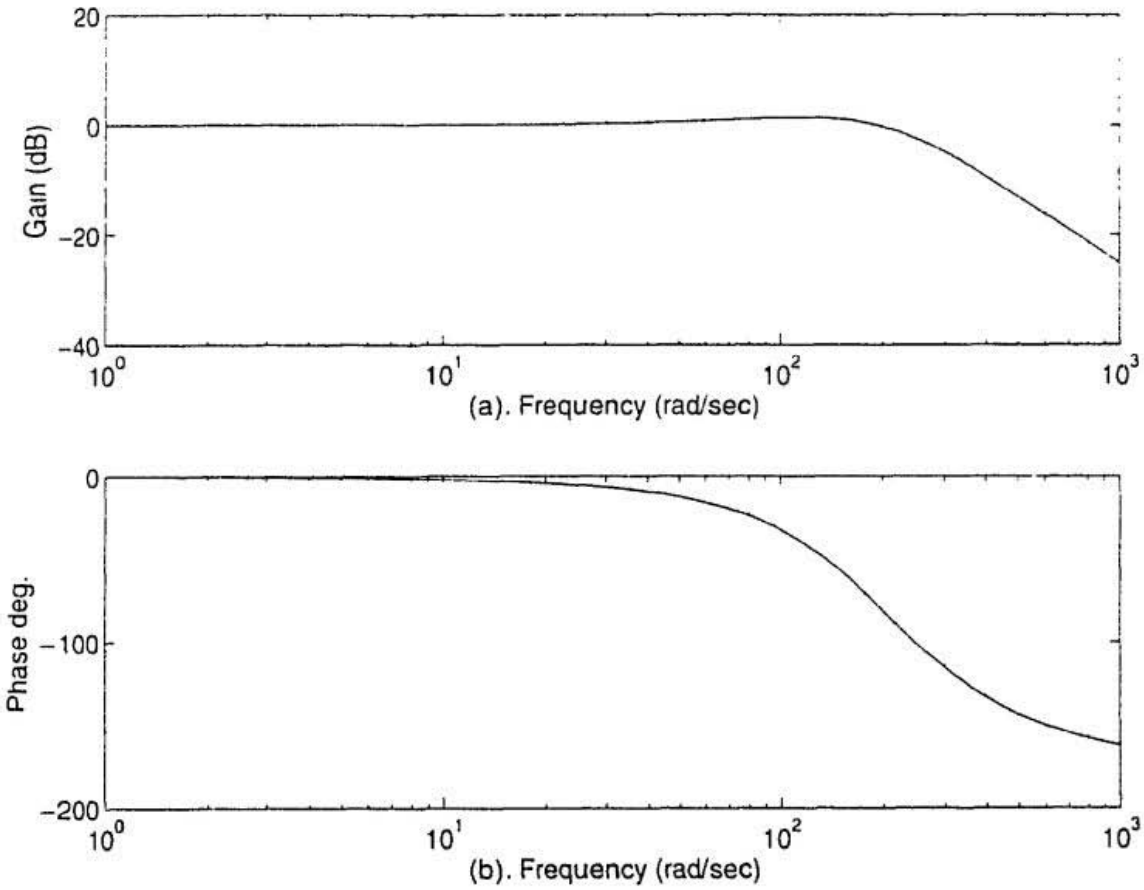

Fig. 4.7 Current closed loop bode plot

(a) gain margin

(b) phase margin

4.5 Direct Axis Current Control

Generally speaking, the ability to optimize the PMHS motor operations arises from the flexibility afforded by having two control inputs, one for i_d and the other for i_q. From the previous analysis, it is apparent that i_q is the primary source of the motor developed torque. More detailed torque analysis will be given in next chapter. A high value for i_q will result in a higher developed torque. The influence of i_d is more subtle. To see it more clearly, rewrite the i_q dynamic equation (4.27) as

$$v_q = r_s i_q + \frac{d}{dt}(L_q i_q) + \omega_r (\psi_m + L_d i_d) \qquad (4.49)$$

Assuming a limited power supply, there exists a maximum v_q that can be applied to the motor. For low speed operation, the back emf term $\omega_r \psi_m$ is easily overcome by v_q, thus allowing a larger value for i_q. However, as the speed increases, $\omega_r \psi_m$ eventually becomes large enough to cancel v_q with the result that no current can be drawn and thus no electrical torque. Notice that negative i_d can now be used in an effort to cancel ψ_m, thereby weakening the effective flux linkage due to the permanent magnet and hysteresis effects and allowing the motor to continue developing electrical torque over an extended range of speeds. This is termed as flux weakening operation. Of course, there is a tradeoff. The current capability of the inverter is also finite. Therefore, current applied to i_d reduces the available current for i_q. This fact, along with the coupling in the i_d dynamic equation makes the choice of optimum i_d and i_q difficult to determine. In addition, the specific voltage and current limitations of the inverter will influence the

tradeoff.

More specifically, a similar argument illustrates that the inverter voltage can be the limiting factor in achieving the desired level of i_d and i_q. In order to develop a large electric torque, a large i_q is needed. From equation (4.49) this requires a large v_q and a large negative i_d. From equation (4.27), a large negative i_d is attained with a large negative v_d. By expressing the inverter voltage limitation as

$$V^2 = v_d^2 + v_q^2 \qquad (4.50)$$

where V is the maximum inverter voltage, it is seen that a large v_q and a large negative v_d cannot be delivered simultaneously. Thus, when choosing the optimum i_d and i_q, the inverter voltage limitation must be considered as well as the inverter current limitation. In this thesis, the control algorithm is designed to keep i_d at zero and vary i_q to adjust the electromagnetic torque.

The model of the direct axis current channel differs from that of the quadrature axis current channel in that $L_d \neq L_q$. The two inductances are, however, close enough in value that the same PI controller will suffice for both the quadrature and the direct axis current dynamics. Therefore, the detailed development of the direct axis current controller, being essentially the same as that for the quadrature axis current controller, will not be repeated here.

Based on the quantities measured at time k and those saved from the previous sampling period, the discrete-time linear states are calculated from

$$x_d(k+1) = x_d(k) + T_s e_d(k)$$
$$x_{dL}(k+1) = K_{dI} x_d(k) + K_{dP} e_d(k) \qquad (4.51)$$

The linear voltage is then combined with measured speed and the quadrature axis current measurement to determine the complete nonlinear voltage

$$v_d(k+1) = -\omega_r(k+1) L_q i_q(k) + v_{dL}(k+1) \qquad (4.52)$$

4.6 Digital Filter Design and Application

A block diagram of the PMHS motor current sensing system is shown in Fig. 4.5. It is assumed that the dynamics of the Hall effect current sensors can be ignored. In practice, some unwanted noise exists in the sensed line currents i_a and i_b. Thus, two digital filters are used to filter the noise before the line currents i_a and i_b are transformed into rotor frame currents i_d and i_q.

Digital filters are broadly divided into two classes, namely infinite impulse response (IIR) and finite impulse response (FIR) filters. The input and output signals to the filter are related by the convolution sum, which is given in Equations (4.53) for the IIR and in (4.54) for the FIR filter.

$$y(n) = \sum_{k=0}^{\infty} h(k) x(n-k) \qquad (4.53)$$

$$y(n) = \sum_{k=0}^{N-1} h(k) x(n-k) \qquad (4.54)$$

where x(n) is the input sequence, h(k), k=0,1,... is the impulse response and y(n) is the

output sequence. It is evident from these equations that, for IIR filters, the impulse response is of infinite duration whereas for FIR it is of finite duration, since h(k) for the FIR has only N values. In practice, it is not feasible to compute the output of the IIR filter using equation (4.53) because the length of its impulse response is too long (infinite in theory). Instead, the IIR filtering equation is expressed in a recursive form:

$$y(n) = \sum_{k=0}^{\infty} h(k)\,x(n-k) = \sum_{k=0}^{N} a_k x(n-k) - \sum_{k=1}^{M} b_k y(n-k) \qquad (4.55)$$

where the a_k and b_k are the coefficients of the filter. We note that, in Equation (4.55), the current output sample y(n) is a function of past outputs as well as present and past input samples, that is the IIR is a feedback system of some sort. This should be compared with the FIR equation in which the current output sample y(n) is a function only of past and present values of the input.

Alternative representations for the FIR and IIR filters are given in Equations (4.56) and (4.57), respectively. These are the transfer functions for these filters and are very useful in evaluating their frequency responses.

$$H(z) = \sum_{k=0}^{N-1} h(k)\,z^{-1} \qquad (4.56)$$

$$H(z) = \frac{\sum_{k=0}^{N} a_k z^{-k}}{\left[1 + \sum_{k=1}^{M} b_k z^{-k}\right]} \qquad (4.57)$$

The choice between FIR and IIR filters depends largely on the relative advantages of the two filter types. FIR filter requires more coefficients for sharp cutoff filters than

IIR filter. Thus for a given amplitude response specification, more processing time and storage will be required for FIR implementation. FIR filter can have an exactly linear phase response. The implication of this is that no phase distortion is introduced into the signal by the filter. In this thesis, because the generation of six channel digital PWM signals takes DSP about 80 μs already, the processing time of filter is mainly concerned. Thus the first order IIR filter is chosen.

A Butterworth filter is designed for this thesis to have a maximally flat amplitude response in the passband. The edge of the passband is usually defined to be the frequency where the amplitude response is 0.707 times the maximum value. The amplitude response of a Butterworth filter decreases monotonically in the transition band and in the stop band. The lowpass Butterworth filter is characterized by the following magnitude frequency response

$$|H(\omega)| = \left[1 + \left(\frac{\omega}{\omega_p}\right)^{2N}\right]^{-\frac{1}{2}} \qquad (4.58)$$

where N is the order of the filter and ω_p is the 3 dB cutoff frequency.

An important class of IIR digital filter design is based on converting a classic analog Butterworth filter to its digital equivalent. The function in the "Signal Processing Toolbox [47]" for designing the lowpass version of this filter is

```
[a,b] = butter(N,Wn)
```
(4.59)

This function designs an N order lowpass filter with cutoff frequency Wn, where Wn is a number between 0 and 1, with 1.0 corresponding to half the sample frequency according to the Nyquist criterion. This function returns the filter coefficients in length

N+1 row vectors a and b. The filter coefficients are ordered in descending powers of z:

$$H(z) = \frac{a(1) + a(2)z^{-1} + \ldots + a(n+1)z^{-n}}{1 + b(2)z^{-1} + \ldots + b(n+1)z^{-n}} \qquad (4.60)$$

In this thesis, the sampling frequency f_s = 6250 Hz, and the maximum line frequency is 60 Hz. Thus

$$Wn = \frac{2f_c}{f_s} = \frac{2\times 70}{6250} = 0.0224 \qquad (4.61)$$

Finally, the first order IIR Butterworth digital filter in the time domain is characterized by the difference equation

$$y(n) = 0.034(n) + 0.034x(n-1) + 0.932y(n-1) \qquad (4.62)$$

The block diagram representation of the filter is given in Fig. 4.8. Fig. 4.9 is the comparison of the experimental PMHS motor line currents before and after being filtered. Figs. 4.9 (a), (c) and (e) show the line currents before being filtered at frequency of 12 Hz, 36 Hz and 60 Hz, respectively. Figs. 4.9 (b), (d) and (f) show the line currents after being filtered. It shows that the designed filter is very effective to remove the high frequency noise contained in line currents.

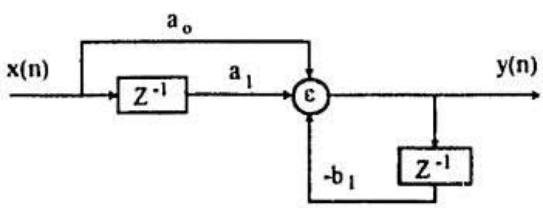

Fig. 4.8 Block diagram of first order IIR filter

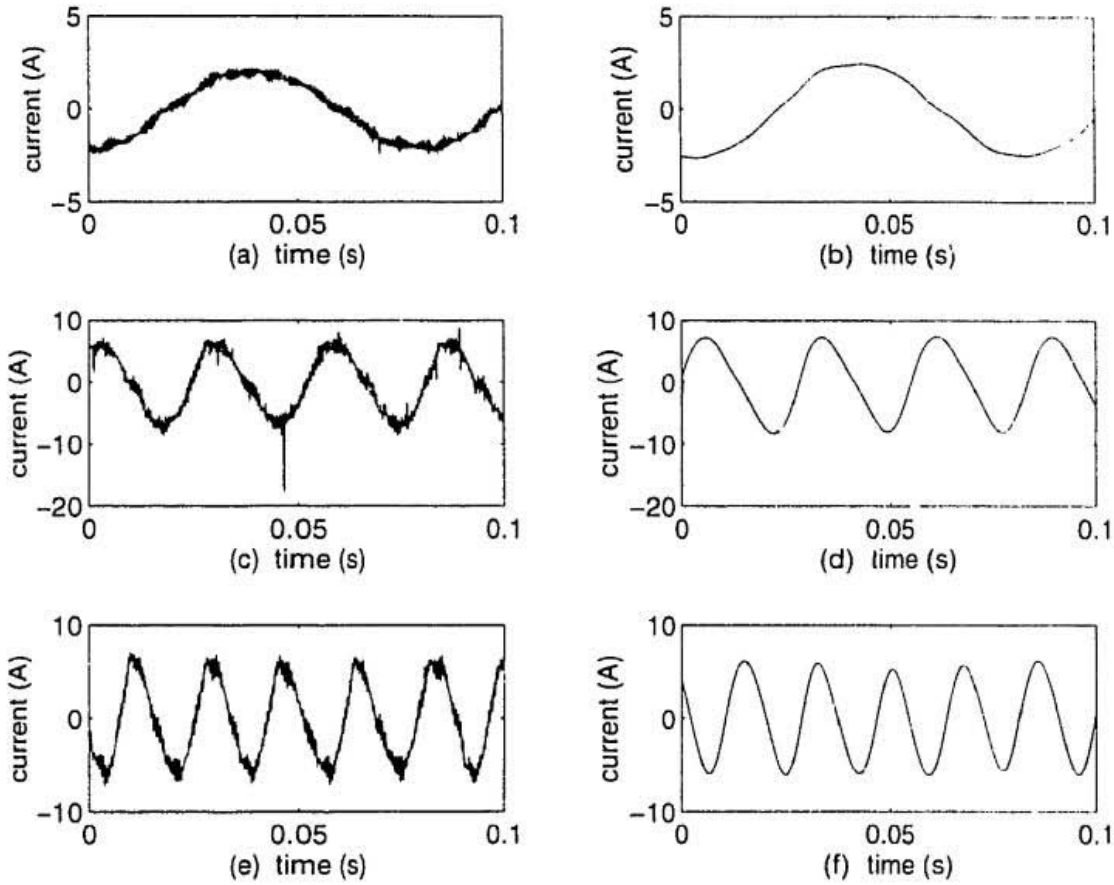

Fig. 4.9 Experimental currents before and after being filtered

(a) current at 12 Hz before being filtered (b) current at 12 Hz after being filtered

(c) current at 36 Hz before being filtered (d) current at 36 Hz after being filtered

(e) current at 60 Hz before being filtered (f) current at 60 Hz after being filtered

4.7 Current Control Implementation and Experimental Results

The necessary parts to construct the inner loop current controller have been developed. Fig. 4.10 shows the functional block diagram of the current control loop.

The direct and quadrature axis current commands are compared against the measured currents to generate the error signals e_d and e_q. The errors are fed into compensator algorithm that is composed of the d and q axis PI controller and emf due to the cross axis flux. Its outputs are the voltages v_d and v_q. The transformation from d-q axis voltages to line quantities is taken first. The output voltages from the controller, v_d and v_q must ultimately be applied to the motor as the line voltages v_a, v_b and v_c. The first step is to translate the rotor frame voltages v_d and v_q to stator frame voltages v_α and v_β, and then transferred to the reference line voltage quantities v_a^*, v_b^* and v_c^*. Since the digital PWM is used to actually generate the line voltages, the quantities used here are the PWM commands rather than the voltages themselves. The PWM command simply specifies the voltage pulse width over one PWM sampling period that is needed to apply the desired voltage, on average, to the motor stator terminals. Finally, the PWM voltage source inverter gate signals are generated by the digital PWM system. As described in Section 3.4, the digital PWM system for each channel generates a centred voltage pulse by correctly programming the two action registers. The PWM signals are sent to shoot through delay circuits, then to amplifiers. Finally, the line voltages v_a, v_b and v_c are generated by the voltage source inverter.

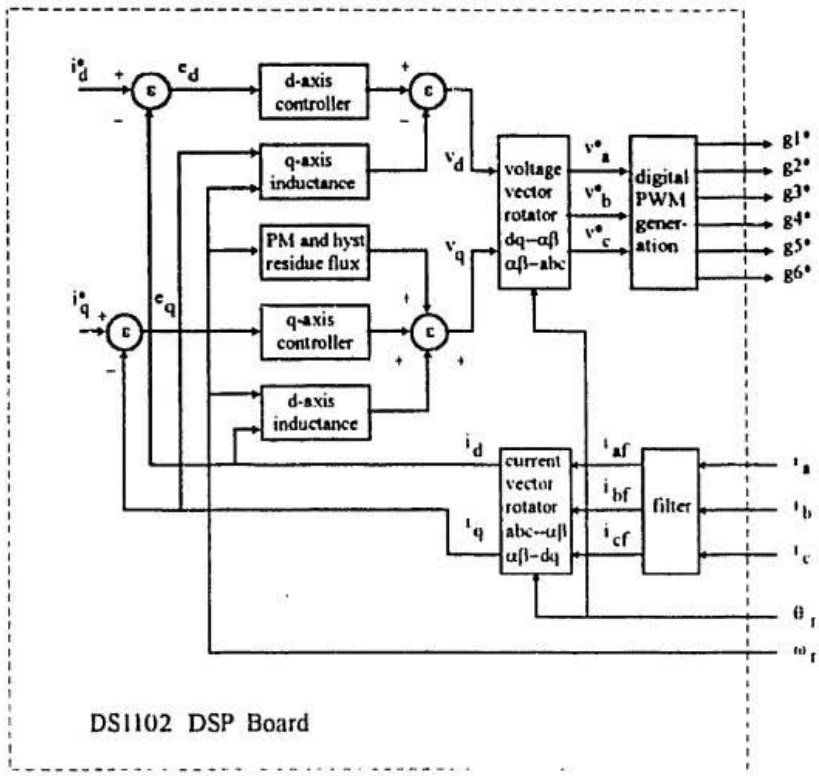

Fig. 4.10 Current control function overview

The line currents are measured by Hall effect sensors and then filtered by low pass IIR digital filter. The outputs of the filter i_{af}, i_{bf} and i_{cf} are transformed into the d-q axis currents i_d and i_q by the current vector rotator. In a separately excited dc motor, the armature current and the field current are orthogonal to each other. This gives the best dynamic performance of a dc motor because the armature current is decoupled from the field current. In the vector control of ac motors, the reference frame d-q is fixed in the rotor frame, thus the control variables can be treated as constants in the d-q frame, and the currents i_d and i_q appear as dc quantities in the steady state condition. In the PMHS motor, the dominant airgap flux is produced by the permanent magnets and the hysteresis material in the rotor. The permanent magnets and hysteresis material will provide enough flux so that the magnetizing stator current can be zero in the PMHS motor vector control. As discussed in Section 4.5, i_d is commanded to zero also, because flux weakening control is not needed over the range of mechanical operation in this thesis. With $i_d = 0$, the quadrature current i_q adjusts the motor torque. Therefore, the motor performance is just like a separately excited dc motor. If the motor field control is required, the current i_d can be positive for aiding the airgap flux along the d-axis. It can also be negative for demagnetising the airgap flux, resulting in a decrease of the total flux.

The rotor position θ_r and speed ω_r signals are generated by the digital incremental encoder. The rotor position θ_r is required for the current and voltage vector rotators, and the rotor speed ω_r is required to calculate emf generated by cross flux in the d-q axes, respectively.

This is a completely digital control system. All of the calculations such as d-q axis controllers, voltage and current frame transformations, digital PWM signal generation and low pass IIR digital filter are completed by the DS1102 DSP board.

Fig. 4.11 shows the experimental currents having the frequency of f=12 Hz, f=36 Hz and f=60 Hz. Fig. 4.11(a) shows the PMHS motor line current i_a at 12 Hz. The motor line currents are measured by Hall effect sensors, then fed into the DSP board through an A/D interface. After filtering, the three phase line currents are first transformed into the two phase α-β stator frame, and then transformed into the d-q rotor frame. Figs. 4.11 (b) and (c) show the rotor frame d-q axis currents i_d and i_q at 12 Hz. Similarly, Figs. 4.11 (d), (e) and (f) show the line current i_a, rotor frame current i_d and i_q at 36 Hz, respectively. Figs. 4.11 (g), (h) and (i) show the line current i_a and rotor frame d-q axis currents i_d and i_q at 60 Hz, respectively. It is to be noted that the currents i_d and i_q appear as dc quantities in the steady state condition, and the direct axis current i_d is ideally controlled to zero.

4.8 Summary

A fully digital current control system for the PMHS motor has been developed in this chapter. The electrical dynamics are regulated through the independent control of the direct and quadrature axis currents.

First, the fluxes, voltages, and currents in the three phase system are conveniently expressed as vectors in an orthogonal coordinate system. The output of the current controllers is a voltage space vector in the rotor frame. This space vector has been retransformed to a space vector in stator coordinates.

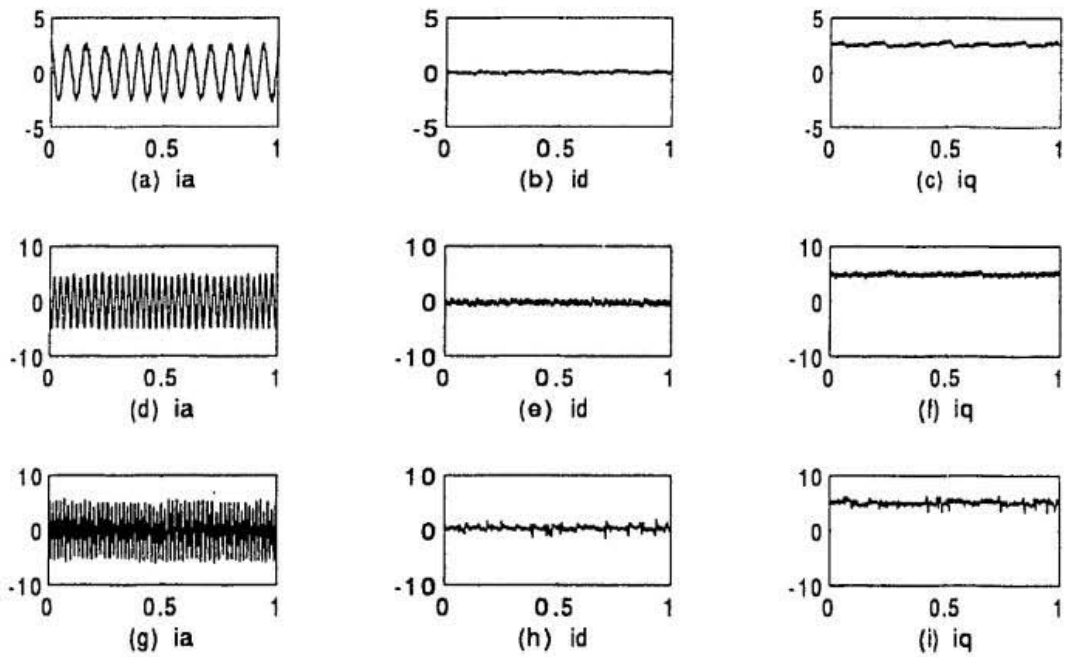

Fig. 4.11 Experimental line and rotor frame currents

(a) current i_a at 12 Hz; (b) current i_d at 12 Hz; (c) current i_q at 12 Hz

(d) current i_a at 36 Hz; (e) current i_d at 36 Hz; (f) current i_q at 36 Hz

(g) current i_a at 60 Hz; (h) current i_d at 60 Hz; (i) current i_q at 60 Hz

It was shown that the conventional stator frame line current controller can be transformed into a set of d-q current commands. However, the PI line current controllers are unable to directly regulate the d-q axis currents without introducing speed dependent coupling between i_d and i_q. In addition, the PI line current controllers do not give zero steady state error since the steady state current commands in the stator frame are sinusoid rather than constants. Without further compensation, the direct application of the PI stator frame current controller for the purpose of regulating d-q currents is not satisfactory. Instead, a rotor frame PI current controller was developed. Because it sees constant commands, it gives zero steady state error.

Using the frequency domain approach, the quadrature axis current controller was developed. The sampled data system was modeled. Based on the current and speed loop transfer functions, the Bode plot designs were given. The developed control algorithms have then been put into a form that could be implemented directly on the real-time digital system.

The advantages and disadvantages of both FIR and IIR digital filters were discussed. Because the processing time of filters is the main concern, the first order IIR filter was chosen.

Finally, the performance of the controller was examined. An experimental verification of the algorithm was carried out by measuring the stator line current at different frequencies. The line currents were transferred into d-q axis to get the constant control variables in steady state, and the direct axis current i_d is ideally controlled to zero. This makes the inner control loop operational.

Chapter 5

Torque and Speed Control of the PMHS Motor

5.1 Introduction

The objective of this chapter is to derive the PMHS motor torque equation and design the digital speed controller for the vector control system. The torque control that regulates the speed of the PMHS motor, is provided by a quadrature axis current command developed by the speed controller. The digital speed controller design is carried out by the symmetry optimum condition based on the speed loop transfer function.

Determination of the PMHS motor torque is much more complicated than that for the conventional induction or synchronous motor because of the nonlinear hysteresis and eddy current properties. Based on the model presented in Chapter 2, the torque equation is derived and analyzed for the control purpose. The non-linear equations of the rotor hysteresis and eddy currents which are difficult to access by means of outside

control are also derived.

The proportional plus integral (PI) controller is normally employed to limit the error between the commanded and actual values of the rotor speed. The design of the gain and time constants of the speed controller is of critical importance in meeting the specifications for dynamic performance of the PMHS motor. Using the Bode plot method, the speed controller is designed around the nominal parameter values. Performance goals are specified in terms of rise time, overshoot, and steady state error. It is also important that the closed loop pole locations can be used to specify the dynamic response of the drive system.

Finally, the experimental verification obtained by using the DSP based vector control is presented.

5.2 PMHS motor torque equation

The general expression of the developed torque in the 3-phase 2P-pole ac motor is given as:

$$T_e = \frac{3}{2} P (\psi_{ds} i_{qs} - \psi_{qs} i_{ds}) \qquad (5.1)$$

If the stator and rotor leakage inductances L_{ls} and L_{lr} are neglected, the flux equation for the permanent magnet hysteresis synchronous motor may be written as:

$$\psi_{ds} = L_{dm} (i_{ds} + i_{dh} + i_{de} + i_{pm}) \qquad (5.2)$$

$$\psi_{qs} = L_{qm} (i_{qs} + i_{qh} + i_{qe}) \qquad (5.3)$$

where i_{dh} and i_{de} are the d-axis rotor hysteresis current and eddy current respectively, i_{qh}

and i_{qe} are the q-axis rotor hysteresis current and eddy current respectively and i_{pm} is the equivalent permanent magnet source current in the d-axis. Substituting the flux linkage ψ_{ds} and ψ_{qs} of equations (5.2) and (5.3) into equation (5.1) the electromagnetic developed torque T_e of the PMHS motor is given as

$$T_e = \frac{3}{2} P\left[(L_{dm} - L_{qm})\, i_{ds}\, i_{qs} + L_{dm} (i_{dh} + i_{de} - i_{pm})\, i_{qs} - L_{qm} (i_{qh} + i_{qe})\, i_{ds} \right] \tag{5.4}$$

The first term of the developed torque equation (5.4) is the reluctance torque component which is the product of the d, q axis stator currents i_{ds} and i_{qs}, as well as the difference of the d and q axis mutual inductance L_{dm} and L_{qm}. For the PMHS motor, the difference of these two inductances is small, so this reluctance torque component is not significant. The second term of equation (5.4) is the rotor d axis flux interacting with the stator q axis current i_{qs}. The rotor d axis flux is generated by the rotor d axis hysteresis current i_{dh}, the rotor d axis eddy current i_{de} and the rotor d axis equivalent permanent magnet source current i_{pm}. This is the main part of the developed torque of a PMHS motor. The last term of the torque equation (5.4) is a negative component which is related to the flux weakening mode of operation. It is the q axis rotor flux which is generated by the q axis hysteresis current i_{qh} and eddy current i_{qe} reacting with the d axis stator current i_{ds}.

It can be seen from the above analysis that the prediction of the developed torque of the PMHS motor is quite complicated for the following two reasons. Firstly, the developed torque varies with the amplitude of the stator currents i_{ds} and i_{qs}. Secondly, the variables in the rotor are not easily accessible by means of outside control. The calculation of the rotor currents is complicated due to the nonlinear hysteresis and eddy

current effects.

The derivation of the stator current, rotor hysteresis current, eddy current and the equivalent permanent magnet source current can be given as follows.

The measured stator frame line currents i_{as} and i_{bs} can be transformed into rotor d-q axis current by using the transfer matrix C_{as} and C_{sd}, which are given by

$$\begin{bmatrix} i_{ds} \\ i_{qs} \end{bmatrix} = [C_{sd}][C_{abs}] \begin{bmatrix} i_{as} \\ i_{bs} \end{bmatrix} \tag{5.5}$$

The d-q axis voltage equations for an ac motor are

$$\begin{aligned} v_{ds} &= r_s i_{ds} + \frac{d}{dt}\psi_{ds} - \omega_r \psi_{qs} \\ v_{qs} &= r_s i_{qs} + \frac{d}{dt}\psi_{qs} + \omega_r \psi_{ds} \end{aligned} \tag{5.6}$$

Substituting the flux linkage ψ_{ds} and ψ_{qs} of equations (5.2) and (5.3) into equation (5.6), the PMHS motor voltage equations become

$$\begin{aligned} v_{ds} &= r_s i_{ds} + L_{dm} \frac{d}{dt}(i_{ds} + i_{dh} + i_{de} + i_{pm}) - \omega_r L_{qm}(i_{qs} + i_{qh} + i_{qe}) \\ v_{qs} &= r_s i_{qs} + L_{qm} \frac{d}{dt}(i_{qs} + i_{qh} + i_{qe}) + \omega_r L_{dm}(i_{ds} + i_{dh} + i_{de} + i_{pm}) \end{aligned} \tag{5.7}$$

Referring to the PMHS motor equivalent circuit which is given is Fig. 2.6, and transferring the voltage equation from time domain to frequency domain, the d-axis voltage equations in phasor form are obtained as

$$\begin{aligned} V_{ds} &= r_s I_{ds} + j\omega_r L_{md}(I_{ds} + I_{dh} + I_{de} + I_{pm}) - j\omega_r L_{mq}(I_{qs} + I_{qh} + I_{qe}) \\ 0 &= (sR_{dh} + j\omega_r L_{md}) I_{dh} + j\omega_r L_{md}(I_{de} + I_{pm} + I_{ds}) \\ 0 &= (R_{de} + j\omega_r L_{md}) I_{de} + j\omega_r L_{md}(I_{dh} + I_{pm} + I_{ds}) \end{aligned} \tag{5.8}$$

By solving the equation (5.8), the rotor d-axis eddy current is given as

$$I_{de} = - \frac{j\omega_r L_{md} sR_{dh} (I_{pm} + I_{ds})}{R_{de} sR_{dh} + j\omega_r L_{md} (R_{de} + sR_{dh})} \qquad (5.9)$$

and the rotor d-axis hysteresis current is given as

$$I_{dh} = \frac{(\omega_r^2 L_{md}^2 R_{de} - j\omega_r L_{md} R_{de} sR_{dh}) (I_{pm} + I_{ds})}{R_{de} s^2 R_{dh}^2 - \omega_r^2 L_{md}^2 (R_{de} + sR_{dh}) + j\omega_r L_{md} sR_{dh} (2R_{de} + sR_{dh})} \qquad (5.10)$$

In the same way as obtaining the d-axis voltage equation (5.8), the q-axis voltage equations in phasor form are obtained as

$$\begin{aligned} V_{qs} &= r_s I_{qs} + j\omega_r L_{mq} (I_{qs} + I_{qh} + I_{qe}) + j\omega_r L_{md} (I_{ds} + I_{dh} + I_{qe} + I_{pm}) \\ 0 &= (sR_{qh} + j\omega_r L_{mq}) I_{qh} + j\omega_r L_{mq} (I_{qe} + I_{qs}) \\ 0 &= (R_{qe} + j\omega_r L_{mq}) I_{qe} + j\omega_r L_{mq} (I_{qh} + I_{qs}) \end{aligned} \qquad (5.11)$$

By solving the equation (5.11), the rotor q-axis eddy current is given as

$$I_{qe} = - \frac{j\omega_r L_{mq} sR_{qh} I_{qs}}{R_{qe} sR_{qh} + j\omega_r L_{mq} (R_{qe} + sR_{qh})} \qquad (5.12)$$

and the rotor q-axis hysteresis current is given as

$$I_{qh} = \frac{(\omega_r^2 L_{mq}^2 R_{qe} - j\omega_r L_{mq} R_{qe} sR_{qh}) I_{qs}}{R_{qe} s^2 R_{qh}^2 - \omega_r^2 L_{mq}^2 (R_{qe} + sR_{qh}) + j\omega_r L_{mq} sR_{qh} (2R_{qe} + sR_{qh})} \qquad (5.13)$$

The equivalent source current i_{pm} of the permanent magnet is determined by Ampere's law. This law is stated as the line integral

$$F = \oint_c H \cdot dl = \sum i \qquad (5.14)$$

where c is any closed path or contour, H is the magnetic field intensity, and dl is the

differential line segment on the contour c. In the PMHS motor, the operating point of the permanent magnet lies in the second quadrant. When the motor windings are energized, the operating point dynamically varies following the straight line demagnetization characteristic as described by

$$B_m = B_r + \mu_r \mu_0 H_m \qquad (5.15)$$

where B_r is the remanence as shown in Fig. 2.2 (b). This equation assumes that the magnet remains in a linear operating region during normal operating conditions.

In a PMHS motor with a radial annular air gap, the permanent magnet has the shape of an arc, as shown in Fig. 2.2 (a). During magnetization it is assumed that the same amount of flux magnetizes each differential length. Therefore, integration of these differential elements gives a permanent magnet reluctance

$$\Re_{pm} = \int_{r_i}^{r_i + l_m} \frac{dr}{\mu_r \mu_0 r 2\alpha L} = \frac{1}{2\mu_r \mu_0 \alpha L} \ln\left\{\frac{r_i + l_m}{r_i}\right\} \qquad (5.16)$$

where B_r is the remanence achieved at r_i, and L is the axial length of the permanent magnet. The flux generated by the permanent magnet, which is dependent on remanence B_r, is given as

$$\phi_r = 2 B_r L \alpha r_i \qquad (5.17)$$

Since the flux leaving the permanent magnet is assumed equal to that crossing the air gap, the magnet and air gap flux densities are related by

$$B_g = B_m \frac{A_m}{A_g} \tag{5.18}$$

where A_m and A_g are the cross-sectional areas of the permanent magnet and air gap, respectively.

The permanent magnet flux is easily found by flux division as

$$\phi_{pm} = \frac{\Re_{pm}}{\Re_{pm} + \Re_g} \phi_r \tag{5.19}$$

where the air gap reluctance is modeled simply as $\Re_g = g/\mu_0 A_g$. Knowing ϕ_{pm}, the mmf across the air gap is

$$F_{pm} = \Re_g \phi_{pm} = \frac{2 B_r L \alpha r_i g \ln\left[1 + \frac{l_m}{r_i}\right]}{\mu_o A_g \ln\left[1 + \frac{l_m}{r_i}\right] + 2\mu_r u m_0 \alpha L g} \tag{5.20}$$

Thus, the current source equivalent i_{pm} of the permanent magnet is determined by

$$i_{pm} = \frac{1}{W_1 K_{w1}} F_{pm} \tag{5.21}$$

The equivalent current i_{pm} can also be defined by

$$E_0 = \frac{1}{\sqrt{3}} \omega_r L_{md} i_{pm} \tag{5.22}$$

where E_0 is the phase voltage induced by the permanent magnet only under synchronous speed.

In the PMHS motor the dominant air gap flux is produced by the permanent magnet and residual hysteresis in the rotor. Because the stator currents i_{ds} and i_{qs} in the

rotor frame can be controlled independently, the control of the stator current i_{ds} to zero is applied. In this case there is no magnetizing or demagnetizing along the d-axis and the flux is produced by the permanent magnet and hysteresis materials. Meanwhile, $i_{ds} = 0$ can avoid demagnetizing the permanent magnet material. Because of the d-axis current $i_{ds} = 0$, the first term of the developed torque which is called the reluctance torque component and the last part of the torque which is a negative component related to flux weakening operation, will disappear from the torque equation. Only the main term of the torque, the rotor d axis flux acted with the stator q axis current i_{qs} remains in the torque equation. Thus the torque expression of equation (5.4) can be simplified as

$$T_e = \frac{3}{2} P\left[L_{dm} (i_{dh} + i_{de} + i_{pm}) i_{qs}\right] \qquad (5.23)$$

Equation (5.23) can be simplified as

$$T_e = K_e \phi_m i_{qs} \qquad (5.24)$$

where constant $K_e = 3P/2$ and $\phi_m = L_{dm}(i_{dh} + i_{de} + i_{pm})$. It is obvious that equation (5.24) is similar to the classical expression of torque in any dc motor. In equation (5.23) i_{qs} is the only controllable variable. If the control of $i_{ds} \neq 0$ is required, the current i_{ds} can be positive, and hence it aids the air gap flux along the d-axis. It can also be negative, and then it demagnetises the air gap flux, resulting in a decrease of the total mutual flux. The latter technique can be used in the flux weakening mode of operation.

5.3 Speed control loop transfer function

In the PMHS motor vector control system, the variables such as current, voltage, electromagnetic torque and speed are controlled. Consequently, the multiple control structures which can operate in different internal configurations are used. A series connection control structure is chosen for PMHS motor control as shown in Fig. 5.1. Each variable is subject to continuous control and the various regulator outputs constitute reference values for the subordinated regulators. At each stage, the control signal depends on the actual values of all variables, and regulators $Rx_2,\ldots,Rx_n$ compensate for the disturbances and internal time constants of the various control plant units. The different variables $x_2,\ldots,x_n$ can be easily limited by constraining the output signals of regulators $Rx_1,\ldots,Rx_{n-1}$.

The synthesis of closed-loop control systems in electrical drives consists of constructing simple loops that are easy to optimize by selecting an appropriate type of controller. In most cases, it is possible to obtain control loops which involve one or two dominant time constants as well as the sum of small time constants. Within such loops it is relatively easy to select a controller type satisfying the desired performance index. Symmetry optimum is employed for parameter selection of the speed controller.

One of the most widespread control structures employed in an ac drive is the series speed control system. The block diagram of the system is shown in Fig. 5.2. The PMHS motor has an incremental encoder whose output is utilized for closing the speed loop. The output of the encoder is filtered to remove the ripples to provide the rotor position θ_r and speed ω_r. The speed command ω^*_r is compared with the actual speed ω_r,

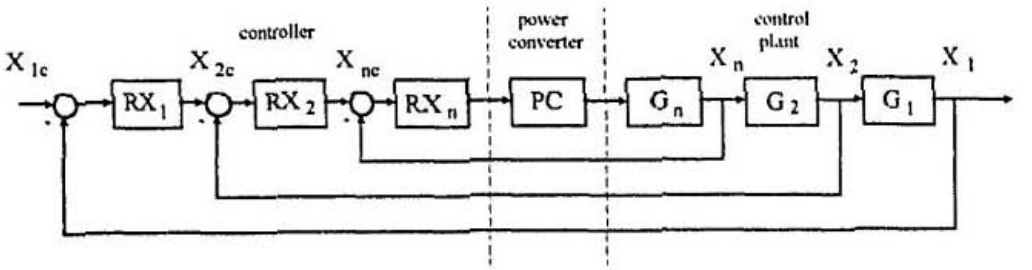

Fig. 5.1 Control structure with series connection

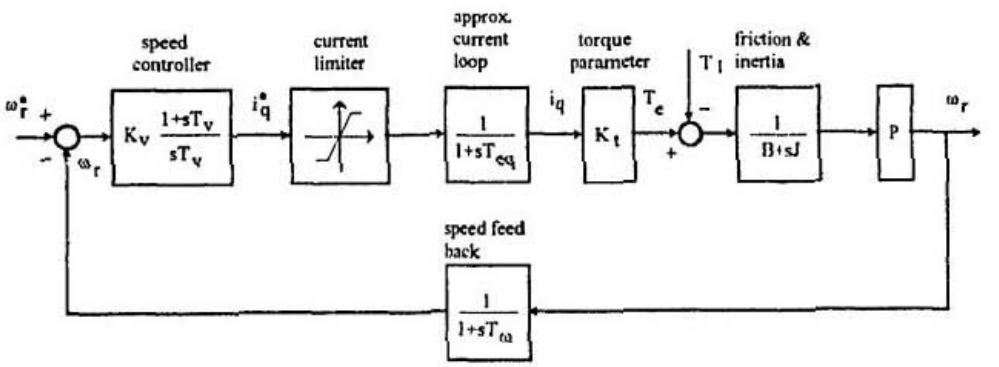

Fig. 5.2 block diagram of speed control system

to produce a speed error signal. This error signal is processed through a speed controller to determine the torque current i_{qs}. The product of torque current i_{qs} times d-axis flux ψ_{ds} generates electromagnetic torque command. The torque command is limited so as to keep it within safe allowable limits and the current command is obtained by proper scaling. Since the d-axis flux is maintained constant, the control of the stator q-axis current is equivalent to control of the torque current in the vector controller. The torque current i_{qs} is obtained from the inner current control feedback loop. The inner current loop assures a fast current response and the current limiter also maintains the current to a safe preset level. This inner current loop makes the converter a linear current amplifier. The outer speed loop ensures that the actual speed is always equal to the commanded speed and any transient is overcome within the shortest time without exceeding the motor and converter capabilities. The transfer functions of the various subsystems will be described in detail in the following subsections.

Speed Controller

The proportional plus integral (PI) control technique is used for the speed controller. It consists of proportional and integral gain constants. The expression for the torque current command i_q^* is given as

$$i_q^* = k_v(\omega_r^* - \omega_r) + \frac{K_v}{T_v}\int(\omega_r^* - \omega_r)\,dt \qquad (5.25)$$

where, K_v and K_v/T_v are the proportional, and integral gain constants, respectively. The transfer function of the speed controller is given as

$$G_v = K_1 \left(\frac{1 + T_1 s}{T_1 s} \right) \tag{5.26}$$

where T_v is the time constant of the controller.

Torque Constant

Rewriting the torque equation (5.23) in which the rotor d axis flux reacts with the stator q axis current i_{qs}. One can obtain the simplified torque expression as

$$T_e = \frac{3}{2} P \left[L_{dm} \left(i_{dh} + i_{de} + i_{pm} \right) i_{qs} \right] = K_t i_{qs} \tag{5.27}$$

$$K_t = \frac{3}{2} P L_{dm} \left(i_{dh} + i_{de} + i_{pm} \right) \tag{5.28}$$

It is worth noting that equation (5.27) is similar to the torque expression in a separately excited dc motor.

Mechanical Inertia and Load

The load is modeled as a function of moment of inertia J with a viscous friction coefficient of B. Then the acceleration torque drives the load. The torque balance equation is given by

$$T_e = J \frac{d\omega_m}{dt} + B\omega_m + T_l \tag{5.29}$$

where T_l is the load torque. The transfer function for the load is given as

$$G_m(s) = \frac{\omega_r}{T_e(s) - T_l} = \frac{P}{Js + B} = P\frac{K_m}{1 + T_m s} \qquad (5.30)$$

where the gain $K_m = P/B$, and the time constant $T_m = J/B$.

Incremental Encoder

The rotor position and speed signal are generated by an optical incremental encoder. The output of the encoder is filtered to remove the ripples to provide the rotor position θ_r and speed ω_r. The transfer function of the speed feedback path is given as

$$G_\omega(s) = \frac{K_\omega}{1 + sT_\omega} \qquad (5.31)$$

Synthesis of Current Control Loop

For the sake of subsequent discussion, the current control loop will be approximated by an inertia element with equivalent time constant T_{eq}. This approximation is based on the current controller integration time T_i. The selection of the current controller integration time T_i is made on the basis of the ratio of motor time constant to the sum of small time constants of the current control loop $T_{\Sigma i}$. When the motor is supplied through a PI controller and PWM inverter, it is assumed that current loop time constant is

$$T_{eq} = 4T_{\Sigma i} \qquad (5.32)$$

for optimization by the symmetry criterion.

It is to be emphasized here that this discussion is correct in terms of the

assumptions made and that it is to be seen as defining certain theoretical guidelines. In practice, the converter dead time, for example, depends on the point of drive operation and consequently the real characteristics may differ somewhat from the theoretical predictions.

As discussed above and refered to in Fig. 5.2, the open loop transfer function of the speed control system is given as

$$G_{vo}(s) = \frac{K_v K_t P (1 + T_v s)}{s T_v (1 + s T_{eq}) (B + sJ) (1 + s T_\omega)}$$

$$= \frac{K_v K_t P (T_v s + 1)}{J T_{eq} T_\omega T_v s^4 + T_v [J (T_{eq} + T_\omega) + B T_{eq} T_\omega] s^3 + T_v [B (T_{eq} + T_\omega) + J] s^2 + B T_v s} \qquad (5.33)$$

and the closed loop transfer function is given as

$$G_{vc}(s) = \frac{K_v K_t P [T_v T_\omega s^2 + (T_v + T_\omega) s + 1]}{J T_{eq} T_\omega T_v s^4 + T_v [J (T_{eq} + T_\omega) + B T_{eq} T_\omega] s^3}$$

$$\frac{}{+ T_v [B (T_{eq} + T_\omega) + J] s^2 + T_v [B + K_v K_t P] s + K_v K_t P} \qquad (5.34)$$

For optimizing and simplifying the speed control system, the symmetry criterion is used. The basic assumptions are as follows.

1. The PMHS drive has n large time constants T_x (x = 1,...,n), each of which is much larger than the sum of small time constants ΣT_μ. The drive transfer function is given by

$$G(s) = \frac{K}{\prod_1^n (1 + s T_x) \prod_1^m (1 + s T_\mu)} \qquad (5.35)$$

2. The elements with large time constants can be replaced by integrating elements

$$\frac{1}{1+sT_r} \approx \frac{1}{sT_r} \qquad (5.36)$$

3. The product of transfer functions for first-order inertia elements with small time constants are simplified to

$$\frac{1}{\prod_1^m (1+sT_\mu)} \approx \frac{1}{1+s\sum_1^m T_\mu} \qquad (5.37)$$

The current loop equivalent time constant for a six-pulse transistor inverter may be estimated to be $T_{eq} \leq 1$ ms. Consider the block diagram of Fig. 5.2. The sum of small time constants for this control loop is given by

$$T_{eq} = T_{ce} + T_\omega \qquad (5.38)$$

where T_{ce} is the equivalent time constant of the current control loop, and T_ω is the speed feedback loop time constant. The transfer function should be further simplified by neglecting the viscous friction parameter B. Thus the open loop transfer function can be obtained as

$$G_{vo}(s) = k_v \frac{1+sT_v}{sT_v} \frac{p}{1+sT_{eq}} \frac{K_t}{sJ} \qquad (5.39)$$

5.4 Speed controller structure and design

The controller is designed as though the speed can be measured directly. In addition, the controller output is allowed to depend upon the speed input, meaning that

no additional state augmentation is necessary. The separation of time-scales also allows the dynamics of the current controller to be ignored for the purpose of speed controller design. The actual current is assumed to reach its commanded value instantaneously.

One way to produce a discrete-time PI control structure is to discretize the continuous time PI controller structure. This results in a similar structure that was used in the current controller.

The optimal properties are found under conditions of symmetry optimization. In this case the phase shift angle represented on the log characteristics of the open control loop attains its peak value for the cross-over frequency ω_D. Therefore, the cross-over frequency ω_D is just in the middle between $\omega_v = 1/T_v$ and $\omega_{eq} = 1/T_{eq}$ in the logarithmic scale. The cross over frequency can be obtained from the following relations as

$$\log\omega_D = \log\omega_v + \frac{1}{2}(\log\omega_{eq} - \log\omega_v) = \log\omega_v \left[\frac{\omega_{eq}}{\omega_v}\right]^{\frac{1}{2}} \qquad (5.40)$$

$$\omega_D = \sqrt{\omega_v \omega_{eq}} \qquad (5.41)$$

and

$$T_D = \frac{J}{K_v P K_t} \qquad (5.42)$$

From equations (5.41) and (5.42) the proportional part of the controller under symmetry optimization is given as

$$K_v = \frac{J}{T_D P K_t} = \frac{J}{P K_t \sqrt{T_v T_{eq}}} \qquad (5.43)$$

For a given time constant T_{eq}, one obtains dynamic responses which depend solely on the

speed controller integration constant T_v. It can be easily demonstrated that the transfer function $G_{vc}(s)$ of the closed control loop is given by

$$G_{vc}(s) = \frac{G_{vo}(s)}{1+G_{vo}(s)} = \frac{\Delta\omega_r(s)}{\Delta\omega_r^*(s)} = \frac{1+sT_v}{1+sT_v+s^2T_vT_D+s^3T_vT_DT_{eq}} \tag{5.44}$$

while the output-disturbance transfer function $G_{lc}(s)$ is given as

$$G_{lc}(s) = \frac{\Delta\omega_r(s)}{\Delta T_l(s)} = G_{vc}(s)\,s\frac{T_v(1+sT_{eq})}{K_v(1+sT_v)} = s\frac{T_v}{K_v}\frac{1+sT_{eq}}{1+sT_v+s^2T_vT_D+s^3T_vT_DT_{eq}} \tag{5.45}$$

For optimal response, the magnitude of the frequency response is close to one over a wide frequency range which guarantees a high bandwidth and hence faster response. The gain factor of the speed controller is selected from equation (5.43). It is found that for $T_v/T_{eq} = 4$, one obtains the symmetry optimum condition. Then the speed closed loop transfer $G_{vc}(s)$ function reduces to

$$G_{vc}(s) = \frac{1+4sT_{eq}}{1+4sT_{eq}+8s^2T_{eq}+8s^3T_{eq}} \tag{5.46}$$

The equation (5.46) is valid for the symmetric optimum condition. For the open loop transfer function, the corner points are $1/4T_{eq}$ and $1/T_{eq}$ with the gain crossover frequency of $1/2T_{eq}$. The slope of the magnitude response in the gain crossover frequency is -20dB/decade which is the most desirable characteristic for good dynamic behaviour.

Because of its symmetry at the gain crossover frequency, this transfer function is known as a symmetric optimum function. The step response of the transfer function is given by

$$g_{so}(t) = 1 + e^{-\frac{t}{2}T_{eq}} - 2e^{-\frac{t}{4}T_{eq}} \cos\left[\frac{\sqrt{3}\,t}{4T_{eq}}\right] \qquad (5.47)$$

Using the first order filter $T_f = T_v$ for the speed command, the transfer function will be

$$G_{sc}(s) = \frac{1}{1 + 4sT_{eq} + 8s^2T_{eq} + 8s^3T_{eq}} \qquad (5.48)$$

The step response for this modified transfer function is given as

$$g_{so}(s) = 1 - e^{-\frac{t}{2T_{eq}}} - \frac{2}{\sqrt{3}} e^{-\frac{t}{2T_{eq}}} \sin\left[\frac{\sqrt{3}\,t}{4T_{eq}}\right] \qquad (5.49)$$

The denominator of the closed loop transfer function (5.46) can be written as

$$\begin{aligned} denominator &= \left[s + \frac{1}{2T_{eq}}\right]\left[2s^2T_{eq} + s + \frac{1}{2T_{eq}}\right] \\ &= \left[s + \frac{1}{2T_{eq}}\right]\left[s + \frac{1}{4T_{eq}} + j\frac{\sqrt{3}}{4T_{eq}}\right]\left[s + \frac{1}{4T_{eq}} - j\frac{\sqrt{3}}{4T_{eq}}\right] \end{aligned} \qquad (5.50)$$

It is clear that the real part of the poles of the equation (5.46) is negative so the system is stable. For the symmetric optimum design, the system stability is usually guaranteed.

This approach indicates one of the possible methods to synthesize the speed controller. The judicious choice of approximations is based on the physical parameters of the motor, inverter, filter and transducers.

Fig. 5.3 is a Bode plot of the open loop speed control system for different values of K, where $K = T_v/T_{eq}$. The gain margins are about 25 dB and the phase margins vary

from 20° to 50°. It is to be noted that the phase angle of the loop transmission starts near -180° for low frequencies, rises toward its maximum near the gain cross over frequency, and then falls off again at higher frequencies. Note that the function closely follows the characteristics of the symmetric optimum function, and the controller maintains sufficient phase margin to ensure the closed loop system stability.

Fig. 5.4 shows the unit step response of closed speed control system. Fig. 5.4 (a) is the step response of equation (5.44). Fig. 5.4 (b) is a step change of speed command, when an input filter with time constant $T_f = T_v$ is used. The use of the input filter significantly reduces the speed overshoot while the control loop retains its stability. It should be noted that such a time domain response is achieved if there is no limit on the torque produced by the motor, since a linear relationship between the speed error and the torque is assumed. But in the practical PMHS motor drive system, the torque capability of the motor and the current capability of the inverter limit the maximum allowable torque. Thus this time domain response represents only the small signal response of the system. Fig. 5.5 and Fig 5.6 show the Bode plot of the closed speed loop control system with and without input filter, respectively.

The design is carried out in the frequency domain. Defining the s-plane transfer function for the control system, the proportional and integral gains of the speed controller are adjusted until the loop transmission has the required bandwidth and phase margin. It should be noted that the usual design relationships between bandwidth, phase margin, and transient response are in terms of a second order system. Even using one order to represent the current control loop, the speed control system is still fourth order, with

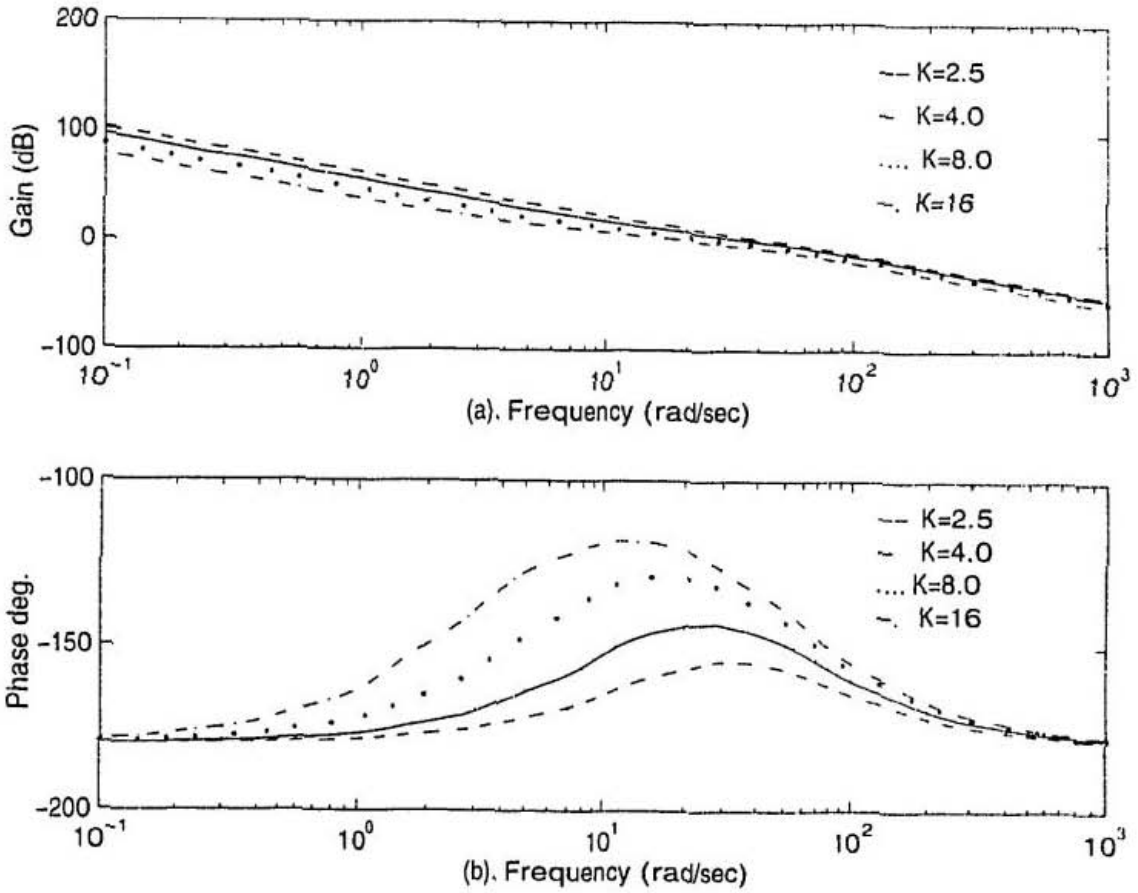

Fig. 5.3 Speed open loop Bode plot

(a) gain margin

(b) phase margin

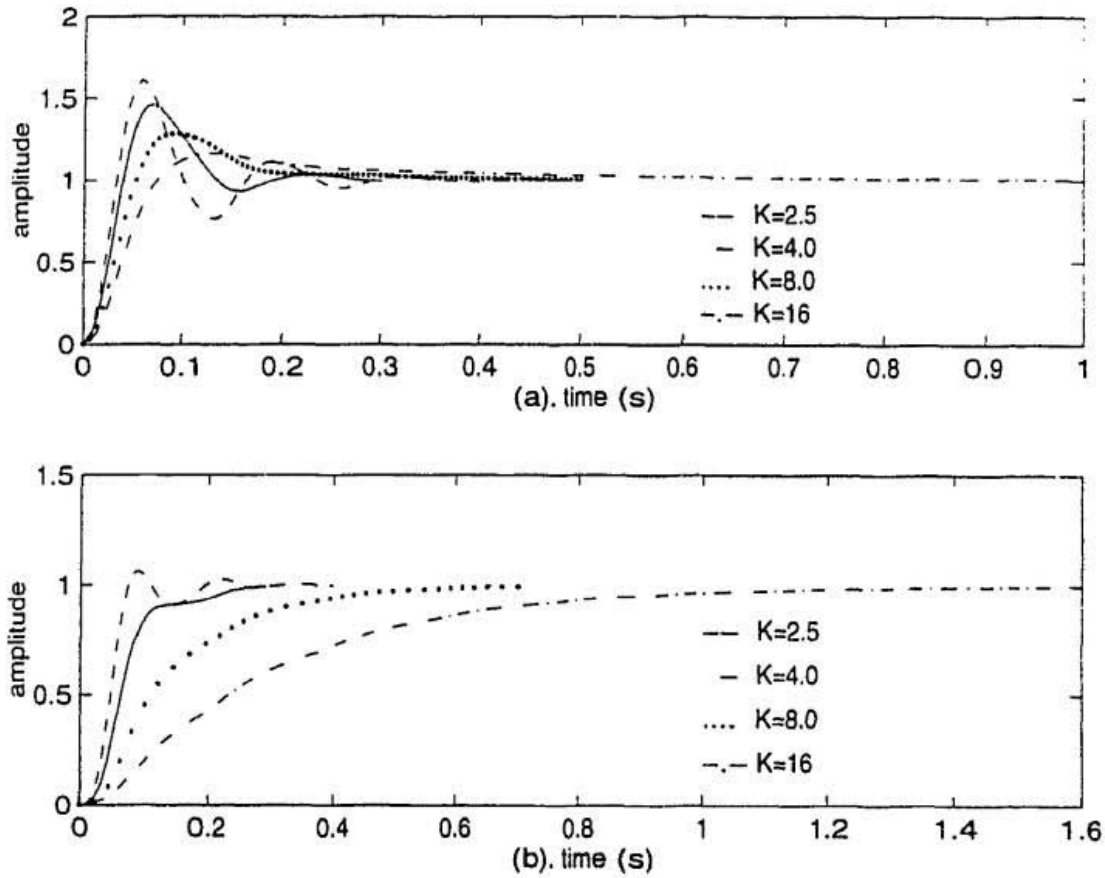

Fig. 5.4 Unit-step response of speed control system

(a) closed loop transfer function with one zero

(b) closed loop transfer function without one zero

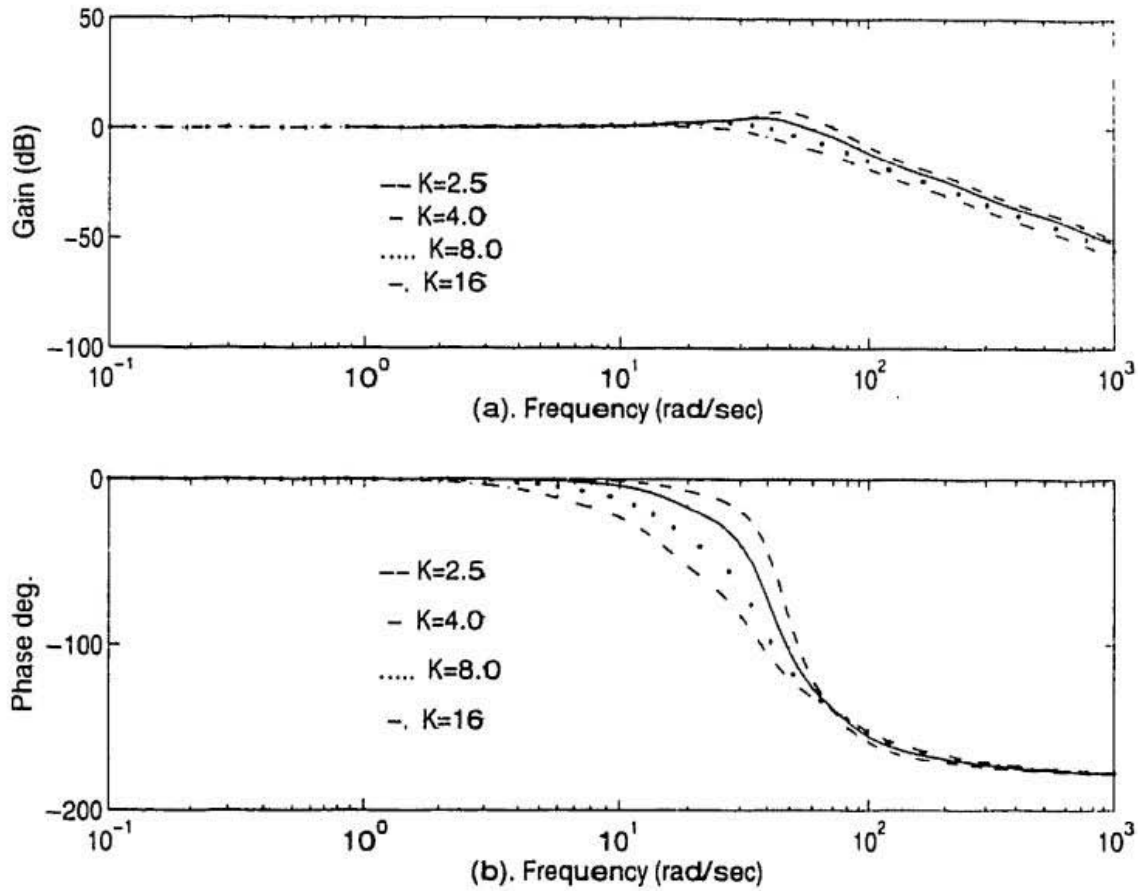

Fig. 5.5 Speed closed loop Bode plot with zero

(a) gain margin

(b) phase margin

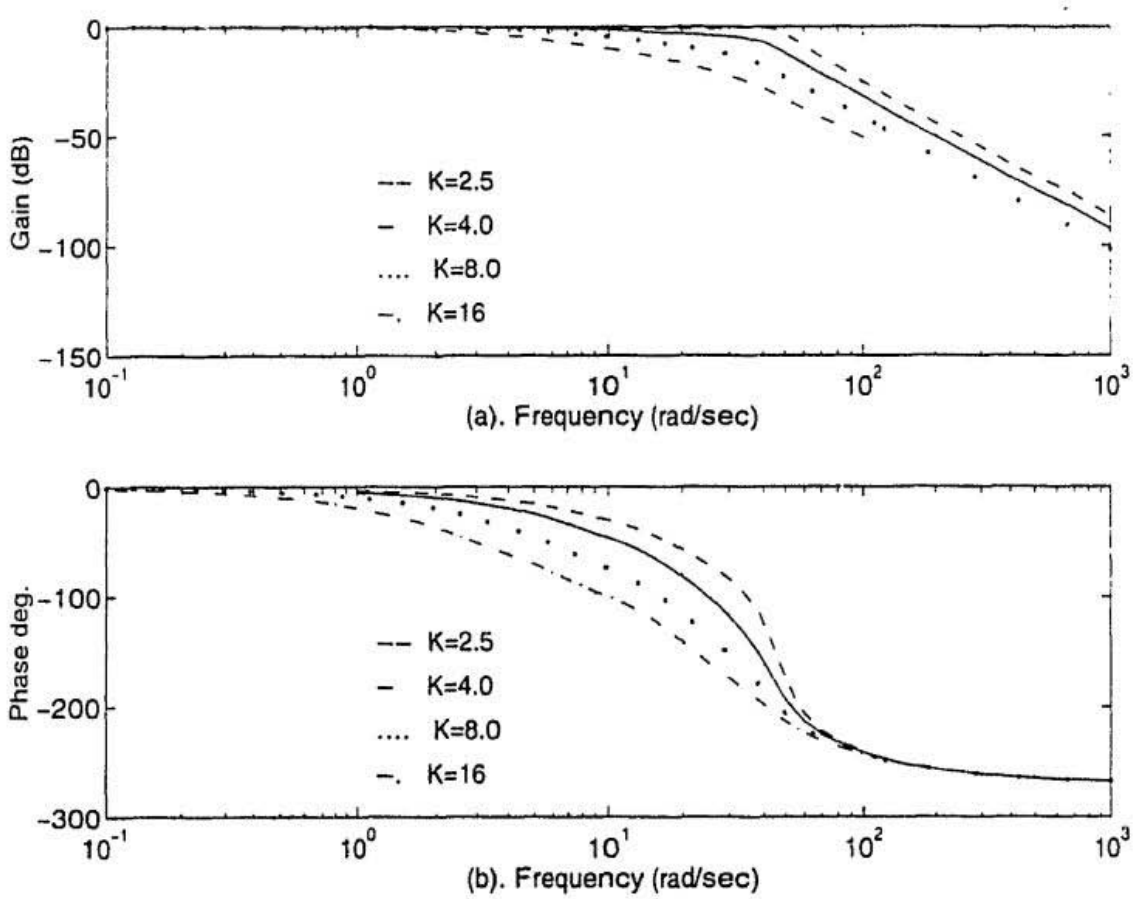

Fig. 5.6 Speed closed loop Bode plot without zero

(a) gain margin

(b) phase margin

poles that are not necessarily widely separated. Thus, these design rules are used only as guides in the design process.

Acceptable performance is obtained when K=4 is chosen. Fig. 5.3 shows that the gain margin is about 25 dB and the phase margin is nearly 35°. The step response shows small overshoot and rapid rise time.

5.5 Speed control implementation and experimental results

The performance of the speed control system is demonstrated by testing the motor at different speed. Fig. 5.7 shows the rotor position and speed vs time in the steady state mode for different values of frequencies. Figs. 5.7 (a), (c), (e) and (g) show the rotor position at 1Hz, 12Hz, 36Hz and 60Hz, respectively. Figs. 5.7 (b), (d), (f) and (h) show the rotor speed when the frequencies are 1Hz, 12Hz, 36Hz and 60Hz, respectively. The rotor position output is from the shaft digital incremental encoder. The rotor position is represented by radian. For the 4-pole experimental PMHS motor, the rotating angle will be set to zero whenever it reaches 2π radian. The rotor angular speed is represented by radian per second (rad./sec.). For the frequency of 1Hz, 12Hz, 36Hz and 60Hz, the rotor angular speed are 3.14, 37.70, 113.10 and 188.50 rad./sec., respectively, and the rotor speed is 30, 360, 1080 and 1800 revolution per minute (rpm), respectively. The speed curves clearly show that the PMHS motor runs quite smoothly without any oscillation over the wide speed range, even at 30 rpm for a supply frequency of 1 Hz.

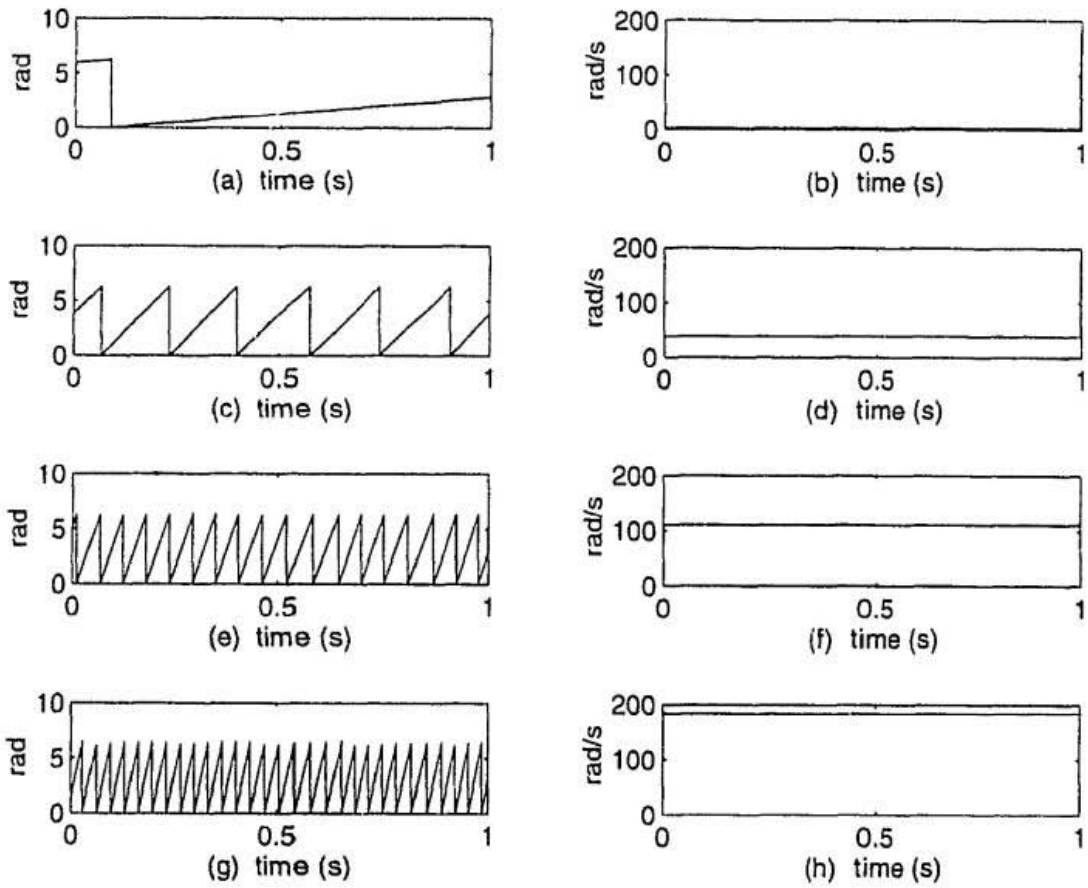

Fig. 5.7 Steady state performances of the rotor position and speed

(a) rotor position at 1 Hz; (b) rotor speed at 1 Hz
(c) rotor position at 12 Hz; (d) rotor speed at 12 Hz
(e) rotor position at 36 Hz; (f) rotor speed at 36 Hz
(g) rotor position at 60 Hz; (h) rotor speed at 60 Hz

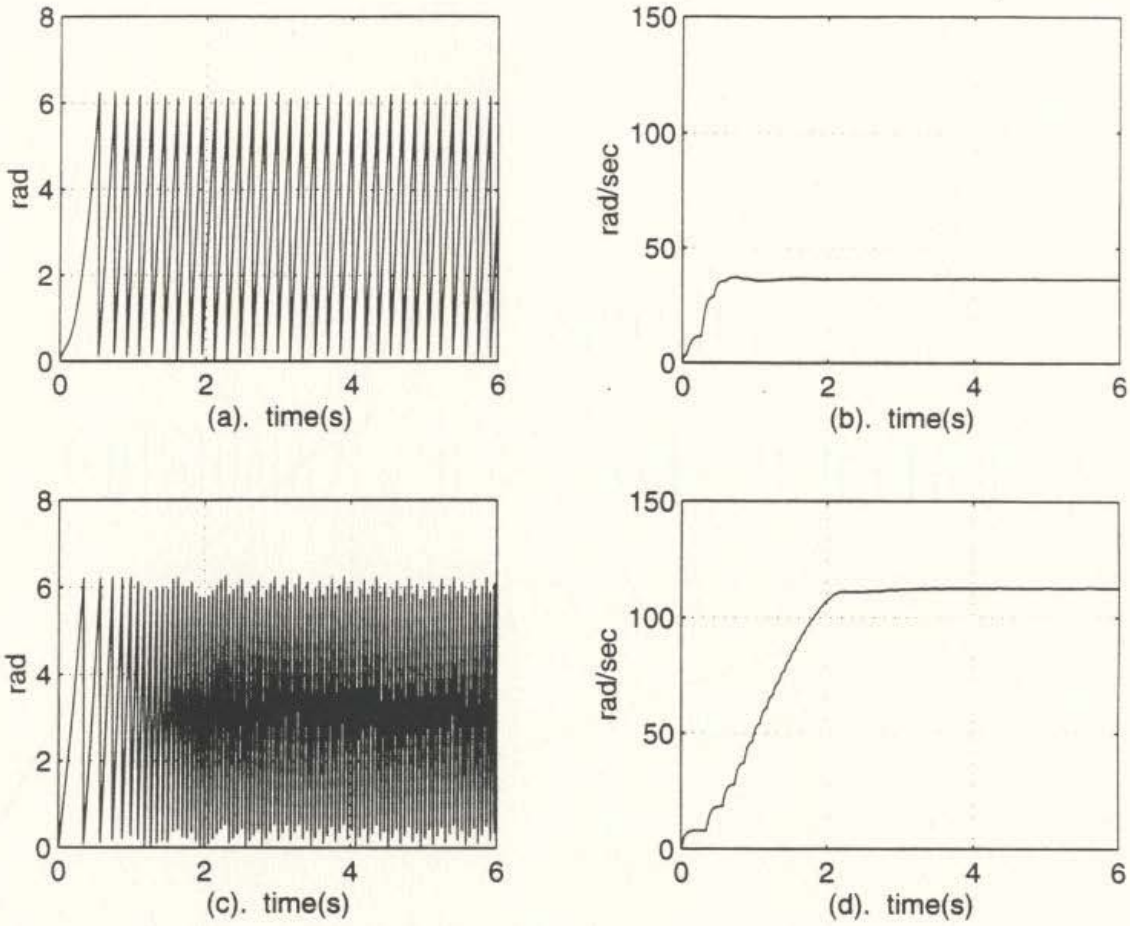

Fig. 5.8 Transient performance of the rotor position and speed

(a) rotor position at 12 Hz; (b) speed respose at 12 Hz

(c) rotor position at 36 Hz; (d) speed respose at 36 Hz

Fig. 5.8 shows the transient performances of the speed control system. Figs. 5.8 (a) and (b) show the rotor position and angular speed performances when the rotor runs from standstill to 37.70 rad./sec. which represents 360 rpm. The rise time is about 1 second and there is a small overshoot. Then, the motor runs very stably. Figs. 5.8 (c) and (d) show the rotor position and angular speed performances when the rotor runs from standstill to the 113.10 rad./sec. which represents the 1080 rpm. The overshoot is almost zero in this situation. It is to be observed that the PMHS motor obtains remarkable steady state and dynamic stability at low frequency operation. Thus it is a distinct advantageous feature over those conventional synchronous motors at low speed operation.

5.6 Summary

The speed controller for the PMHS motor has been developed in this chapter. The controller operates as the outer loop of the multi-loop control system and issues commands to the current control loop in order to adjust the electromagnetic torque of the motor.

First, the general expression of the developed torque of the PMHS motor was derived. Then the torque equation was analyzed for the vector control purpose. The expression of the rotor hysteresis current, eddy current and equivalent permanent magnet source current were also presented. Because the control of the stator current i_{ds} to zero is applied, i_{qs} is the only controllable variable. Thus the torque equation is similar to the classical expression of torque in any dc motor.

For optimizing and simplifying the speed control system, the symmetry criterion

is used on the basic assumptions. For the convenience of controller design, the transfer function is simplified that the current control loop is approximated by an inertia element with equivalent time constant T_{eq}. It may be emphasized here that this approximation is acceptable in terms of the assumptions made. In practice, some parameters depend on the point of drive operation and consequently the real characteristics may differ somewhat from the theoretical predictions.

Because the real part of the poles of the transfer function are negative the system stability is guaranteed for the symmetric optimum design. Then, the Bode plot of both the open and closed loop speed control system, and the unit step responses of closed speed control system were given.

The performance of the speed controller was then demonstrated with several real-time experiments. The speed controller was shown to possess the desired characteristics in terms of rise time and overshoot. The steady state rotor position and speed response are quite smoothly in a wide speed range and without any oscillation.

Chapter 6

System Implementation and Experimental Results

6.1 Introduction

In the previous chapters, the PMHS motor and inverter models, and the current and speed controllers were presented. This chapter describes the hardware and software implementation of the digital signal processor based vector control system of the permanent magnet hysteresis synchronous motor.

In implementing this control system, the system's major functions and their interconnections are described by means of a functional diagram. Then a brief description of the system software is presented.

The hardware requirements of each function are discussed separately. First, the DS1102 DSP controller board which plays the main role in the control system is described. This includes the architectural overview, host interface description, analog to digital and digital to analog subsystems, and slave DSP application.

Then the experimental permanent magnet hysteresis synchronous motor and

voltage source inverter are presented. Next, the operating principle and structure of the optical incremental encoder, the rotor position measurement and rotor speed calculation are described. Finally, experimental results which include steady state and starting process of the drive system at different frequencies are presented.

6.2 General Description of the PMHS Vector Control System

The DS1102 DSP based vector control of a PMHS motor was successfully implemented and tested. The general hardware and software descriptions of the control system are included in this subsection.

6.2.1 System General Hardware Description

The following is a brief description of the experimental set-up of the whole control system. The main equipment used in the experimental set-up are:

- DS1102 DSP board
- 386 personal computer
- Three phase full wave rectifier module
- 0-20 V dc power supply
- P111 VSI voltage source transistor inverter
- L100 AM gate signal amplifier
- Interface circuits between DSP board and inverter

- PMHS motor with dc loading machine
- H25D optical incremental encoder
- Hall effect current sensors
- Tektronix 2212 digital storage oscilloscope
- Voltage and current meters
- Resistance bank

Fig. 6.1 shows the experimental setup of DSP based vector control system of the PMHS motor. It consists of five parts: the DS1102 DSP board, the voltage source inverter, the interface circuits, the PMHS motor with load and rotor position and stator current measurements, as shown in Fig. 6.2. All of the calculations and signal processing are carried out by the DSP board. These calculations include d-q axis current controller, speed controller, speed calculation, voltage and current vector rotators, digital filters, reference voltage calculation, digital sinusoidal pulse width modulation (SPWM) signals generation, analog to digital and digital to analog signal transformations. The programs are downloaded into TMS320C31 master DSP and TMS320P14 slave DSP chips. The digital switching signals that are to be fed to the inverter to drive the PMHS motor are determined by the DSP board. These signals are based on the comparison of the reference currents derived and actual currents as well as rotor position fed back. The actual currents are measured using Hall effect current transducers and the rotor position is obtained from the optical incremental encoder attached to the motor shaft. The dc machine, coupled to the PMHS motor and connected to the resistance bank, acts as a loading machine.

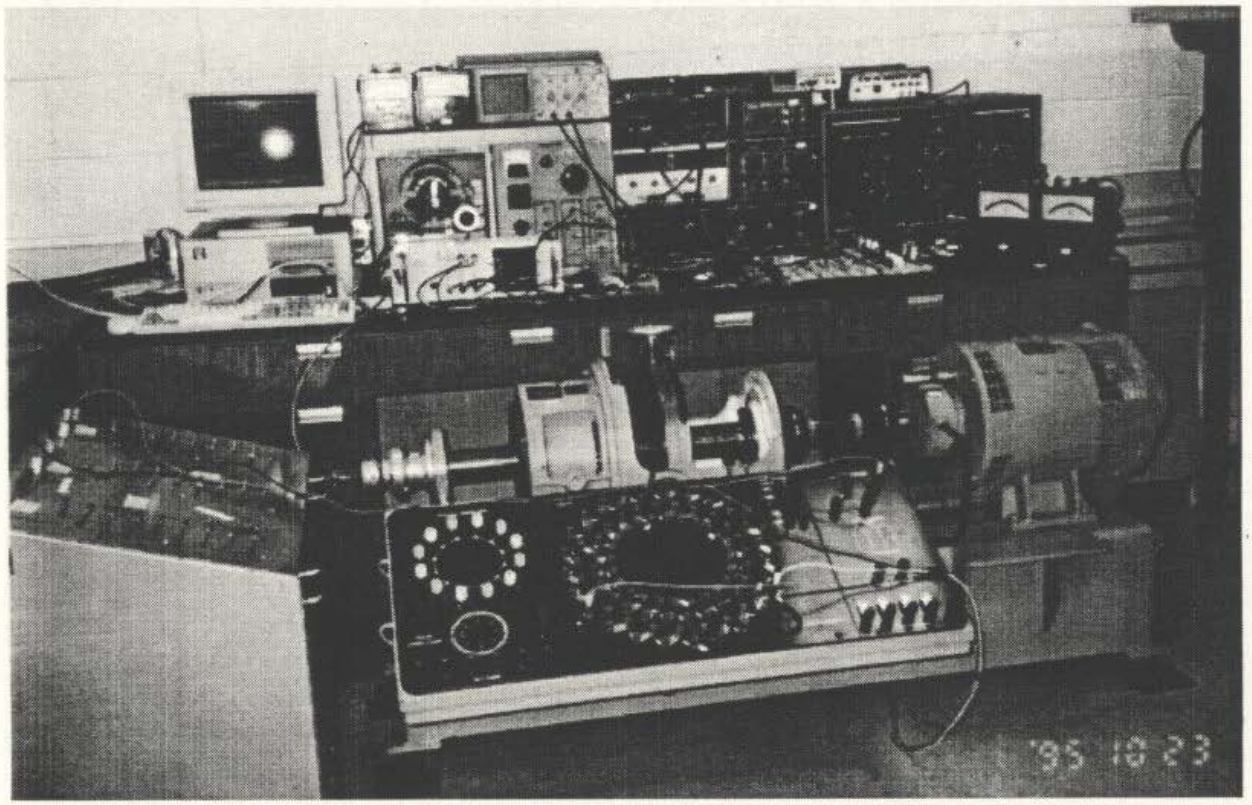

Fig. 6.1 Experimental setup of DSP based vector control of PMHS motor

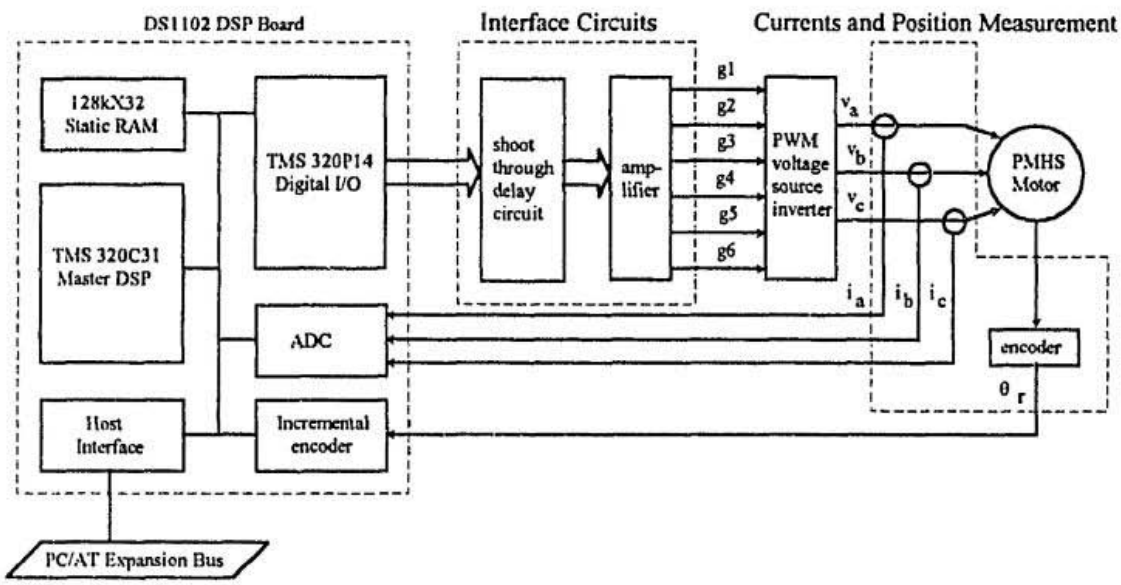

Fig. 6.2 Experimental setup block diagram

6.2.2 System General Software Description

Fig. 6.3 shows the block diagram of the vector control scheme for the PMHS motor. The control system software is carried out by the DS1102 DSP board. The input signals of the DSP board are three phase stator currents and rotor position, and the output of the DSP board is the digital switching signals that are fed to the inverter. The flow chart of the main program for the PMHS motor vector control system is shown in Fig. 6.4. In the control system, rotor speed is obtained from rotor position and timing counter. The three phase stator current signals which include both the magnitude and phase information are obtained by the digital filter. Because the current controllers are designed in the rotor d-q axis frame, the stator currents are transferred into the orthogonal stator frame α-β axis first, then transferred into the rotor d-q axis to get currents i_d and i_q. The speed signal ω_r obtained from the rotor position and timing counter is fed back to compare with the reference speed ω_r^*. The speed error is the input of the speed controller. The output of the speed controller is the q-axis reference current i_q^*. Both the d-q axis currents i_d and i_q are fed back to compare with the d-q axis reference currents i_d^* and i_q^*, respectively. The current errors e_d and e_q are the input of the d-axis and q-axis current controllers. The rotor d-q axis voltages v_d and v_q are generated by the combination of the current controllers output and the back emf. These rotor frame voltages need to be transformed into the stator three phases frame again. Thus the three phases stator frame reference voltages v_a^*, v_b^* and v_c^* are obtained by the voltage vector rotator. Finally, 6-channel sinusoidal pulse width modulation signals are fed into the interface circuit to control the 6-pulse transistorized voltage source inverter.

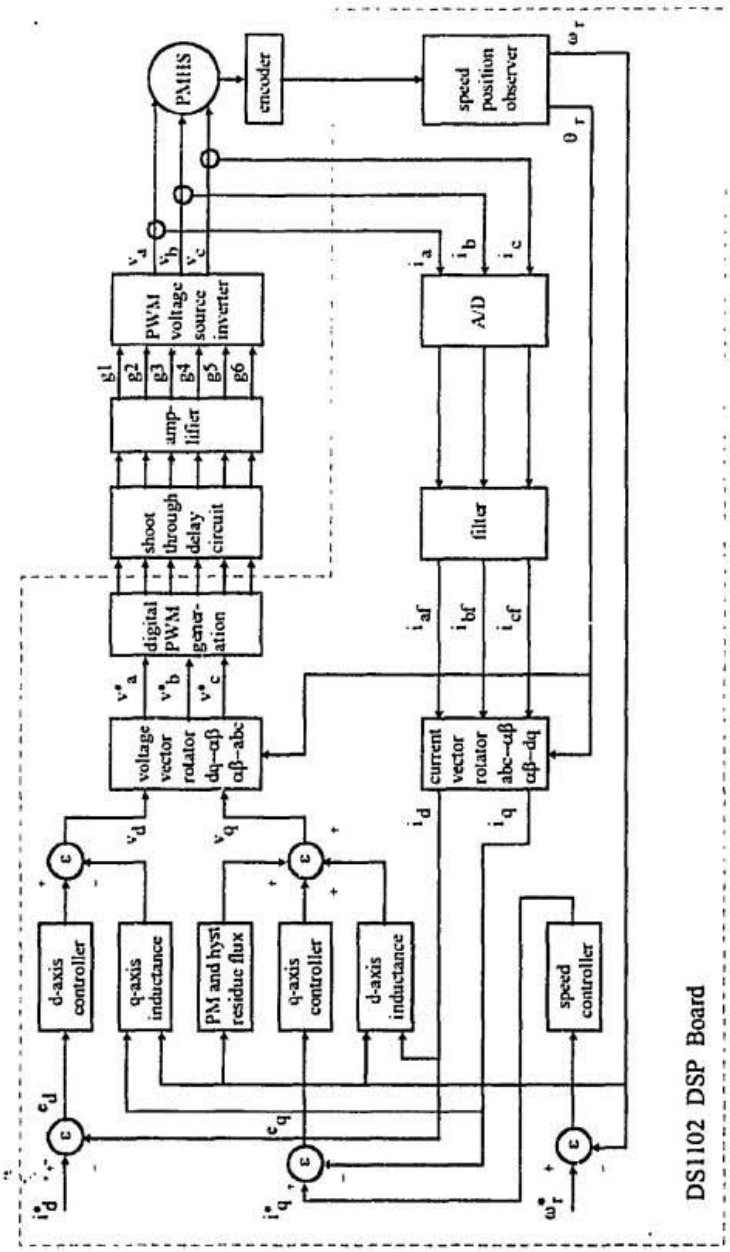

Fig. 6.3 The block diagram of the vector control scheme for the PMHS motor

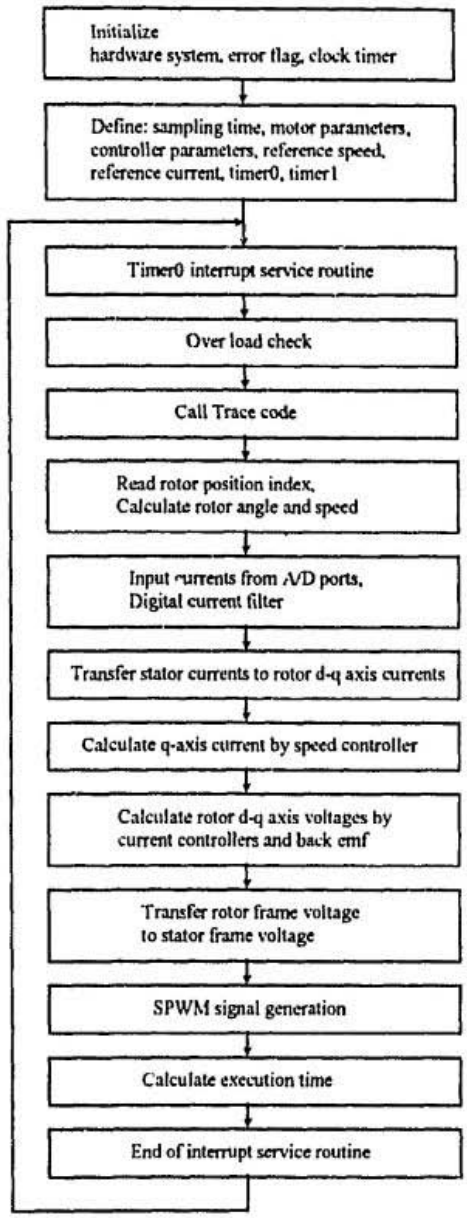

Fig. 6.4 The main program flow chart of the PMHS motor vector control

6.3 DS1102 DSP Control Board

The digital signal processor is a specialized microprocessor whose architecture is optimized to perform its task efficiently. The DS1102 DSP board is specifically designed for the development of high speed multivariable digital controllers and real time control in motor drives and vehicle controls, as well as for general digital signal processing tasks. The DS1102 DSP board contains two DSPs. The main processor is the Texas Instruments TMS320C31 floating point digital signal processor which has the main processing unit providing fast instruction cycle time for numeric intensive algorithms. The second processor is the TMS320P14 DSP used for many different digital I/O functions. The DSP has been supplemented by a set of on-board peripherals frequently used in digital control systems. Analog to digital and digital to analog converters, a digital I/O subsystem and incremental sensor interface make the DS1102 an excellent DSP board solution for a broad range of digital control tasks for PMHS motor drives.

Architectural overview

The DS1102 board is built around the TMS320C31 DSP. It contains 128K Words memory fast enough to allow zero wait state operation. Several peripheral subsystems are implemented to support a wide range of digital signal processing applications. Fig. 6.5 presents a block diagram of the DS1102. The TMS320C31 supports the total memory space of 16M 32-bit words including program, data and I/O space. All off-chip memory and I/O can be accessed by the host, even while the DSP is running thus allowing easy system setup and monitoring.

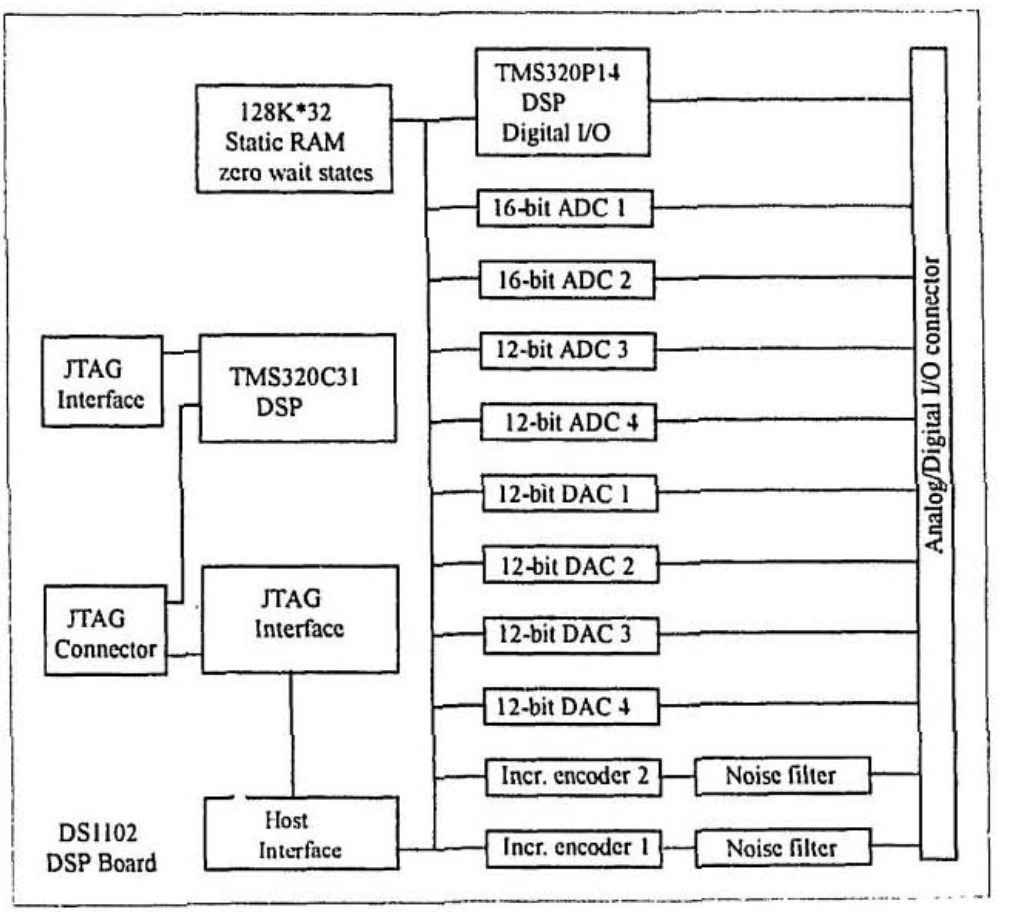

Fig. 6.5 Block diagram of the DS1102 DSP board

The TMS320C31 DSP

The TMS320C31 third generation floating point DSP is a high performance member of Texas Instruments' TMS320 family of VLSI digital signal processors. It performs parallel multiply and arithmetic logic unit (ALU) operations on integers or floating point numbers in a single cycle. It supports a large address space with various addressing modes allowing the use of high level languages for application development. Some key features of the TMS320C31 are:

- 50 ns single cycle instruction execution time
- Two 1K*32-bit dual access on chip data RAM blocks
- 64*32-bit instruction cache
- 32-bit instruction and data words, 24-bit addresses
- 40/32-bit floating point /integer multiplier and ALU
- 32-bit barrel shifter
- Eight 40-bit accumulators
- Two independent address arithmetic units
- Serial port
- DMA controller for concurrent DMA and CPU operation
- Four external interrupts
- Two 32-bit timers

A/D subsystem

The DS1102 contains two types of analog to digital converters:

• Two 16-bit auto-calibrating sampling A/D converters with integrated sample/holds.

• Two 12-bit sampling A/D converters with integrated sample/holds.

The A/D register addresses are shown in Table 6.1

Table 6.1 A/D subsystem register addresses

Address	Register
023000H	Channel 1 16-bit ADC data register
023001H	Channel 2 16-bit ADC data register
023002H	Channel 3 12-bit ADC data register
023003H	Channel 4 12-bit ADC data register
025000H	Calibration start flag

All ADCs have single ended bipolar inputs with ± 10 V input span. All return lines are connected to system ground. To avoid ground loops, separate return lines should be used for all connected sensors and the sensor grounds should be isolated from each other.

D/A subsystem

The DS1102 board contains four 12-bit digital to analog converters with programmable output voltage ranges. The D/A subsystem consists of four data registers,

four output registers, a mode register and a strobe bit register. The register addresses are shown in Table 6.2.

Table 6.2 D/A subsystem register addresses

Address	Register
022000H	Channel DAC data register
022001H	Channel DAC data register
022002H	Channel DAC data register
022003H	Channel DAC data register
026000H	Mode select register
026001H	Mode strobe register

The DACs have single ended voltage outputs with ± 10 V span. The return lines of the outputs are connected to system ground. Each DAC features a set of two back to back registers, a data register connected to the data inputs and an output register connected to D/A converter. This allows the DAC to sequentially preload new output values and then to update the D/A outputs simultaneously by copying the contents of the data registers to the output registers by a common transfer strobe.

Digital I/O subsystem

The DS1102's digital I/O subsystem is based on the TMS320P14 DSP. The Digital I/O subsystem register address is given in Table 6.3.

Table 6.3 digital I/O subsystem register addresses

Address	Register
021000H	Slave DSP communication port

Besides a 16-bit fixed point DSP core, it has a bit-selectable parallel I/O port, four timers, six PWM circuits, four capture inputs and a serial interface. The TMS320P14 contains firmware making all on-chip peripherals accessible by the TMS320C31. After power up the DSP executes an I/O server firmware residing in its built in program PROM. This PROM has been augmented by an external program RAM providing a program download feature which allows application specific DSP programs to be executed in parallel to TMS320C31.

Incremental encoder subsystem

The DS1102 contains two incremental sensor interfaces to support optical incremental sensors used in the PMHS motor vector control. The register addresses of the incremental encoder are given in the Table 6.4

Table 6.4 Incremental encoder subsystem register addresses

Address	Register
024000H	Channel 1 incremental encoder position counter register
024001H	Channel 2 incremental encoder position counter register

Each interface contains line receivers for the input signals, a digital noise pulse filter eliminating spikes on the phase lines, a quadrature decoder which converts the sensor's phase information to count up and count down pulses, a 24-bit counter which holds the current position of the sensor and a 24-bit output latch. Fig. 6.6 shows the block diagram of an incremental sensor interface. The minimum encoder state width is 120 ns resulting in a maximum count frequency of 8.3 MHz. Noise pulses shorter than 80 ns are eliminated by the digital noise filter.

After power up the position counters contain arbitrary data and must be synchronized to the absolute position of the connected motor. This is accomplished by moving the respective sensor until an index pulse is encountered. To monitor the index lines the index pulses are fed to the TMS320C31's interrupt lines. When the DSP has detected an index line it may reset the respective position counters by setting the flags. The output data can be read via the corresponding position counter register. The 5 V sensor supply voltage output is connected to the host's 5 V power supply via a multifuse.

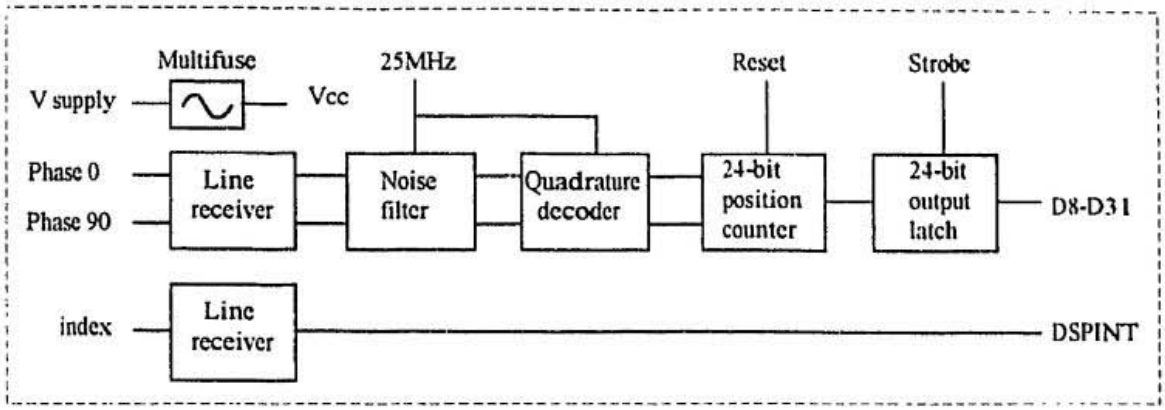

Fig. 6.6 Block diagram of an incremental encoder interface

6.4 Experimental PMHS Motor and Inverter

The experimental 5 hp permanent magnet hysteresis synchronous motor used in this thesis is the Mawdsley's Multiform Research Machine Set. It is a generalized experimental machine whose stator windings can be connected to different number of poles and phases for operation. In the experiment, the stator windings were configured as a 4-pole, delta-connection with rated line voltage of 208 V. The permanent magnet hysteresis rotor was inserted in the Mawdsley machine stator. The rotor hysteresis material is made of 36% Cobalt-steel alloys and the Neodymium Iron Boron (NdFeB) permanent magnets are arranged within the hysteresis material. Fig. 6.7 is a picture of the PMHS motor rotor and stator. The pertinent properties of the rotor materials, design dimensions and the parameters of the experimental PMHS motor are given in Appendix A1.

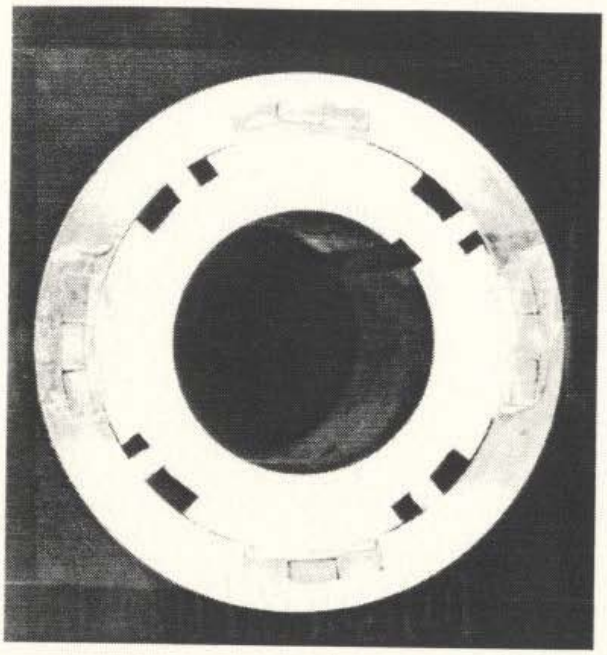

(a) Experimental PMHS motor rotor

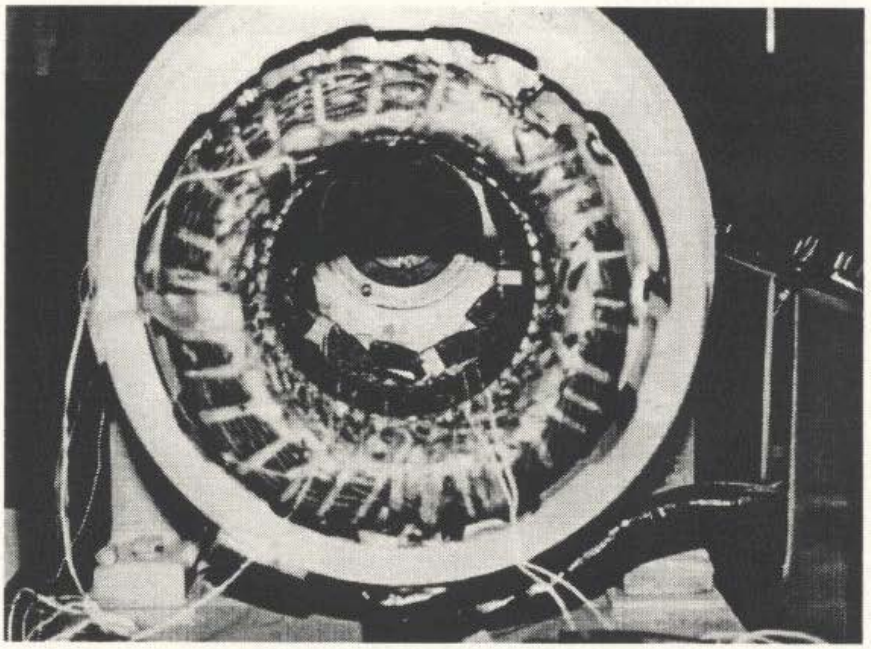

(b) Experimental PMHS motor stator

Fig. 6.7 Experimental PMHS motor

In general, the 3-phase ac voltage available in a laboratory is of a variable voltage and fixed frequency type. Such a power supply is not suitable for the variable speed operation of a PMHS motor, the speed of which depends on the supply frequency. Hence the inverter, which can convert the three phase fixed frequency ac into a variable voltage with variable frequency, is required in the PMHS motor drive. There are one ac-dc converter and one dc-ac inverter in this drive system. The first one is to convert constant frequency utility ac supply to a dc voltage source using a diode bridge rectifier. The bridge rectifier along with the dc link capacitance performs this conversion. The second one is a three phase inverter which converts the dc link voltage to a variable frequency ac voltage and serves as the input to the PMHS motor. Six transistors are used to build this three phase inverter. The six gate signals from the DSP board are fed through a gate drive circuit and amplifier, and then switch the appropriate devices. The three outputs of the inverter are then fed to the corresponding phases of the motor terminals.

6.5 Rotor Position and Stator Current Measurements

Only two feedback signals are needed for this vector control system. One is the rotor position and the other is the stator currents. In the PMHS motor drive system, the rotor position sensor is an important part of the overall system.

6.5.1 Optical Incremental Encoder

The incremental encoder has a simple structure. Besides, it can easily transmit signals because it has fewer electrical wires for output. The output pulses of the encoder

do not show the absolute value of the rotational position of the axis. The number of pulses is proportional to the rotational angle of the axis. The absolute value of the rotational position of the axis is shown by the result of accumulating the output pulses of the encoder by using a counter.

Fig. 6.8 is a structural drawing of an incremental encoder's relative angular position detector of output A and B type, having signal Z of phase zero.

The light projected from the LED goes through the slits of the rotary disc and each of the slits A, B and Z of the fixed board with slits. Then the light is detected by the light receiving devices A, B, and Z. Slits A and B on the fixed board with slits have a phase difference of 90 degrees. The electrical output, with its waveform shaped, is a rectangular wave with the same 90 degree phase difference. Fig. 6.9 shows the output waveforms of the H25 incremental optical encoder. When encoder's shaft is rotated, it generates two pulse signals with a 90 degree phase shift. The frequency of the encoder output waveforms is proportional to the speed at which the encoder shaft is rotating. The sign of the phase shift of signal B with respect to signal A determines the direction of rotation. If signal B lags signal A, the rotation is counterclockwise viewed from the shaft, otherwise, the opposite is true.

The rotor position can be obtained from the encoder output waveform by counting the rising edges of a pulse train signal with a digital counter. For an incremental encoder with a given number of pulse per revolution, the resolution of the position measured is given by

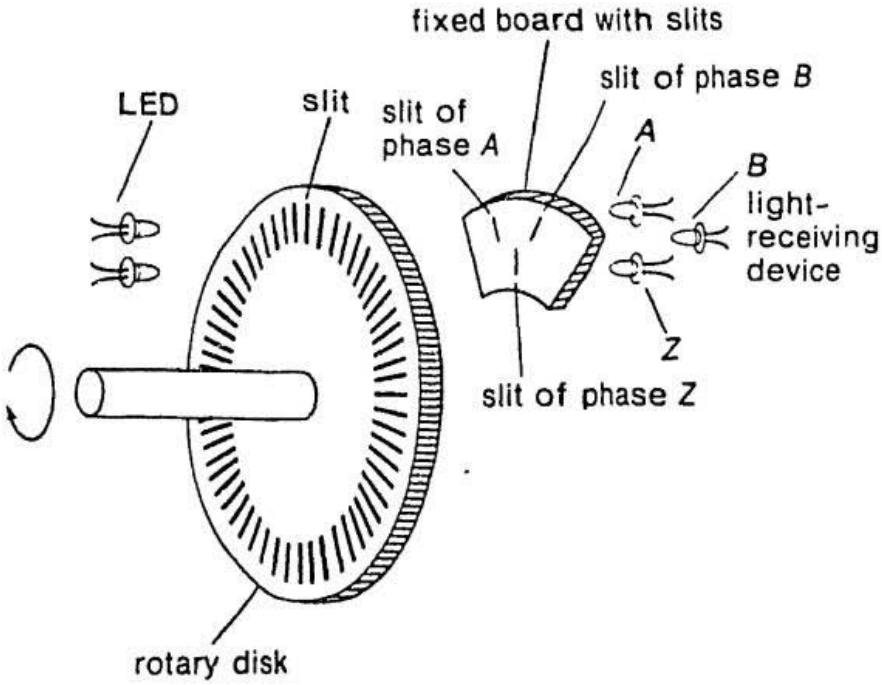

Fig. 6.8 Structure of incremental encoder

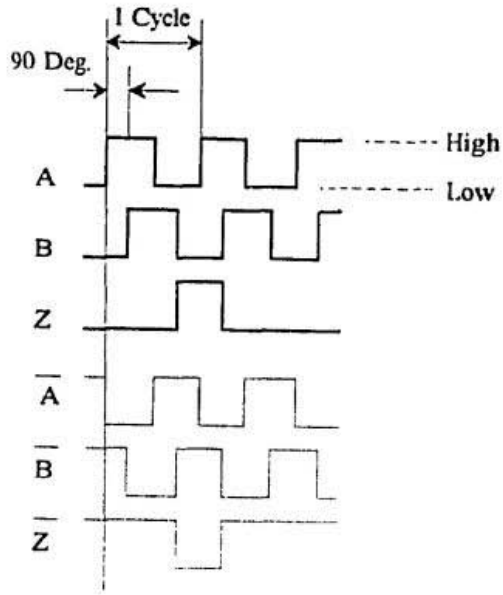

Fig. 6.9 Incremental encoder output waveforms

$$\Delta\theta_r = \frac{2\pi}{pulses\ per\ revolution} \quad (rad) \tag{6.1}$$

In the PMHS vector control system implemented, the incremental optical encoder has

$$pulses\ per\ revolution = 1000 \tag{6.2}$$

Therefore, the resolution of the position measurement is

$$\Delta\theta_r = \frac{2\pi}{1000} \quad (rad) = 0.36\ degree \tag{6.3}$$

6.5.2 Speed Calculation Software

After measuring the rotor position, the rotor speed can then be calculated by

$$\omega_r(nT_r) = \frac{\theta_r(nT_r) - \theta_r((n-1)T_r)}{T_r} \quad (rad./sec.) \tag{6.4}$$

where T_r is the speed calculation time step, and n = 0, 1, 2, ...

The software flow chart for speed calculation is given in Fig. 6.10. First, the value of the pulse counter and pulse index are read. If the index is not equal to one, the rotor position is calculated by multiplying the pulse counter and the pulse resolution. If the index is equal to one, the rotor speed is calculated using the time between two indices.

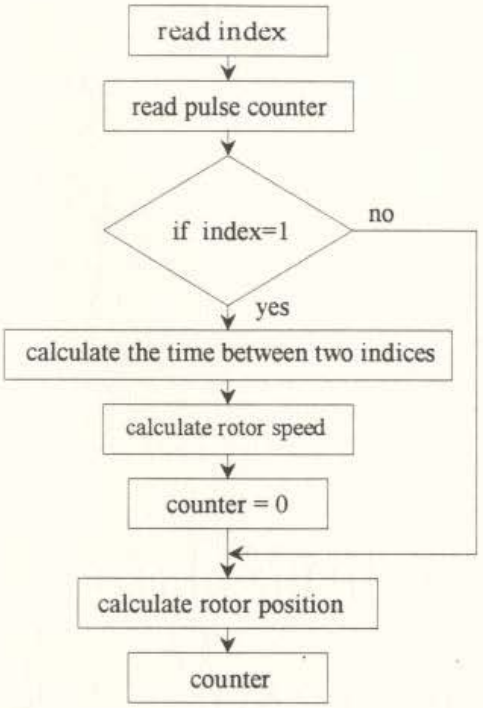

Fig. 6.10 Speed measurement flow chart

6.5.3 Stator Currents Measurement

Hall effect sensors are used for currents measurement in the laboratory experiments. The analog outputs of the current sensors are digitized using 12-bit analog to digital (A/D) converters built in the DS1102 DSP board. Because the A/D ports have single ended bipolar inputs with ± 10 V input span, the maximum output of the current sensors must be limited within 10 V. This is done by adjusting the Hall effect sensor's load. Since the starting current of the PMHS motor is about 40 A, the Hall effect sensor's load is chosen to be 120 Ω. Thus a 1 A input current of the Hall effect sensor is calibrated by 0.12 V Hall effect sensor's output, and the maximum output of the

sensor will be limited within 10 V.

The analog to digital conversion is performed by setting the IOCTL register. The state of the end of conversion outputs of the ADCs can be monitored by reading the IOCTL register bits BUSY. This enables the DSP to track the current conversion and to read the ADC data after the conversion has been completed. For the 12-bit ADC port, the conversion time for each converter is 3 μs.

6.6 Experimental Results of Steady State and Starting Performances

The motor is tested with the dc loading machine coupled to the shaft, where the correspondent angular speeds at frequency range of 1 Hz to 60 Hz are 3.14 rad./sec. to 188.5 rad./sec. and the rotor speeds are 30 rpm to 1800 rpm.

The stator currents are measured by Hall effect sensors and then put into analog to digital ports of the DSP board. The stator d-q axis currents are calculated by transforming the 3-phase a-b-c stator frame currents to 2-phase α-β stator frame, then 2-phase α-β stator frame currents are converted into rotor frame d-q axis. The rotor position is obtained by an optical incremental encoder which is coupled with the PMHS motor shaft, then it is sent to the DSP board through an incremental sensor interface. The rotor angular speeds are calculated from the rotor position as described in section 6.5.2.

Fig. 6.11 shows the steady state performance of DSP based vector control PMHS motor running at 36 Hz. The stator line current i_a is shown in Fig 6.11 (a). It is clear

that there are some spikes in the stator line current. The spikes must be filtered out before the line current is transformed into d-q axis current. The d and q axes currents i_d and i_q are shown in Fig. 6.11 (b) and (c), respectively. From theoretical analysis in Chapter 4, it is known that in the steady state the rotor frame current i_d and i_q are dc quantities. Fig. 6.11 (b) also shows that the current i_d is ideally controlled to zero. Fig. 6.11 (d) shows the rotor position vs time. To avoid the pulse counter over flow, the counter is cleared to zero in every revolution. Thus the rotor position changes from 0 to 2π radian. The rotor angular speed is shown in Fig. 6.11 (e). For 36 Hz operation, the correspondent angular speed is 113.04 rad./sec., and the rotor speed is 1080 rpm.

The starting performance of the DSP based vector control PMHS motor running at 36 Hz is shown in Fig. 6.12. The motor line current i_a is shown in Fig. 6.12 (a). In the traditional ac synchronous motor starting process, the frequency of the stator starting current is fixed because it depends on the frequency of the power supply. This means that during the starting process, the speed of the rotating magnetic field is different from the rotor speed. For the vector control drive, the frequency of the stator current depends on the rotor speed. With the motor speed increasing, the stator current frequency increases. Thus, the speed of the magnetic field is in synchronism with the speed of the rotor. Figs. 6.12 (b) and (c) clearly show the performances of the d-q axis current i_d and i_q during the starting process. The rotor position and rotor angular speed responses as a function of time are shown in Fig. 6.12 (d) and (e), respectively.

Fig. 6.13 shows the steady state performance of the DSP based vector control PMHS motor at 1 Hz operation, with a corresponding angular speed of 3.14 rad./sec.,

which represents a rotor speed of 30 rpm. The stator line current i_a, d-q axis currents i_d and i_q, rotor position and rotor angular speed are shown in Fig. 6.13 (a), (b), (c), (d), and (e), respectively. Figs. 6.13 (d) and (e) show that the motor speed is quite smooth without any oscillation. For the starting performance of the motor at 1 Hz, the control system takes relatively longer time to reach steady state, and the time constant is too long to show any meaningful transient speed response at 1 Hz operation.

The other experimental results showing both steady state and run-up performances for the PMHS motor drive at 12 Hz and 60 Hz are given in Figs. 6.14, 6.15, 6.16 and 6.17, respectively.

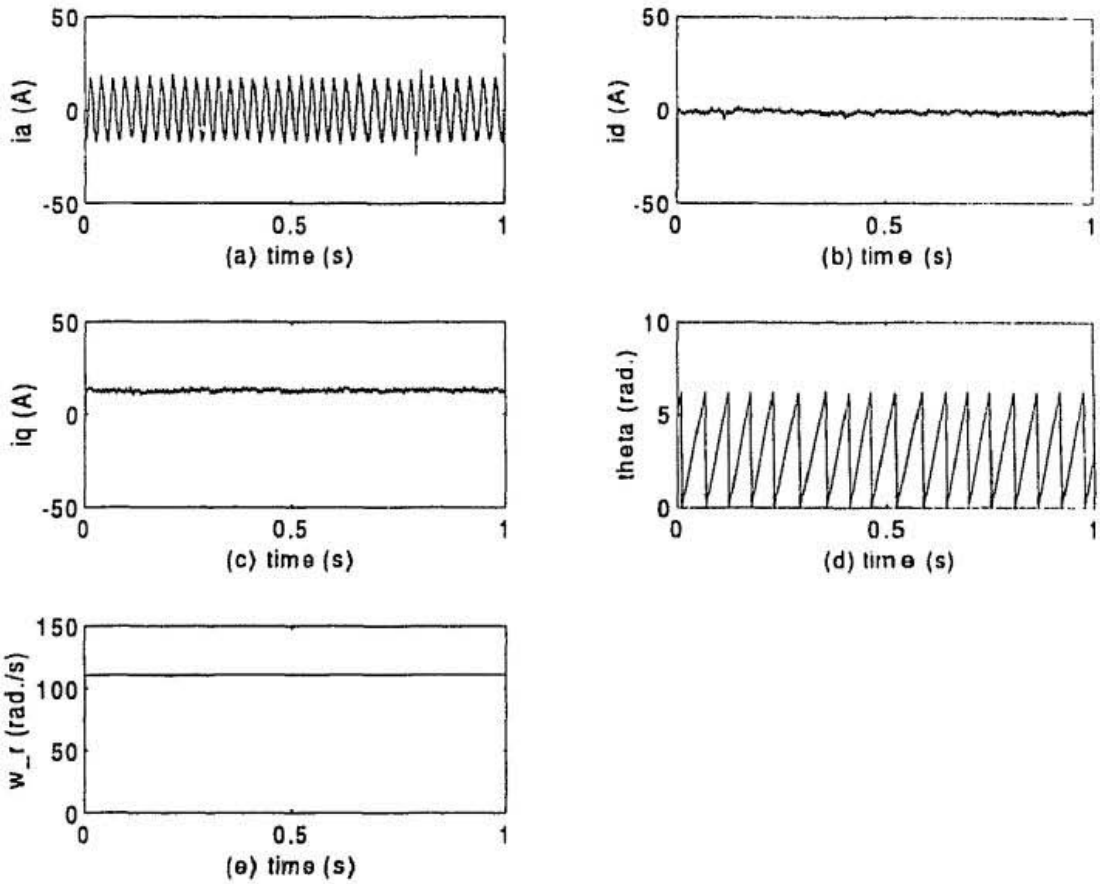

Fig. 6.11 36 Hz steady state performance of the PMHS motor

(a) phase a current; (b) d-axis current

(c) q-axis current; (d) rotor position

(e) rotor speed

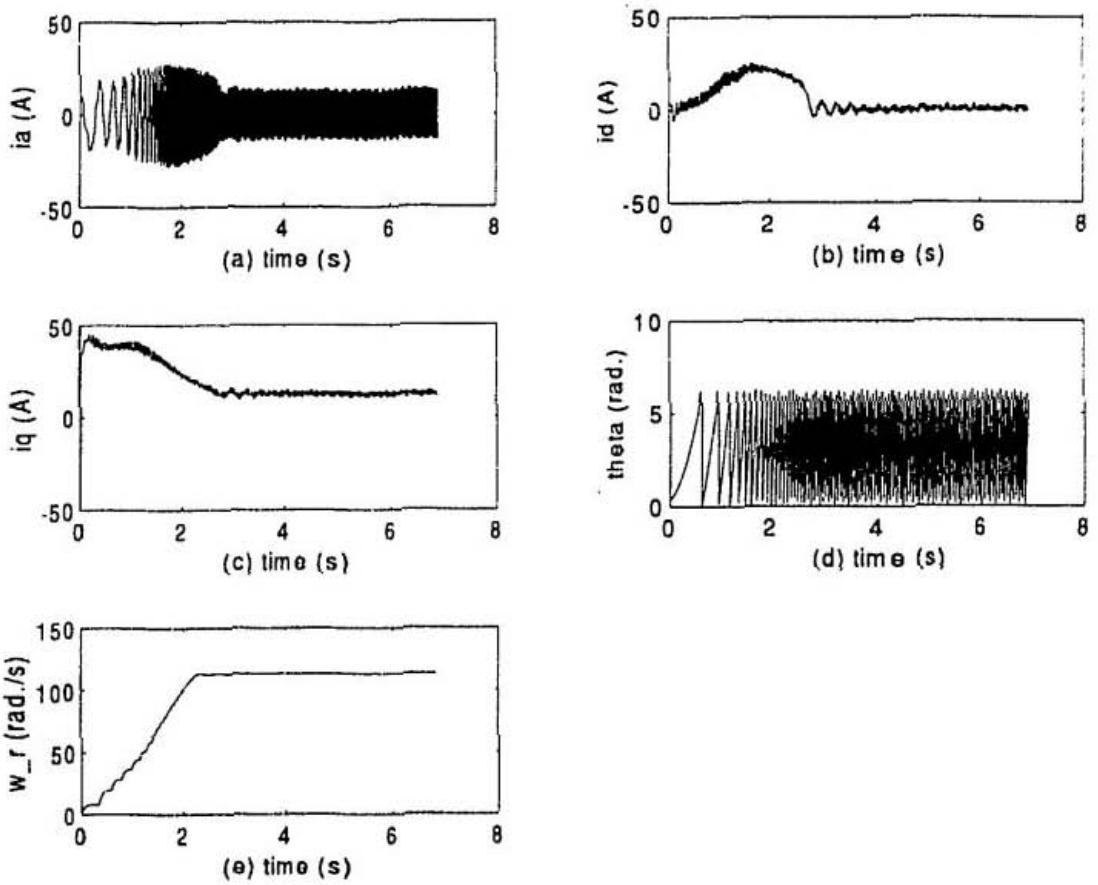

Fig. 6.12 36 Hz starting performance of the PMHS motor

(a) phase a current; (b) d-axis current

(c) q-axis current; (d) rotor position

(e) rotor speed

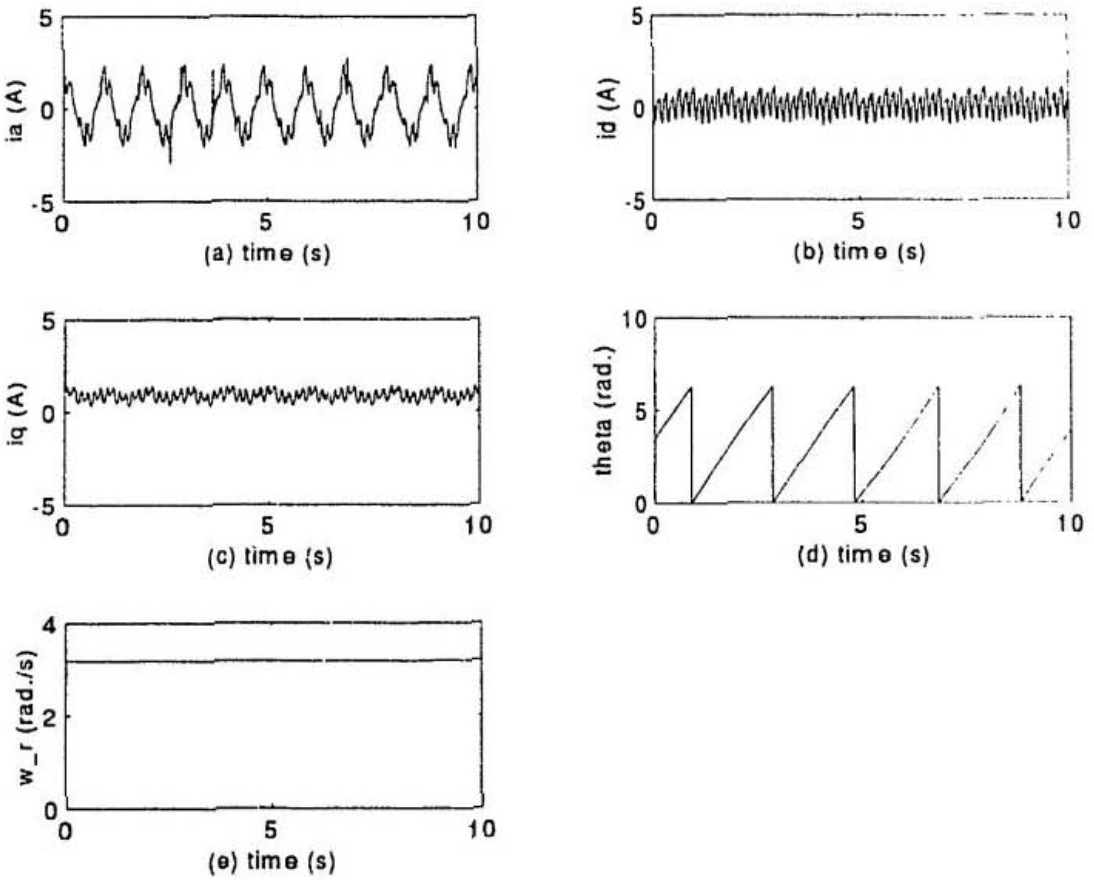

Fig. 6.13 1 Hz steady state performance of the PMHS motor

(a) phase a current; (b) d-axis current

(c) q-axis current; (d) rotor position

(e) rotor speed

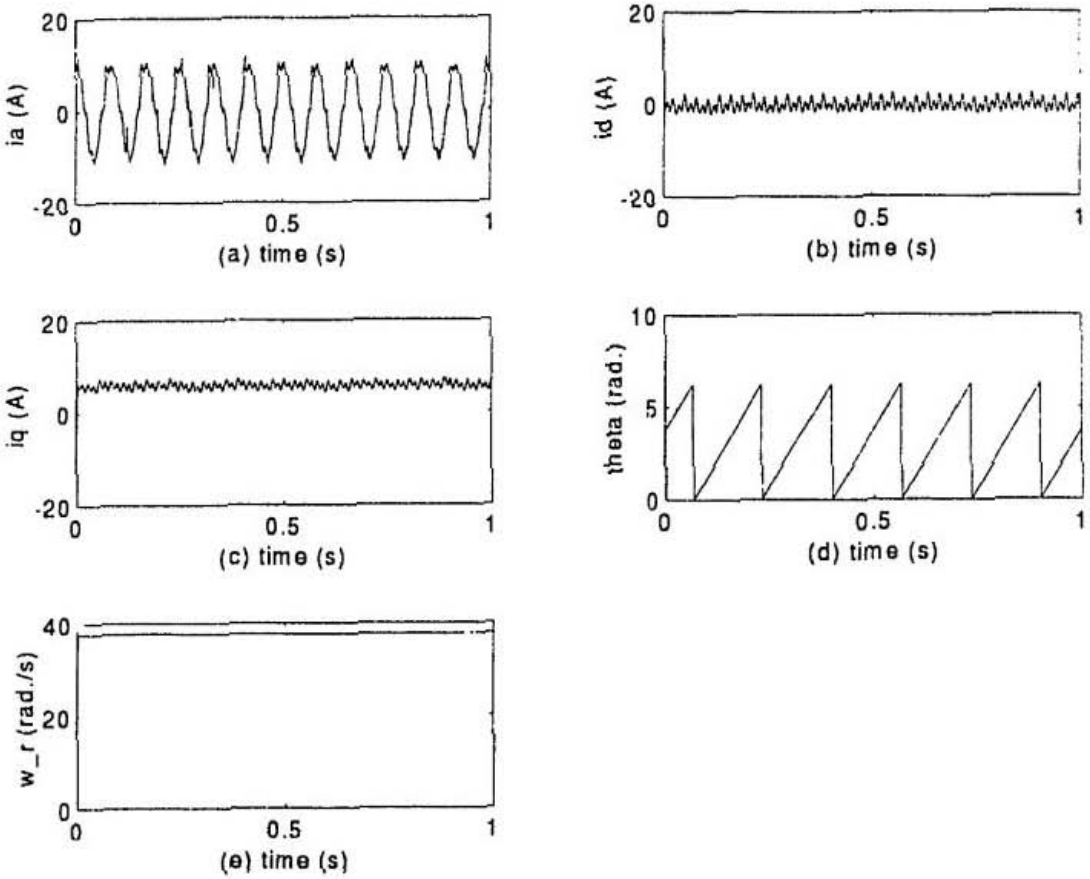

Fig. 6.14 12 Hz steady state performance of the PMHS motor

(a) phase a current; (b) d-axis current

(c) q-axis current; (d) rotor position

(e) rotor speed

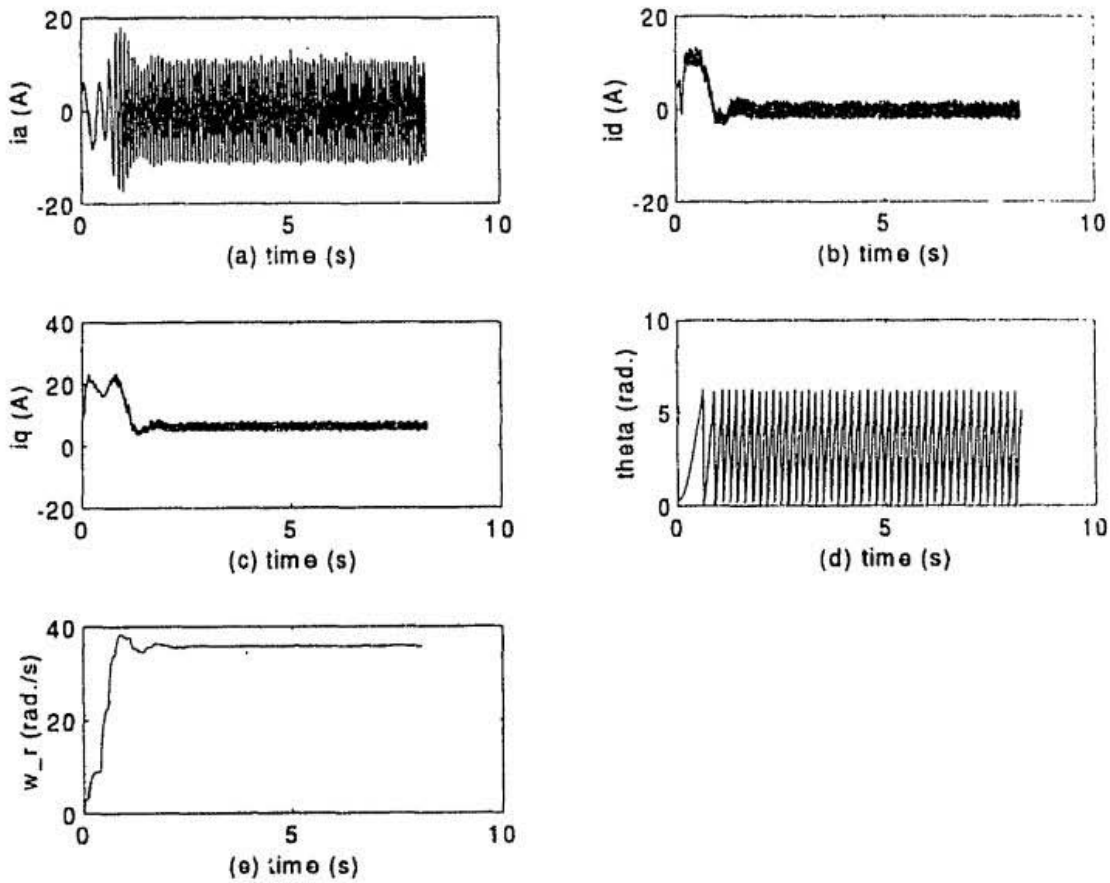

Fig. 6.15 12 Hz Starting performance of the PMHS motor

(a) phase a current; (b) d-axis current

(c) q-axis current; (d) rotor position

(e) rotor speed

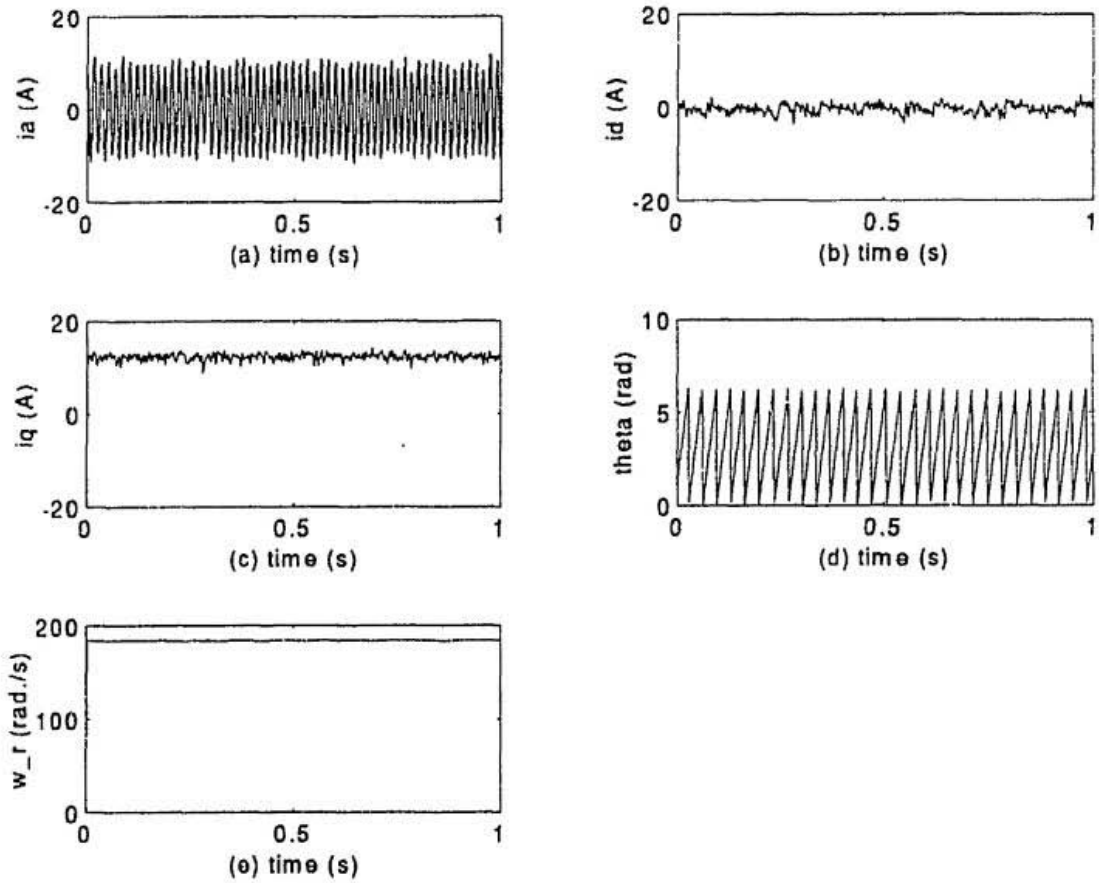

Fig. 6.16 60 Hz steady state performance of the PMHS motor

(a) phase a current; (b) d-axis current

(c) q-axis current; (d) rotor position

(e) rotor speed

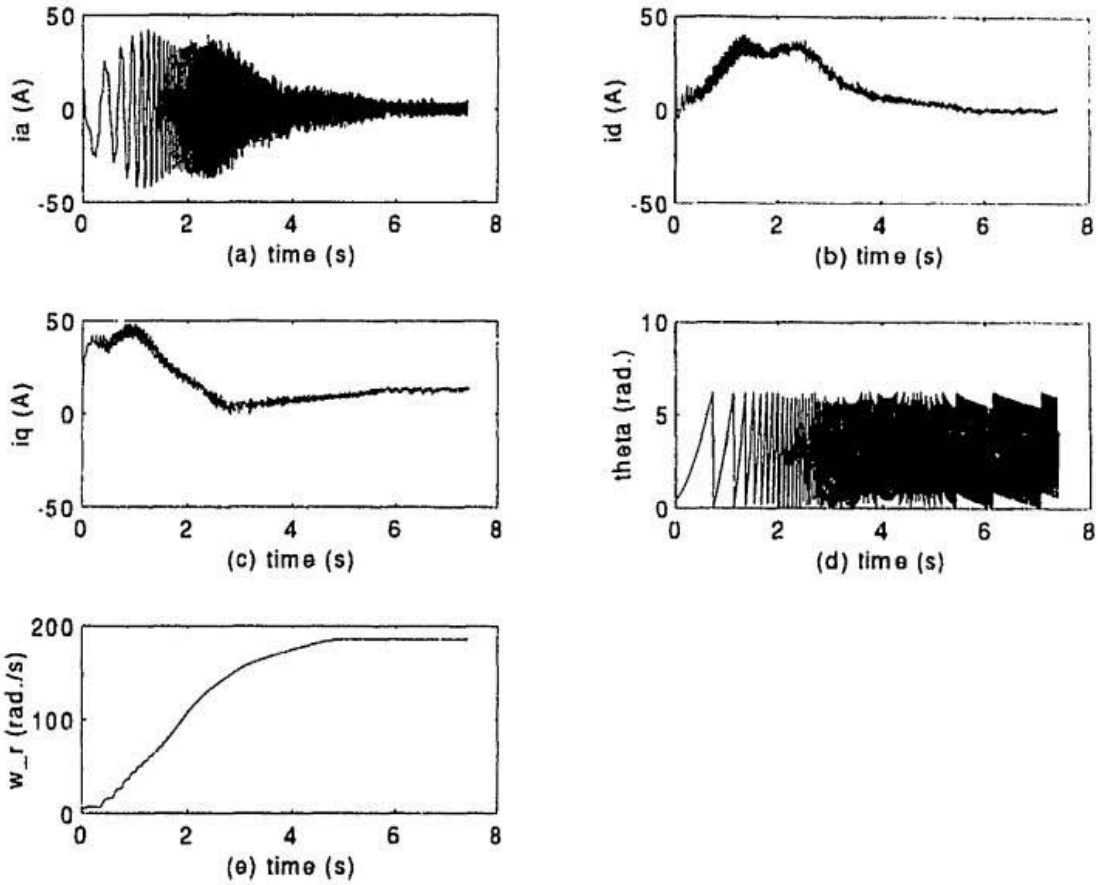

Fig. 6.17 60 Hz starting performance of the PMHS motor

(a) phase a current; (b) d-axis current

(c) q-axis current; (d) rotor position

(e) rotor speed

6.7 Summary

In this chapter, the complete experimental drive system has been described by dividing it into hardware description and software description. The main hardware of the control system, DSP1102 DSP board, PMHS motor and voltage source inverter were presented. Specifically, a brief description of the DSP board was given by discussing the architecture and different subsystems of the DSP board. The measurements of the rotor position and stator currents were discussed by describing the optical incremental encoder and Hall effect current sensors. The flow chart of the rotor speed calculation was also presented. Finally, the experimental results of DSP based PMHS motor vector control system were given. The motor has been successfully controlled from 1 Hz to 60 Hz.

Unlike the operation of conventional synchronous motors at low speed, the PMHS motor drive did not exhibit noticeable instability or oscillation at 1 Hz operation. This is mainly because of the following reasons. First, the rotor hysteresis ring is a built-in damper of the PMHS motor. Second, because of the permanent magnets inserted inside the hysteresis ring, the rotor position compared with the rotating magnetic field is fixed. Third, the design of the PMHS motor drive system which includes the control scheme and parameters chosen, seems appropriate for the selected speed range from 1 Hz to 60 Hz.

Chapter 7

Summary, Conclusion and Suggestions for Future Research

7.1 Thesis Summary and Conclusion

The combination of permanent magnet and hysteresis materials in the rotor of the hybrid permanent magnet hysteresis synchronous (PMHS) motor has many distinct advantages over the conventional permanent magnet (PM) or hysteresis motors. The PMHS motor torque consists of the hysteresis torque, eddy current torque and permanent magnet torque. The negative effect of the magnet brake torque of a conventional PM motor is ideally compensated by the high eddy current and hysteresis torques, particularly at the initial run-up period. It also has features such as simple structure, high speed stability and low noise. This hybrid PMHS motor has good potential for applications in electric vehicles, robotics, gyro scopes and high performance industrial drives requiring smooth starting and quiet operation.

Because this is a new hybrid synchronous motor, there remain many problems to

be solved, such as to establish accurate analytical and control models of the PMHS motor, to eliminate search coils from the motor stator, to improve the stability of the motor at low speed range and to use a high speed digital signal processor for the PMHS motor vector control.

Chapter 2 developed a PMHS motor model for applications of DSP based vector control and simulation. The discussion started with the introduction of the PMHS motor structure. Based on the features of this structure and the models of permanent magnet and hysteresis, the magnetic equivalent circuit of the PMHS motor was developed. The voltage and flux equations involved in developing the electrical equivalent circuits were also developed in that chapter. The electrical equivalent circuits were presented in the rotor frame d-q axis. An analytical model including the derivation of state variable equations in time domain was developed. The transient current, torque, speed and flux linkages during the starting and synchronizing process have been calculated by solving the state variable equations numerically. Reasonably good agreements between the computed and experimental results of a 5 hp PMHS laboratory motor confirm the validity of the proposed analysis.

Chapter 3 was devoted to the programmed sinusoidal pulse width modulation which was used for PMHS motor vector control. After briefly reviewing the theory of pulse width modulation, the interpretation of the operation of the inverter was gained through a voltage space vector analysis. Next, a detailed analysis of the logic relations of a switching sequence in two PWM periods was discussed. Using TMS320P14 DSP microcontroller, six channel PWM signals were generated. The gate signals of the

inverter with shoot through delay were achieved through hardware logic operation. Finally, programmed three-phase sinusoidal PWM voltage experimental results were given in different modulation cases.

Chapter 4 developed the all digital current controller for the PMHS motor drive system. Because the conventional PI stator frame line current controllers introduce unwanted speed dependent coupling into the system, there are magnitude and phase errors when sinusoidal commands are applied to a PI controller. The approach of implementing the PI current controllers directly in the rotor frame was taken here. This results in zero steady state error. Because the independent control of the field flux and torque is required for PMHS motor vector control application, the decoupling controller transformed the torque and field flux commands into equivalent current commands to influence these variables independently. This is similar to the dc motor drive where field flux is controlled by the field current and torque by the armature current. Using the frequency domain approach, the direct and quadrature axis current controllers were developed. Based on the current and speed loop transfer functions, the Bode plot designs were given. The control algorithms were then put into a form that could be implemented directly on the real-time digital system. After that, the advantages and disadvantages of both FIR and IIR digital filters were discussed, and the first order IIR filter was chosen. Finally, an experimental verification of the algorithm was carried out by measuring the stator line currents at different frequencies.

Chapter 5 concentrated on the development of the digital speed controller for the PMHS vector control system. First, the general expression of the developed torque of

the PMHS motor was obtained. Because the developed torque depends on the amplitudes of the stator currents, rotor currents, and also because of the nonlinear hysteresis and eddy current properties, the prediction of the developed torque of the PMHS motor is quite complicated. Because the control of stator current i_{ds} to zero was applied, i_{qs} was the only controllable variable. Thus the torque equation was similar to the classical torque expression of a separately excited dc motor.

For the convenience of controller design, the transfer function was simplified so that the current control loop was approximated by an inertia element with equivalent time constant T_{eq}. The speed controller design was based on the symmetry optimization. Then, the Bode plot of both the open and closed loop speed control system, and the unit step responses of the closed speed control system were given.

The performance of the speed controller was then demonstrated with several real-time experiments. The speed controller was shown to possess the desired characteristics in terms of rise time and overshoot. The steady state rotor position and speed responses were quite smooth in a wide speed range and without any noticeable oscillation.

Chapter 6 described the complete experimental drive system by dividing it into hardware and software descriptions. In implementing this control system, the system's major functions and their interconnections were described by means of functional diagram. Then, a brief description of the system software was presented. The main hardware of the control system, DSP1102 DSP board, PMHS motor and voltage source inverter were presented. Specifically, a detailed description of the DSP board was given by discussing the architecture and different subsystems of the DS1102 DSP board. The

measurements of the rotor position and stator currents were discussed by describing the optical incremental encoder and Hall effect current sensors. The flow chart of the rotor speed calculation was also presented. Finally, the experimental results of DSP based PMHS motor vector control system were given. The motor was controlled from 1 Hz to 60 Hz successfully.

The conclusions of this thesis are:

The transient and steady state performances of current and speed show that the vector control of the PMHS motor has important features for smooth and quiet operation over a wide speed range. The experimental results verified the effectiveness of the motor models for a high performance PMHS motor drive.

7.2 Contributions

The major contributions made in this thesis can be summarized in the following two parts: to present PMHS motor models for analysis and control, and to build a DSP based vector control system for the PMHS motor drive.

1) PMHS motor models for analysis and control

- Based on the analysis of the permanent magnet and hysteresis models, the magnetic equivalent circuit of the PMHS motor was developed.
- The PMHS motor electrical equivalent circuit was presented. The rotor hysteresis and eddy currents, which are difficult to access by means of outside control, can be calculated by this equivalent circuit.
- The general expression of the developed torque of the PMHS motor was

derived. The torque equation was analyzed for the control purpose.

- A time domain state variable model of the PMHS motor for the steady state and run-up period was presented. Using the state variable method, analytical expressions have been derived. Theoretical prediction for the PMHS motor performance was done by solving the state variable equations numerically.

2) DSP based vector control system for the PMHS motor drive

- A programmed sinusoidal pulse width modulation has been developed and successfully operated for PMHS motor vector control sysetem.

- A DSP based vector control system for the PMHS motor drive has been built and the motor has been controlled from 1 Hz to 60 Hz successfully. Experimental results show that the PMHS motor exhibits improved speed stability especially in the very low speed range. This thesis is the first to develop such a control system for the PMHS motor.

7.3 Suggestions for Future Research

Based on the experience gained from the study that was carried out for this thesis, a few recommendations for further research are listed below:

- The motor used in this thesis is a laboratory prototype hybrid permanent magnet hysteresis synchronous motor. The design optimization of the PMHS motor with better efficiency and torque capabilities is required for drive applications. It should be emphasized that the motor design is a part of the system trade off. For example, selection of single speed or multiple speed operation would impose different constraints on motor

design. Therefore, the new motor design has to be dealt with at the system level.

- In this application, the controllers designed around nominal operating parameters are used to meet performance specifications. However, load changes, temperature variations and changing geometry can often disturb operating conditions enough to compromise motor performance in terms of accuracy, speed, and efficiency. Adaptive control is recommended for future research because it can redesign controllers based on some type of performance index, and can potentially overcome these problems.

- The encoder used in this control system presents several disadvantages from the standpoint of drive cost, size and noise immunity. For these reasons, a challenge remains so as to eliminate this sensor from the motor and to realize a sensorless control of the PMHS motor. The rotor position and speed will be estimated from on line voltage, current and motor parameters.

References

[1] C.P.Steinmetz, *Theory and Calculation of AC Current Phenomena*, McGraw-Hill, N.Y., 1908, p.122 and 180.

[2] B.R.Teare, "Theory of hysteresis motor", AIEE Transactions, vol.59, 1940, pp.907-912.

[3] G.R.Slemon, R.D.Jackson and M.A.Rahman, "Performance for large hysteresis motors", IEEE Transactions on Power Apparatus & Systems, vol.PAS-96, Dec. 1977, pp.1915-1919.

[4] M.A.Rahman, M.A.Copeland and G.R.Slemon, "An analysis of the hysteresis motor, III parasitic losses," IEEE Trans. on Power Apparatus and Systems, vol. PAS-88, no.6, June 1969, pp.954-961.

[5] S.P.Clurman, "On hunting in hysteresis motors and techniques," IEEE Transactions on Magnetics, September 1971, pp.512-517.

[6] M.A.Rahman and A.M.Osheiba, "Dynamic Performance Prediction of Polyphase Hysteresis Motors", IEEE Transactions on Industry Applications, vol.26, no.6, Nov.-Dec. 1990, pp.1026-1033.

[7] R.Qin and R.Zhong, "The Starting Process Analysis of Hysteresis Motors", Small

and Special Electrical Machines, China, no.4, 1986, pp.25-31.

[8] M.A.Rahman, "Permanent magnet synchronous motor - A review of the design art", Proceeding of International Conference on Electrical Machines, Athens, Greece, Part 1, Sept. 15-17, 1980, pp.312-319.

[9] E.Richter, "Permanent Magnet Motors Technical Report", General Electric Company (Corporate Research and Development,) Schenectaddy, NY, Sept. 1984.

[10] T.J.E.Miller, "Synchronization of line-start permanent-magnet AC motors," IEEE Transactions on Magnetics, vol. no.3, May 1984, pp.507-515.

[11] M.A.Rahman, A.M.Osheiba, T.A.Little, G.R.Slemon, "Samarium cobalt permanent magnet on the performance of polyphase hysteresis-reluctance motors," IEEE Transctions on Magnetics, vol. MAG-20, no.5,pt.2, Sept., 1984,pp.1765-7.

[12] H.Yamada, "Characteristics of a hysteresis motor using permanent magnet particles," Trans. Soc. Instrum. and Eng. (Japan), vol.21, no.1, Jan. 1985, pp.102-3.

[13] H.Lechner, "Numerical calculation of the magnetic permanent magnet hysteresis drive," Tech. Mod. (France), vol.78,no.3-4, March-April 1986,pp.23-7.

[14] T.A.Little, M.A.Rahman and G.R.Slemon, "Analytical Model for Permanent Magnet Synchronous Motors", IEEE Tran. on Magn., vol. MAG-21, no.5, Sept. 1985, pp.1741-43.

[15] M.A.Rahman, "Combination Hysteresis Reluctance Magnet Motor", U.S. Patent Number 5,187,401, Feb.16, 1993.

[16] M.A.Rahman and Ruifeng Qin, "A permanent magnet hysteresis hybrid motor drive for electric vehicles", IECON96', August 5-6, 1996, Taipei, Taiwan.

[17] J.Qian and M.A.Rahman, "Analysis of Field Oriented for Permanent Magnet Hysteresis Synchronous Motors", IEEE Tran. on Industry Applications, vol.29, no.6, Nov./Dec. 1993, pp.1156-1163.

[18] P.C.Sen, *Principles of Electric Machines and Electronics*, New York: Wiley, 1988.

[19] P.C.Sen, *Thyristor DC Drives*, New York: Interscience, 1981.

[20] P.C.Sen, "Electric Motor Drives and Control -- Present, and Future," IEEE Tran. on Industrial Electronics, vol.37, no.6, Dec. 1990, pp.562-575.

[21] K.P.Phillips, "Current-source converter for ac motor drives," IEEE Trans. on Industry Applications, vol. IA-18, no.6, Nov./Dec. 1972, pp.679-683.

[22] M.L.MacDonald and P.C.Sen, "Control loop study of induction motor drives using DQ model," IEEE Trans. Ind. Contr. Instrum., vol. IECI-26, no.4, 1979, pp.237-243.

[23] F.Blaschke, "The principle of field orientation as to the new trans vector closed-loop control system for machines," Siemens Rev., 1972.

[24] K.Hasse, "Zum Dynamischen Verhalten der bei Betriek Mit Variabler Standerfrequenz und Standerspannung", ETZ-A, Bd.9, 1968, p.77.

[25] T.M.Jahns, "Flux-weakening regime operation of an permanent-magnet sychronous motor drive," IEEE Trans. Industry Appl., vol.IA-23, July/Aug. 1987, pp.681-689.

[26] R.Shiferl and T.A.Lipo, "Power capability of pole permanent magnet synchronous motors in variable speed drive applications," IEEE IAS Annual Conference Record, Oct. 1988, pp.23-31.

[27] L.A.Jones and J.H.Lang, "A state observer for the permanent-magnet synchronous motor," IEEE Trans. on Industry Electronics, vol.3, Aug.1989, pp.374-382.

[28] R.Wu and G.R.Slemon, "A permanent-magnet motor drive without a shaft sensor," Conference Record of IEEE/IAS Annual Meeting, October 7-12, 1990, pp. 553-558.

[29] M.Naidu and B.K.Bose, "Rotor position estimation scheme of a permanent magnet synchronous machine for high performance variable speed drive," IEEE/IAS Annual Meeting, 1992, pp48-53.

[30] R.B.Sepe and J.H.Lang, "Real-time adaptive control of the permanent-magnet synchronous motor," IEEE Trans. on Industry Applications, vol.27, July/Aug. 1991, pp.706-714.

[31] R.B.Sepe and J.H.Lang, "Real-time observer-based (adaptive) control of a permanent-magnet synchronous motor without mechanical sensors," IEEE Trans. on Industry Applications, no.6, Nov./Dec. 1992, pp.1345-52.

[32] T.S.Low, T.H.Lee and K.T.Chang, "A nonlinear speed observer for permanent-magnet synchronous motors," IEEE Trans. Industrial Electronics, vol.40, no.3, June 1993, pp307-316.

[33] N.Ertugrul and P.Acarnley, "A new algorithm for sensorless operation of permanent magnet motors," IEEE Trans. on Industry Applications, vol.30, no.1, January/February 1994, pp.126-133.

[34] M.A.Rahman and P.Zhou, "Analysis of brushless permanent magnet synchronous motors", IEEE Transactions on Industrial Electronics, vol.43, no.2, April 1996, pp.256-267.

[35] T.Sebastian, *Steady-state performance of variable speed permanent magnet synchronous motors*, Ph.D. Thesis, University of Toronto, Toronto, Ontario, Canada,

Oct. 1986.

[36] M.A.Copeland and G.R.Slemon, "An analysis of the hysteresis motor I-analysis of the idealized machine", IEEE Transactions on Power Apparatus and Systems, Vol. 82, April 1963, pp.34-42.

[37] Paul C.Krause, *Analysis of electric machinery*, McGraw-Hill book company, 1986.

[38] Ruifeng Qin and M.A.Rahman, "The equivalent circuits for permanent magnet hysteresis synchronous motors", IEEE/NECEC'95, May 4-5, 1995, St. John's, Newfoundland, pp.155-160.

[39] I.Boldea and S.A.Nasar, *Electric Machine Dynamics*. New York: Macmillan Publishing Company, 1986, pp.63-69.

[40] M.A.Rahman and Ruifeng Qin, "Starting and synchronization of permanent magnet hysteresis motors," IEEE IAS Annual Conference Record, Denver, Colorada, USA, October 2-7, 1994. pp.210-215.

[41] M.H.Rashid, *Power Electronics Circuits, Devices and Applications*, second edition, Prentice Hall, 1993, pp.376-378.

[42] A.J.Pollmann, "Software pulsewidth modulation for μP control of AC drives", IEEE Tran. vol. IA-22, no.4, July/August, 1986, pp.691-696.

[43] T.M.Rowan, R.J.Kerkman, "A new synchronous current regulator and an analysis of current regulated PWM inverter", IEEE Trans. on Industry Applications, 22, July/August, 1986, pp.678-690.

[44] "Controller for synchronous AC drive running on DS1101, application note", Preliminary document version 1.0, dSPACE digital signal processing and control

engineering GmbH. August 17, 1992.

[45] B.C.Kuo, *Automatic Control Systems*, Prentice Hall, Englewood Cliffs, New Jersey, 1991.

[46] S.Sastry, M.Bodson, *Adaptive Control: Stability, Convergence, and Robustness*. Prentice Hall, 1989.

[47] J.N.Little and L.Shure, "*Signal Processing Toolbox for Use with MATLAB*", The Math Works, Inc. May 1993.

Appendix A

Design Data of the PMHS Motor

PMHS motor dimensions and design data are given in Table A1:

able A1. Design dimensions and material properties of the PMHS Motor

stator	Rotor
stator inner dia. 151mm	rotor outer diameter 150mm
core length 105mm	length of rotor ring 105 mm
number of slots 48	hysteresis ring thickness 16mm
number of poles 4	air gap length 0.33 mm
number of n/coil 27	PM material thickness 6.25mm
umber of coils 48	width of PM materials 40 mm
stator coil pitch 1-13	
winding factor 0.829	
type of winding: double layer lap.	

Properties	Materials	
	36% Cobalt Steel	NdFeB
residual flux density (kG)	9.60	11.38
coercive force (kO_c)	0.24	10.84
recoil permeability	18.00	1.01
energy product (MGO_e)	1.00	31.10

Table A2. The parameters of the experimental PMHS motor

Parameters	Values
Stator leakage inductance (H)	0.0086
Rotor leakage inductance (H)	0.0070
Hysteresis incremental inductance (H)	0.0050
Rotor hysteresis resistance (Ω)	9.8000
Rotor eddy current resistance (Ω)	18.700
Permeance Λ_d (H)	$0.3403*10^{-6}$
Permeance Λ_q (H)	$0.3930*10^{-6}$
Permeance Λ_m (H)	$0.3134*10^{-6}$
Magnetomotive force F_m (A)	$0.9415*10^{+5}$

Appendix B

The Flow Chart of the State Variable Equation

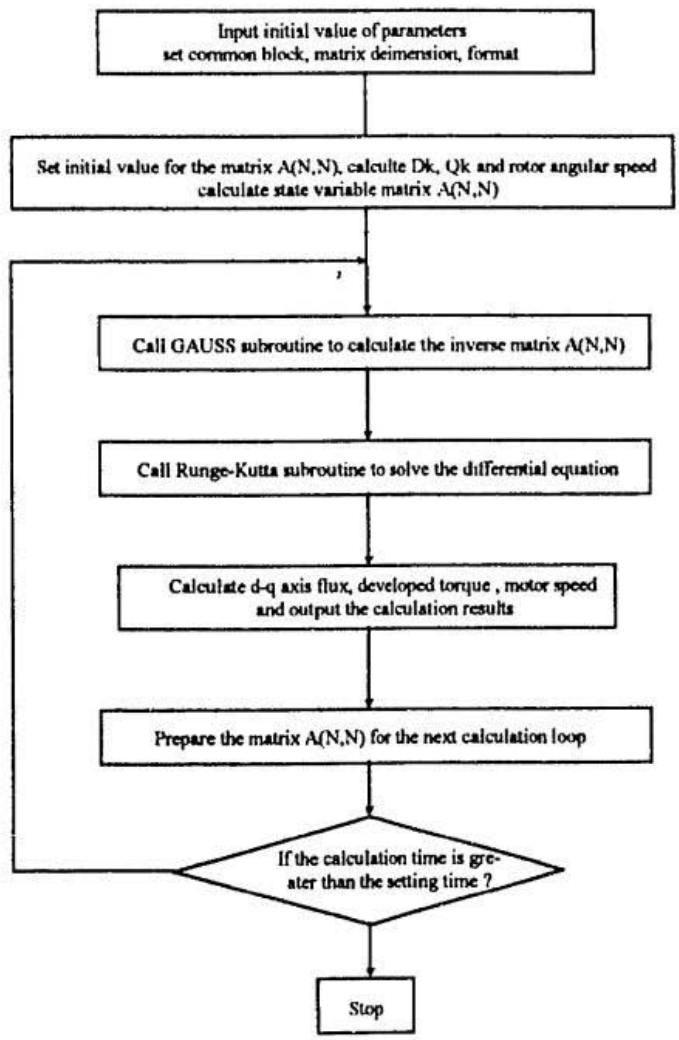

Fig. B.1 The flow chart of the state variable equation

Appendix C

The Derivation of the Unit Matrix

Following is the derivation of the unitary matrix which was mentioned in the section 4.3 for the stator frame voltage and integral equations.

From

$$C_{sd} = \begin{bmatrix} \cos\theta & \sin\theta \\ -\sin\theta & \cos\theta \end{bmatrix} \tag{C.1}$$

we obtain

$$\frac{d}{dt} C_{sd} = -\frac{d\theta}{dt} \begin{bmatrix} \sin\theta & -\cos\theta \\ \cos\theta & \sin\theta \end{bmatrix} \tag{C.2}$$

We know that

$$\begin{bmatrix} A & B \\ C & D \end{bmatrix}^{-1} \begin{bmatrix} A & B \\ C & D \end{bmatrix} \begin{bmatrix} \sin\theta & -\cos\theta \\ \cos\theta & \sin\theta \end{bmatrix} = \begin{bmatrix} \sin\theta & -\cos\theta \\ \cos\theta & \sin\theta \end{bmatrix} \tag{C.3}$$

Now we try to find A, B, C and D to satisfy

$$\begin{bmatrix} A & B \\ C & D \end{bmatrix} \begin{bmatrix} \sin\theta & -\cos\theta \\ \cos\theta & \sin\theta \end{bmatrix} = \begin{bmatrix} \cos\theta & \sin\theta \\ -\sin\theta & \cos\theta \end{bmatrix} \tag{C.4}$$

from (C.4)

$$\begin{aligned} A\sin\theta + B\cos\theta &= \cos\theta \\ -A\cos\theta + B\sin\theta &= \sin\theta \end{aligned} \tag{C.5}$$

thus

$$A = \frac{(1-B)\cos\theta}{\sin\theta}$$

$$-\frac{(1-B)\cos\theta}{\sin\theta}\cos\theta + B\sin\theta = \sin\theta$$

$$(B-1)\cos^2\theta + B\sin^2\theta = \sin^2\theta \qquad (C.6)$$

$$(B-1)\cos^2\theta + (B-1)\sin^2\theta = 0$$

$$(B-1)(\cos^2\theta + \sin^2\theta) = 0$$

$$B=1$$

$$A=0$$

from (C.4)

$$C\sin\theta + D\cos\theta = -\sin\theta$$
$$-C\cos\theta + D\sin\theta = \cos\theta \qquad (C.7)$$

$$D = \frac{-(1+C)\sin\theta}{\cos\theta}$$

$$-C\cos\theta - \frac{(1+C)\sin\theta}{\cos\theta}\sin d\theta = \cos\theta$$

$$-C\cos^2\theta - (1+C)\sin^2\theta = \cos^2\theta \qquad (C.8)$$

$$(1+C)\cos^2\theta + (1+C)\sin^2\theta = 0$$

$$C = -1$$

$$D = 0$$

thus

$$\begin{bmatrix} A & B \\ C & D \end{bmatrix} = \begin{bmatrix} 0 & 1 \\ -1 & 0 \end{bmatrix} \qquad (C.9)$$

$$\begin{bmatrix} A & B \\ C & D \end{bmatrix}^{-1} = \begin{bmatrix} 0 & -1 \\ 1 & 0 \end{bmatrix}$$

So

$$\frac{d}{dt}C_{nl} = -\frac{d\theta}{dt}\begin{bmatrix} 0 & -1 \\ 1 & 0 \end{bmatrix}C_{nl} = \frac{d\theta}{dt}\begin{bmatrix} 0 & 1 \\ -1 & 0 \end{bmatrix}C_{nl} \qquad (C.10)$$

Appendix D

DS1102 Data Sheet

Table D1 DS1102 Control Board Data Sheet

Processor	Texas Instruments TMS320C31 floating point DSP running at 40 MHz clock rate and 50 ns cycle time. Two 32-bit on-chip timers/event counters. On-chip bidirectional 8 MBaud serial link. On-chip DMA. 4 interrupt lines.
Memory	128K*32-bit zero wait state memory. 2K*32-bit on-chip memory.
16-bit ADCs	±10 V input range. 10 μs conversion time. ±5 mV offset voltage. ±0.25 % gain error. 4 ppm/K offset drift. 25 ppm/K gain drift. >80 dB signal to noise ratio.

12-bit ADCs	±10 V input range. 3 μs conversion time. ±5 mV offset voltage. ±0.5 % gain error. 4 ppm/K offset drift. 25 ppm/K gain drift. >65 dB signal to noise ratio.
DACs	±10 V output range. 4 μs settling time. ±5 mV offset error. ±0.5 % gain error. 5 mA output current. 13 ppm/K offset drift. 25 ppm/K gain drift.

Slave DSP	Texas Instruments TMS320P14 DSP 25 MHz clock rate, 160 ns cycle time. 32-bit arithmetic unit. 4K*16-bit on-chip PROM containing firmware 4K*16-bit external program RAM. 256*16-bit on-chip data RAM. Bit selectable 16-bit I/O port. 6 high precision PWM outputs. event manager with capture inputs and compare outputs.
Incremental encoder interface	Fourfold pulse multiplication. 8.3 MHz maximum count frequency. Three stage digital pulse filter. 24-bit position counter. 5V/200 mA sensor supply voltage.
Host-Interface	Four 16-bit and three 8-bit I/O ports in the 64K host I/O space. Memory and I/O are accessible by the host even while the DSP is running. DSP-host and host-DSP interrupts.
JTAG-Interface	On board test bus controller and emulator connector.

Physical size	160 mm * 107 mm * 20 mm. Requires one half length PC-slot.
Power supply	+ 5 V ± 10%, 1.5 A. ± 12 V ± 5%, 100 mA.

Appendix E

Experimental Results of Back emf of the PMHS Motor

During the starting process, the hysteresis loop sweeps across the PMHS rotor until it reaches synchronous speed, where the hysteresis ring acts as though it was a permanent magnet. Once the rotor reaches synchronous speed, hysteresis poles will be fixed on the rotor surface. The relative position between the hysteresis poles and PM poles is important for the successful operation of the PMHS motor.

By measuring the electromotive force (emf) at different speeds, the sweeping rotor poles during the starting process are observed. The PMHS motor was connected with a rated 3-phase, 60 Hz, 208 V ac power supply. The emf is sensed by a search coil which is inserted inside of the stator slots, then the emf signals are measured by a digital oscilloscope. The emfs are measured at different speed during the starting process. The motor speeds at which the emf are measured are 0.2 pu, 0.4 pu, 0.6 pu, 0.8 pu, 0.9 pu and 1.0 pu, where pu represent the per unit speed which is 1800 rpm for the 4-pole PMHS motor. During the starting process, the emfs of the PMHS motor at different speed are shown in Fig. E.1.

When the rotor is blocked to standstill, and the stator windings are switched on with power supply for a short time, then the hysteresis poles will be formed on the rotor

because of the residual flux density B_r of the hysteresis material. A dc motor which is coupled co-axially with the experimental PMHS motor is used to drive the PMHS motor at a certain speed. The emf waveforms are measured from the stator winding as shown in Fig. E.2.

If the PMHS motor is run at a certain speed, then the power supply is turned off, by the same method as mentioned above, the measured emfs are shown in Fig. E.3 for the speed of 0.9 pu. From Fig. E.2 and Fig. E.3 one can deduce that, during the starting process the rotor pole formed by the hysteresis effect is sweeping around the rotor surface. That is to say when the power is turned off before the motor runs at synchronous speed, the relative positions of the hysteresis poles to PM poles are uncertain.

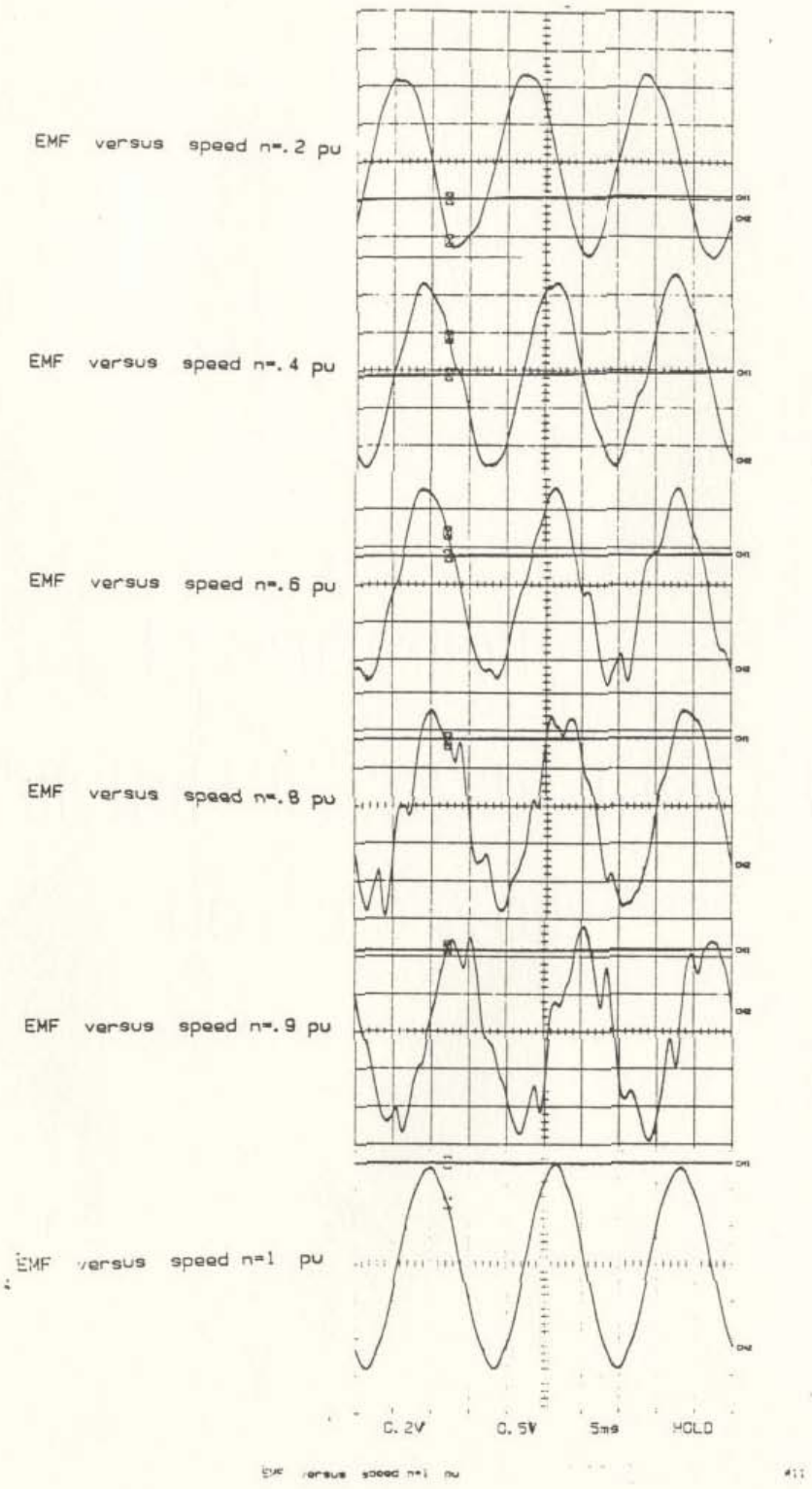

Fig. E.1 emf of the PMHS motor vs speed

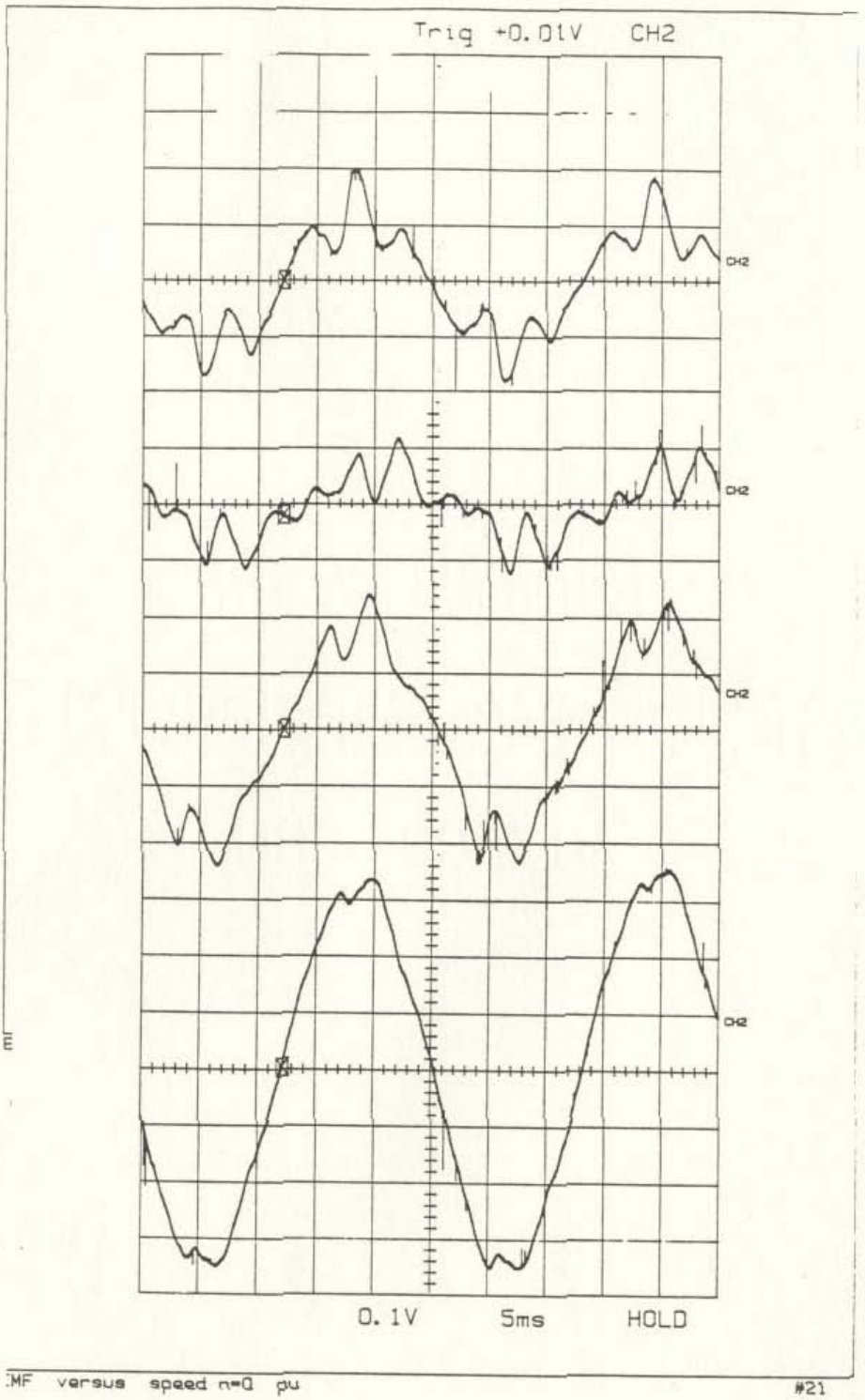

Fig. E.2 emf of PMHS motor when it is blocked

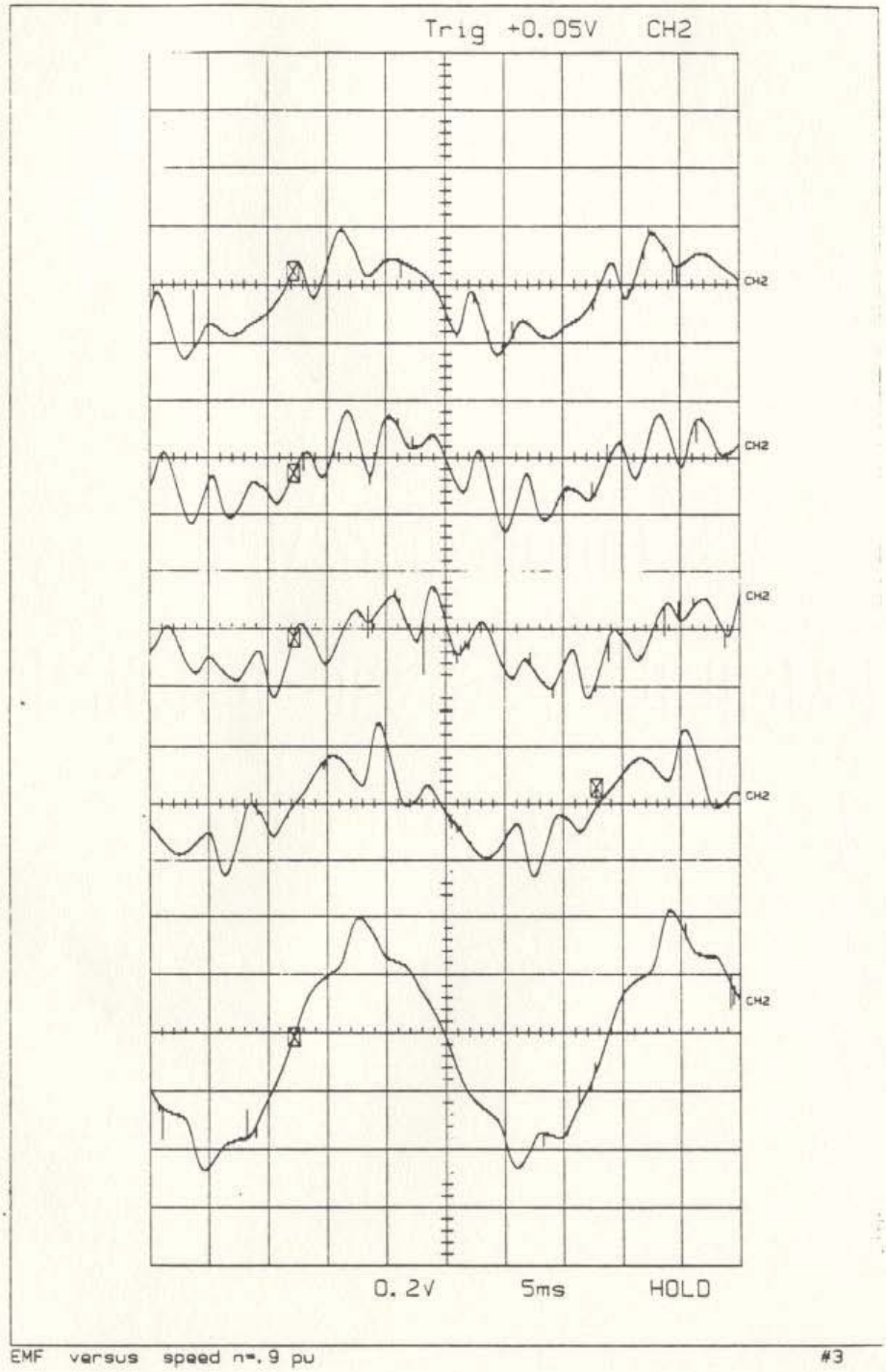

Fig. E.3 emf of PMHS motor when it runs at 0.9 pu speed